

THÈSE DE DOCTORAT

Soutenue à Aix-Marseille Université

Le 04 NOVEMBRE 2022 par :

IMENE GUELLIL

Nano-fonctionnalisation par FIB haute résolution de silicium

Discipline

Physique et sciences de la matière

Spécialité

Matière Condensée et Nanosciences

École doctorale

ED 352 – PHYSIQUE ET SCIENCES DE
LA MATIERE

Laboratoire

IM2NP-Marseille

• **Composition du jury :**

-
-
-
-
- **AISSAT Abdelkader** Rapporteur
- *Professeur, Université de BLIDA*
- **MOTTA Nunzio** Rapporteur
- *Professeur, École de chimie et de physique*
- **OSMOND Johann** Examineur
- *Ingénieur de recherche, Institut des Sciences Photoniques de l'ICFO*
- **ABEL Mathieu** Président du jury
- *Professeur, Aix Marseille Université*
- **BERBEZIER Isabelle** Directrice de thèse
- *Directrice de recherche, IM2NP, CNRS, Marseille*
- **FAVRE Luc** Co-encadrant thèse
- *Maitre de conférences, IM2NP, CNRS, Marseille*
- **RONDA Antoine** Co-encadrant de thèse
- *Ingénieur de recherche, IM2NP, CNRS, Marseille*
- **HOUEL Arnaud** Examineur
- *Docteur, Manager senior à Orsay Physics*

Affidavit

I, undersigned, Imène GUELLIL, hereby declare that the work presented in this manuscript is my own work, carried out under the scientific direction of Isabelle BERBEZIER, Antoine RONDA, Luc FAVRE and Arnaud HOUEL, in accordance with the principles of honesty, integrity and responsibility inherent to the research mission. The research work and the writing of this manuscript have been carried out in compliance with both the French national charter for Research Integrity and the Aix-Marseille University charter on the fight against plagiarism.

This work has not been submitted previously either in this country or in another country in the same or in a similar version to any other examination body.

Place Marseille, date 7 juillet 2022



Cette œuvre est mise à disposition selon les termes de la [Licence Creative Commons Attribution - Pas d'Utilisation Commerciale - Pas de Modification 4.0 International](https://creativecommons.org/licenses/by-nc-nd/4.0/).

Liste de publications et participation aux conférences

1) Liste des publications¹ réalisées dans le cadre du projet de thèse :

1. COMBINATION OF EPITAXY AND CONDENSATION TOWARDS THE FABRICATION OF GE PHOTODIODE, I. Guellil, L. Favre, M. Bollani, M. Bouabdellaoui, E. Assaf, M. Abel, M. Abbarchi, A. Ronda, Olivier Gourhant, Fabien Deprat, Christophe Duluard, Anne-Flore Mallet, P. Vennéguès, J.N. Aqua, Berbezier, soumis dans « Applied Surface Science ».
2. FIB NANOPATTERNING FOR PHOTONIC APPLICATIONS, I. Guelil, I. Berbezier, M. Bollani, A. Ronda, L. Favre, en préparation

2) Participation aux conférences² et écoles d'été au cours de la période de thèse :

1. Poster : au GDR PULSE : « Processus ULtimes de l'épitaxie de SEMI-conducteurs » : du 1 au 4 Juillet, 2019 à Polytech Clermont Ferrand.
2. Poster: à la conférence international PULSE durant l'école d'été, du 2 au 8 Juliet 2021 par "the French National Research Network (GDR) sur la thématique d'épitaxie des semiconducteurs à Porquerolles.

¹ Cette liste comprend les articles publiés, les articles soumis à publication et les articles en préparation ainsi que les livres, chapitres de livre et/ou toutes formes de valorisation des résultats des travaux propres à la discipline du projet de thèse. La référence aux publications doit suivre les règles standards de bibliographie et doit être conforme à la charte des publications d'AMU.

² Le terme « conférence » est générique. Il désigne à la fois « conférence », « congrès », « workshop », « colloques », « rencontres nationales et/ou internationales » ... etc.

Indiquer si vous avez fait une présentation orale ou sous forme de poster.

Résumé

Les boîtes quantiques (QD) semiconductrices ont montré de grandes possibilités d'application pour de nombreuses applications allant des systèmes de la microélectronique à la photonique et à l'optoélectronique. Elles peuvent être utilisés dans les transistors à un électron, les diodes électroluminescentes (LED), les photodétecteurs, les lasers, les sources d'émission à photon unique, l'informatique quantique. De plus, les QD ont des propriétés optoélectroniques qui changent en fonction à la fois de leur taille et de leur forme. Elles peuvent avoir en particulier des propriétés très différentes des semi-conducteurs massifs et présenter des structures de bande et une bande interdite ouvrant sur de nouvelles applications. La densité et la taille des boîtes quantiques, dépendent du procédé de fabrication et sont adaptés en fonction des applications visées. Notre intérêt à travers cette étude est de développer un processus d'élaboration des QD de silicium-germanium (SiGe) avec des compositions allant du Si pur au Ge pur, et permettant d'obtenir des QD semi-conductrices et de tailles suffisamment petites pour l'obtention de confinement quantique. Pour cela, nous avons utilisé une combinaison de différentes techniques : l'épitaxie par jets moléculaires, la lithographie ionique par faisceau d'ions focalisés (FIB) et le démouillage solide hétérogène. Dans ce contexte, la finalité de cette recherche est de développer un nouveau FIB qui soit couplé au bâti d'épitaxie par jets moléculaires, donc sous ultra-vide, pour la fabrication de nano-gravures totalement dénuées de pollution et aux caractéristiques variables et parfaitement contrôlées (taille, densité, profondeur). Les nano-gravures sont réalisées par lithographie FIB en utilisant des ions non polluants (typiquement dans le cas envisagé dans cette thèse : Si et Ge) dans des substrats issus de la microélectronique. Pour ces raisons, notre choix s'est porté sur la gravure de substrats composés de couches de SiGe épitaxiées sur du Silicium-sur-Isolant (SOI). La morphologie des nano-gravures obtenues est ensuite caractérisée in-situ par microscopie électronique à balayage (SEM), et la profondeur est déterminée par des caractérisations ex-situ par microscopie de force atomique (AFM). Les nano-gravures réalisées par FIB en utilisant des sources d'ions d'alliage métallique liquide (LMAIS) filtrées en énergie, ont été comparées d'une part aux gravures plasmas avec He et Ne et d'autre part aux gravures obtenues par lithographie électronique (EBL).

En ce qui concerne les applications, nous nous sommes intéressés d'une part à la fabrication d'émetteurs de lumière dans des enclumes de diamant par implantation ionique FIB des centres colorés SiV et GeV. Ces implantations ont été réalisées en faisant varier le courant jusqu'à des valeurs extrêmement faibles (de quelques fA au pA) en utilisant des sources LMAIS de AuSi

et de AuGe avec discrimination isotopique de Si et Ge. Dans le même contexte, un objectif a été de former des centres SiV dans des substrats ultrafins de SOI (UT-SOI). Des caractérisations par spectroscopie de photoluminescence des pics de SiV sont aussi présentées.

Le travail de thèse est présenté dans ce rapport de la façon suivante : après une *introduction générale* présentant le contexte global et les enjeux de mes recherches, le *premier chapitre* est consacré à un état de l'art sur les configurations des microscopes FIB et sur leurs applications pour la nano-structuration d'une façon générale. Un bref historique sur l'évolution de la FIB est rapidement rappelé, suivi d'une description des colonnes FIB conventionnelles, des sources et des interactions ion-matière et électron-matière. Dans une deuxième partie de ce chapitre je donne quelques exemples d'applications du FIB, en partant de l'imagerie et la tomographie 3D, la préparation des lamelles de microscopie électronique en transmission (TEM), la réalisation de nano-gravures par lithographie ionique et l'implantation localisée pour la création de défauts précisément positionnés. Le *deuxième chapitre* est consacré aux principes généraux de la lithographie à écriture directe par FIB, en se focalisant sur les sources de type LMAIS. J'expose en particulier les aspect instrumentaux et expérimentaux de cette étude, avec une présentation des stations à double faisceaux utilisées au cours des différentes expériences : la station Lyra et le prototype Nanospace en cours de développement chez Orsay Physics (OP), utilisant des sources AuGe et AuSi respectivement. Ici, je donne une explication détaillée des composants de chaque colonne et de leurs alignements mécanique et optique afin de pouvoir séparer les différentes espèces chimiques présentes pour les applications de nano-fabrication visées (nanostructuration / implantation). Le *troisième chapitre* expose les différentes expérimentations réalisées durant cette thèse. Une première partie concerne le processus de fabrication des émetteurs dans le diamant et dans le silicium, et la formation de centres colorés de SiV et GeV par la combinaison de procédés d'implantation FIB et de traitements thermiques pour leur activation et créer des bits quantiques (Qbits). Les défauts sont créés soit dans une enclume de diamant, soit dans des substrats UT-SOI. Dans ce dernier cas, il s'agissait aussi de créer les défauts avec du silicium purifié en utilisant l'isotope ^{28}Si qui est stable et n'interfère pas avec le qubit, contrairement aux isotopes naturellement présents dans le silicium. Les défauts créés sont ensuite caractérisés en collaboration dans d'autres laboratoires par spectroscopie de photoluminescence (PL).

Mots clés : FIB, MBE, dual-beam FIB-SEM, nano-structuration, implantation ionique, boîtes quantiques, émetteurs de lumière, LMAIS, Si, Ge, démouillage.

Abstract

Semiconductor quantum dots (QDs) have shown great potential for many applications ranging from microelectronic systems to photonics and optoelectronics. They can be used in one-electron transistors, light-emitting diodes (LEDs), photodetectors, lasers, single-photon emission sources, quantum computing. Moreover, QDs have optoelectronic properties that change according to their size and shape. In particular, they can have very different properties from bulk semiconductors and exhibit band structures and band gap opening new applications. The density and size of quantum dots depend on the fabrication process and are adapted according to the targeted applications. Our interest in this study is to develop a process for the elaboration of silicon-germanium (SiGe) QDs with compositions ranging from pure Si to pure Ge, and allowing to obtain semiconducting QDs with sufficiently small sizes to obtain quantum confinement. For this purpose, we have used a combination of different techniques: molecular beam epitaxy, focused ion beam lithography (FIB) and heterogeneous solid state dewetting. In this context, the aim of this research is to develop a new FIB coupled to the molecular beam epitaxy growth chamber. The FIB equipment should then be under ultra-high vacuum, for the fabrication of pollution-free nano-patterns with variable and perfectly controlled characteristics (size, density, depth). The nano-patterns are made by FIB lithography using non-polluting ions (typically in the case considered in this thesis: Si and Ge) in substrates from the microelectronics industry. For these reasons, we have chosen SiGe on Silicon-on-Insulator (SGOI) substrates consisting of SiGe layers epitaxied on SOI. The morphology of the obtained nano-patterns is characterized in-situ by scanning electron microscopy (SEM), and the depth is determined by ex-situ characterizations by atomic force microscopy (AFM). The nano-patterns made by FIB using energy-filtered liquid metal alloy ion sources (LMAIS) have been compared to plasma millings with He and Ne on the one hand and to patternings obtained by electron lithography (EBL) on the other hand.

Regarding the applications, we were interested in the fabrication of light emitters in diamond anvils by FIB ion implantation of SiV and GeV colored centers. These implantations have been performed by varying the current down to extremely low values (from a few fA to pA) using AuSi and AuGe LMAIS sources with Si and Ge isotopic discrimination. In the same context, one objective has been to form SiV centers in ultra-thin SOI substrates (UT-SOI). Photoluminescence spectroscopy characterizations of SiV peaks are also presented.

The thesis work is presented in this report as follows: after a general introduction presenting the global context and the challenges of my research, the first chapter is devoted to a state of the art of the conventional FIB microscopes configurations and their applications for nanostructuring in general. A brief overview of the history of the FIB evolution is quickly recalled, followed by a description of conventional FIB columns, sources and ion-matter and electron-matter interactions. In a second part of this chapter I give some examples of FIB applications, starting from 3D imaging and tomography, preparation of transmission electron microscopy (TEM) slides, realization of nanopatterns by ion lithography and localized implantation for the generation of precisely positioned defects.

The second chapter is devoted to the basics of direct writing lithography by FIB, focusing on LMAIS sources. In particular, I present the instrumental and experimental aspects of this study, with a presentation of the dual beam stations used in the experiments: the Lyra station and the Nanospace prototype under development at Orsay Physics (OP), using AuGe and AuSi sources respectively. I give a detailed description of the components of each column and their mechanical and optical alignments in order to efficiently separate the different chemical species present for the targeted nanofabrication applications (nanostructuring / implantation).

The third chapter presents the different experiments performed during this thesis. A first part concerns the fabrication of emitters in diamond and silicon, and the formation of colored SiV and GeV centers by the combination of FIB implantation and thermal treatments; the latter serves for the activation of the defects and the generation of quantum bits (Qbits). The defects are created either in a diamond anvil or in UT-SOI substrates. In the latter case, the defects were also created with purified silicon using the ^{28}Si isotope which is stable and does not interfere with the qubit, unlike the isotopes naturally present in silicon. The defects are then characterized in collaboration with other laboratories by photoluminescence spectroscopy (PL).

Keywords : FIB, SEM, nanopatterning, ion implantation, Quantum Dots (QD), light emitters, LMAIS, Si, Ge, Diamond, dewetting.

Acknowledgements

I would like to thank the ANR for the CIFRE funding of this thesis, the IM2NP laboratory located at the Saint Jérôme campus of Aix Marseille University, as well as the company ORSAY PHYSICS for having welcomed me warmly in their premises.

I would like to thank mainly my thesis director, Isabelle BERBEZIER, for her patience, her availability, her trust and her essential advice, as well as my co-supervisors Antoine RONDA and Luc FAVRE, for their availability throughout my thesis, their explanations and the rich scientific discussions.

I would also like to thank my supervisor from Orsay Physics, Arnaud HOUEL, for his welcome at the company and for the work we did together on the prototype and the diamond implantations and the various experiments. For his help during the resolution of the bugs and above all during my period of insertion in the group.

I also thank Damien and Alexandra for the training on the prototype in Orsay.

I thank infinitely all the people of the R&D building of Orsay Physics and the production department for their sympathy and help: Morgan, Julien Sebasti, Arthur & Charles and all the BE Soft engineers, JBM, JBF, Mathieu, Olivier, Axel, Thierry, Alexandre, Julien Campanini, all Jeans, Romain & Fabrice from the Clean-room, Frédéric, Andrea, Julien, Valérie, David, Elodie, Anne, Pierre, Avihay, Greg, Jeremy.... etc.

I would like to thank Marie Planchet for all the administrative procedures during my thesis.

I thank all the staff of Tescan France as well as the staff of Tescan analytics, with whom I was able to work for the AFM and the TEM preparation and with whom I spent pleasant moments.

I particularly thank Amandine and Thomas for the whole days of TEM preparation and the rich scientific discussions and their expertise and sympathy, I will never forget your help!

I would also like to thank the permanent and non-permanent members of the NOVA team, with whom I was able to work and discuss different themes: Marco ABBARCHI, David GROSS, Mathieu KOUDIA, Mathieu ABEL, Drisse HANNANI, JB CLAUDE and Momo BOUANDELLAOUI for the work we shared and advises; it was a pleasure to work with you!

I warmly thank my friends: Radia, Yasmin and Youba who just had a beautiful twin with whom I lived unforgettable moments, their support throughout my thesis. I also thank my friends from Im2np at St Jérôme and Toulon, Ecole Supérieure des Mines and Polytec...etc. I thank all the people I met and worked with especially Hadjer Soltani, Majdi, Joseph, Anes, Ayoub, Hassan, Ismail, Hamza, Noureddine, Ilyes, Mouad, Selma, Anasse, and from British Columbia Fateh & Adrian for the precious advises during all these years; you are all engraved in my memory!

*I would particularly like to thank **my parents** for their love and encouragement during my thesis, their moral support, their help, my sister my sweetheart “**Maïssa Djanette**” and my brothers “**Houssein Eddine**” & “**Mohamed**”, I am lucky to have you, you are my real treasure!*

Finally, I am very proud of myself for having accomplished this work despite the difficulties encountered during these four years of thesis with the period of health crisis.

Now, I could say: ***It was not easy but I did it & after the effort comes the comfort!***

Imène

Résumé de thèse vulgarisé

Les nanosciences s'ouvrent depuis quelques années à la recherche de nanostructures hybrides combinant différentes catégories de matériaux (tels que semi-conducteurs / matériaux organiques / oxydes métalliques) afin d'intégrer de multiples fonctionnalités dans une même structure dans le but de créer de nouvelles propriétés. Cette thématique innovante nécessite d'associer différentes approches Bottom-up et top-down pour synthétiser ces nanostructures hybrides multifonctionnelles. A la problématique complexe de la synthèse de ces nanostructures est associée une difficulté majeure rencontrée actuellement de leur caractérisation à l'échelle nanométrique en 3D, caractérisation essentielle pour le contrôle de leur morphologie, composition, taille et configuration géométrique. Face à ce défi des nanosciences dans leur globalité, il est devenu nécessaire de développer de nouvelles techniques et compétences dans le domaine de la nano-fabrication et de la caractérisation 3D ultime des nanomatériaux complexes.

Depuis plusieurs années, il y a une demande croissante des laboratoires de recherche, publics comme privés, pour des équipements couplant des techniques de nano-structuration sans masque faisceaux d'électrons et d'ions focalisés et de caractérisation à l'échelle nanométrique par microscopie, ou tomographie, associant les procédés induits (EBID, FIBID, ...) fonctionnant en environnement UHV (Ultra High Vacuum). En effet, cet environnement UHV répond à la nécessité de propreté absolue des substrats et constitue le seul moyen de rendre fonctionnels les dispositifs ainsi élaborés dans des domaines aussi variés que la micro-nanoélectronique, l'optoélectronique, le photovoltaïque, la spintronique, la plasmonique... L'UHV permettrait aussi à terme une connexion entre la nano-fabrication FIB et la croissance par épitaxie par jets moléculaires (MBE) est l'unique voie pour fabriquer des structures 3D en alternant des étapes de gravure et de dépôt de nanostructures empilées.

Dans ce contexte, en ce qui concerne la réalisation de nanostructures à base de Si, le principal challenge pour l'industrie microélectronique et pour les chercheurs qui l'accompagnent, est d'être capable de réaliser une optoélectronique entièrement intégrée à base de silicium. Cela nécessite de convertir les matériaux à base de Si en absorbeur/émetteur efficaces de lumière, ce qui n'est pas le cas des matériaux massifs IV-IV qui ont une bande interdite indirecte. De nombreuses voies ont été testées, sans succès à ce jour. Une des pistes les plus prometteuses pour modifier la structure de bande de ces matériaux et obtenir une bande interdite directe est de combiner les effets de la fonctionnalisation chimique et du confinement quantique dans les

nano-objets. Différentes démonstrations théoriques ont permis de mettre en évidence des géométries de structures qui ne peuvent être obtenues que par une combinaison d'étapes Top-Down (gravure) et Bottom-Up (croissance). Le problème de cette combinaison est l'introduction de contaminants et de défauts, entre les étapes (gravure/croissance), qui sont rédhibitoires pour la fabrication ultérieure de composants électroniques fiables.

Par ailleurs, une autre approche est de développer des dispositifs ayant des fonctionnalités optique et optoélectronique n'existant pas à ce jour. Parmi les nouveaux dispositifs déjà explorés les avancées les plus spectaculaires concernent les composants nanophotoniques. Ils constituent de nouvelles classes de dispositifs susceptibles de répondre aux défis actuels de l'optoélectronique. Les composants photoniques diffusent dans de nombreux secteurs stratégiques tels que les télécommunications, la production industrielle, le diagnostic médical, le suivi environnemental et l'aérospatial. Afin de réaliser des nano-sources très efficaces, il faut contrôler le positionnement de nano-motifs au sein ou au-dessus de leur cavité, et être capable d'y localiser (moduler) des boîtes (puits) quantiques présentant des propriétés optiques performantes.

Par le passé, pour répondre à ce type de besoins, Orsay Physics a fourni des colonnes FIB et SEM UHV à des laboratoires de recherche qui ont tenté de les combiner à des chambres de croissance. La limitation de ces adaptations «home made» est liée, notamment, à l'absence des conditions environnementales adéquates, ce qui empêche de tirer parti des performances de chacun des équipements ainsi «additionnés ». C'est ainsi que la résolution des images ou de la gravure perd plusieurs ordres de grandeur par rapport aux spécifications garanties dans un environnement favorable et optimisé en termes de vibrations et de bruits phoniques ou électromagnétiques. De plus les propriétés électroniques et optiques des hétérostructures ainsi créées par des outils non couplés sont en général décevantes (hormis les cas où les hétérostructures subissent différentes étapes de nettoyage longues et difficilement industrialisables). Cette démarche d'adaptation « home made » résultait de l'absence de solutions intégrées et industrielles sur le marché. Il y a donc une fenêtre de marché à occuper pour une station ultravide, modulaire, comportant un panel de nano-outils, et potentiellement couplable à une chambre d'épitaxie par jets moléculaires (MBE).

Le but de cette thèse concerne donc le développement d'un nouvel équipement sous ultra-vidé pour la fabrication, l'observation et l'analyse de nano-objets pour des applications en microélectronique. L'équipement doit être sous UHV pour permettre son intégration ultérieure à un bâti d'épitaxie.

De formidables progrès en nano-fabrication à grande échelle ont été réalisées pour la réalisation de composants micro- nano- et opto-électroniques miniaturisés. Les procédés s'appuient sur des infrastructures et des équipements de plus en plus coûteux. Ceci a poussé les chercheurs et les fabricants à trouver des compromis entre les propositions de nouveaux composants et le développement et/ou l'amélioration des procédés de production massive, de grande complexité, des composants plus performants mais à bas coûts. Les chaînes de production utilisent les matériaux semi-conducteurs et principalement le silicium, qui a permis l'essor de la micro-électronique, avec notamment des puces électroniques basées entre autres sur des transistors de plus en plus petits (jusqu'à des nœuds de 28nm actuellement), avec en parallèle une quête constante d'amélioration de leurs performances, tout en essayant de garder un coût de procédé constant.

Parmi les approches de nano-structuration utilisées dans l'industrie des semi-conducteurs, la lithographie est la technique la plus utilisée. Elle se réfère à l'écriture de motifs aux dimensions ajustables à volonté et contrôlées pour la fabrication de différentes structures complexes. Le procédé de lithographie varie selon la manière dont les motifs sont transférés sur la surface : lithographie optique qui utilise des graveurs à faisceau laser, lithographie par nano-impression, lithographie par faisceau d'électrons (EBL) et par faisceau d'ions à particules chargées (IBL). Ces différentes techniques passent par l'impression des motifs sur des résines en utilisant des masques. Cependant, pour la fabrication de dispositifs à test unique ou en faible série, les masques à haute résolution sont coûteux, d'où l'émergence de l'écriture directe (sans masque) d'une résine photosensible, avec une variété de techniques, les plus utilisées étant à nouveau la lithographie optique et l'EBL. Contrairement à la lithographie optique à écriture directe qui n'est pas vraiment considérée comme une méthode de nano-écriture en raison de la taille micrométrique du motif ($> 0,6 \mu\text{m}$), l'EBL est considérée comme une méthode de nano-écriture polyvalente puisqu'elle utilise un faisceau d'électrons focalisé d'un diamètre allant jusqu'à 1 nm et une taille minimale du motif dans la résine de ~ 10 nm, donnant ensuite une taille de gravure plus élevée et dépendante du matériau gravé [3]. Plus récemment un grand nombre de recherches se sont penchées sur la lithographie par faisceau d'ions (IBL). Il s'agit d'une méthode moins connue malgré une promesse de résolution ultime inégalée ($\sim 10\text{nm}$) [1,2]. De la même manière que l'EBL, l'IBL a montré de nombreuses possibilités d'applications, depuis la nano-fabrication avec l'écriture de motifs dans une couche sacrificielle pour déposer ou fraiser localement, jusqu'à la nano-structuration de substrats pour l'auto-organisation de nano-objets et l'implantation ionique locale pour la création de défauts locaux positionnés à volonté. L'utilisation de sources d'ions de métaux liquides (LMIS) permet d'obtenir à la fois une très

bonne résolution (puisque le faisceau d'ions focalisé possède un diamètre ultime de l'ordre du nm), similaire, voire supérieure à l'EBL, mais aussi une vitesse d'écriture plus élevée que l'EBL puisque l'exposition des résines est plus rapide, en raison de l'énergie plus élevée du faisceau d'ions qui contient des ions de masse supérieure.

Finalement, il est aussi possible de graver directement les matériaux par FIB, sans passer par une résine, ce qui permet encore d'améliorer à la fois la résolution et le temps de gravure ; le temps de gravure par pixel étant très court (avec des tailles de pixel et de faisceau qui sont du même ordre de grandeur). Pour ces raisons, l'IBL propose des spécifications supérieures à la lithographie électronique, même pour une taille de faisceau similaire.

Par ailleurs, une autre application du FIB est l'implantation ionique locale. Dans ce cas, les motifs sont générés à la surface de l'échantillon puis insérées dans le procédé général de fabrication incluant d'autres étapes de métallisation, dopage, oxydation, etc. pour la réalisation des dispositifs finaux [4]. Il a par exemple été démontré que des centres émetteurs de lumière pour les technologies quantiques (Qbits) basés sur certains types spécifiques de lacunes, peuvent être créés par FIB à partir de nano-cavités dans le diamant [5]. De la même façon, des substrats de silicium sur isolant ultra-minces (UT-SOI) ont aussi été utilisés pour réaliser le même type d'émetteurs de lumière pour des dispositifs optoélectroniques reposant sur la génération, la modulation et la détection de la lumière avec des applications dans les écrans, le stockage de données, les capteurs, la communication par fibre optique et les cellules solaires.

Dans ce contexte, le travail de thèse visait à étudier et à démontrer les nouvelles potentialités de techniques basées sur l'association dans un même équipement de faisceaux d'ions et de faisceaux d'électrons, pour la fabrication et l'analyse tomographique 3D de différents systèmes complexes, en s'appuyant sur une plateforme prototype sous ultra-vide (UHV).

L'émergence des techniques multifaisceaux intégrant source d'électrons (FEB) et source d'ions (FIB) et leur couplage à un bâti d'épitaxie UHV (MBE), ouvre des combinaisons remarquables de procédés incluant la nano-structuration, la reprise d'épitaxie, la métallisation, l'adressage, l'observation et l'analyse tomographique 3D (FIB/SEM) à l'échelle nanométrique. De plus, afin de prendre en compte la complexité et les dimensions réduites des nanostructures en cours de synthèse actuellement, il est impératif de développer la nouvelle génération d'équipements en environnement UHV qui permet de s'affranchir de la contamination inhérente au système à vide standard (HV) ce qui serait rédhibitoire pour ce type d'échantillons novateurs.

Dans ce travail, le but est de valider le développement d'une nouvelle station multifaisceaux UHV par OP (Nanospace) par l'élaboration et la caractérisation de différentes nanostructures.

La station Nanospace est constituée d'un faisceau FIB servant à la fois à la nano-structuration et à la caractérisation (gravure, coupe et reconstruction 3D) et d'un faisceau d'électrons (SEM) très haute résolution pour la visualisation des structures de taille ultime. Les paramètres (énergie, courant et taille de sonde) du faisceau d'ions primaires jouent un rôle majeur non seulement pour la gravure des échantillons mais également pour les signaux (en ions ou en électrons secondaires). De manière générale, il est nécessaire de choisir un couple « faisceau primaire (FIB ou SEM) /détecteur » en fonction de la fonction désirée.

Un certain nombre d'études préliminaires sur des nanostructures modèles permettent d'établir un cahier des charges exhaustif pour l'optimisation de la plateforme : distance de travail, encombrement, géométrie, sensibilité.... La nouvelle plateforme développée par OP et testée en laboratoire devrait pouvoir être utilisée de façon générique sur différentes catégories de nano-objets uniques ou assemblés en nanomatériaux complexes.

Une des premières tâches était d'analyser les effets des interactions ion/matière avec différents types de matériaux (semiconducteurs, matériaux organiques, oxydes) à la fois pour la nano-structuration FIB et pour les imageries SI.

Dans ce cadre, un point important concerne les effets d'irradiation ionique sur des cibles de très faibles dimensions : à la fois sur la redistribution volumique des éléments induite par le bombardement ionique, sur les défauts engendrés et sur les contraintes créées.

Un autre point important est d'estimer les volumes de matière les plus petits qu'il est possible de graver par FIB-HR UHV et d'observer in situ par SEM. En effet, la gravure FIB et l'imagerie SEM de très petits volumes imposent des contraintes sur les faisceaux primaires et sur les signaux détectés. Il est nécessaire d'avoir un faisceau d'ions bien défini pour une gravure précise mais également une énergie adaptée afin de réduire les dommages (amorphisation) causés par le faisceau incident. L'objectif est donc de déterminer les limites ultimes du système UHV SE, BSE, SI et SE/SI développé par OP.

Dans ce travail de thèse une grande partie du temps a été dédiée à la résolution de problèmes instrumentaux liés au développement difficile (et finalement abandonné) de la station prototype Nanospace chez OP. La partie instrumentale qui devait être réalisée sur quelques mois en début de thèse a donc largement débordé sur la partie applicative concernant la réalisation des nanostructures. Mon travail a donc été principalement consacré à la résolution des problèmes liés au non fonctionnement de la station Nanospace multifaisceaux FIB/SEM. Les nombreuses pannes n'ont pas permis de l'utiliser en bon état dans pour les des applications visées : implantations, gravures et caractérisations tomographiques 3D en temps réel par le SEM. Les tests des spécifications de la colonne FIB n'ont pas non plus pu être réalisés.

Les deux premiers chapitres présentent des revues bibliographiques sur le FIB, la lithographie FIB à écriture directe, les différents types de sources et les applications générales du FIB. Le troisième chapitre présente les résultats obtenus à la fois par implantation ionique et par nano-gravure.

Dans le *premier chapitre*, nous décrivons l'état de l'art de la technologie FIB avec un bref historique de ses développements en considérant les deux configurations de microscope ionique, soit à faisceau unique FIB, soit à double faisceau FIB/SEM. Nous donnerons aussi les spécifications générales des deux colonnes FIB et SEM conventionnelles, leurs composants et finalement une brève revue sur les processus d'interaction des particules chargées ions / solide. La dernière partie est principalement consacrée aux applications du FIB avec d'une part la nano-gravure de motifs et d'autre part l'implantation localisée pour la génération de défauts locaux.

Dans le *second chapitre*, nous présenterons les caractéristiques générales de la lithographie à écriture directe par FIB, et nous nous focalisons sur deux instruments ayant des sources de type LMAIS, le LYRA et la NANOSPACE (en cours de développement chez OP) qui sont généralement équipées de sources AuGe et AuSi. Nous détaillons les sources LMAIS ainsi que les différents composants. Une seconde partie du chapitre concerne les alignements mécanique et optique des colonnes qui sont cruciaux pour séparer les différentes espèces chimiques présentes dans les matériaux. Une troisième partie est consacrée à l'imagerie haute résolution FIB/SEM.

Le *troisième chapitre* expose les différentes expériences réalisées durant cette thèse, pour essayer de valider la station Nanospace qui n'a finalement jamais fonctionné correctement (en raison d'un très grand nombre de bugs entre autres de soft). Je présente en premier lieu le procédé de fabrication des émetteurs de lumière dans le diamant et dans le silicium, à partir de la formation de centres colorés de SiV et GeV. Ils sont réalisés par l'implantations FIB (de Si et de Ge), d'une part dans des enclumes de diamant « Anvil 957 », et d'autre part dans du UT-SOI, suivie par l'activation des défauts par des traitements thermiques. L'efficacité des défauts est finalement caractérisée par la spectroscopie de photoluminescence (PL).

De plus, dans le cas des substrats de UT-SOI les centres SiV sont créés en utilisant des ions de l'isotope unique ^{28}Si . Une première mise en évidence des récents résultats obtenus dans cette étude sont brièvement présentés.

Durant ces expériences, différents paramètres ont été variés : la dose, le courant, le dwell-time, le nombre de scan et le taux de gravure ; une calibration de ce dernier a été faite selon la nature des substrats (SOI et SGOI) et l'isotope ionique utilisé. Un compromis entre ces paramètres a permis d'atteindre nos objectifs de faible profondeur de gravure avec faible courant et faible dwell-time à une forte énergie de FIB.

Dans une deuxième partie, je présente un procédé de fabrication original de QD de Ge enrobés dans du SiO₂ par une combinaison de nano-gravure FIB, condensation et démouillage. La condensation de Ge est effectuée par RTP. Une calibration de la température de condensation est réalisée pour cette étude sur des substrats de SGOI non patternés afin de déterminer les conditions optimales de démouillage de la couche SiGe. Dans un second temps, les calibrations en température du démouillage des couches de SGOI gravées par FIB sont effectuées par SEM après décapage de l'oxyde formé durant la condensation. Les observations ont confirmé la formation et la mise en ordre des QDs de Ge, même si les profondeurs gravées étaient trop importantes et ont dégradé les échantillons. Les résultats ont été comparés à des gravures effectuées avec d'autres types d'ions : He et Ne. Les substrats gravés ont été observés par SEM, AFM et TEM. Malheureusement, la profondeur de pénétration de ces ions a été trop importante par rapport à la profondeur de la couche de SGOI. Les observations TEM faites sur des lignes gravées même à très faibles doses montrent des dégradations importantes. Les résultats ont aussi été comparés aux résultats obtenus par nano-gravure EBL. Ces derniers sont aussi présentés en fin de chapitre.

Comme déjà expliqué, le temps consacré aux expériences et aux caractérisations des structures telles que les préparations de lames par FIB pour les observations TEM, qui sont particulièrement chronophages, a été extrêmement réduit ; pour cette raison, il y aura un nombre limité de caractérisations TEM dans le manuscrit. Elles ont été sélectionnées selon la priorité de l'étude.

Le but de la thèse était double d'une part un but instrumental qui consistait à aider OP pour le développement d'une nouvelle colonne FIB filtrée en masse, de haute résolution avec une grande dynamique de courant afin d'étudier et d'autre part de développer différents types de nanostructures modèles. Ce développement a pour but d'améliorer la technologie FIB filtrée sur les points suivants : la résolution latérale des colonnes équipées d'un filtre de masse, leur dynamique en courant et leur stabilité. Le second but était de valider la nouvelle technologie FIB par la nano-fabrication de deux types de nanostructures : des Qbits et des boîtes quantiques. La finalité étant d'ouvrir la voie vers des mécanismes originaux de fabrication, nous permettant d'étudier des phénomènes photoniques et de transport des électrons dans les structures. Durant

la thèse, était prévue la réalisation d'un démonstrateur (structure active et mesures photoniques correspondantes) ainsi qu'un modèle de composant optimisé.

Les tâches instrumentales que j'ai réalisées pour aider au développement du prototype NANOSPACE, ne sont que très peu décrites dans le manuscrit ; elles ont pourtant accaparé la majeure partie de mon temps, puisque plusieurs problèmes de soft et d'instrumentation (mécaniques, système de vide et de sécurité, etc.) ont été présents tout le long de mon travail de thèse, sans qu'aucune résolution des problèmes n'ait été apportée. Ces problèmes empêchent de façon récurrente le bon déroulement des expériences et nécessitent une intervention directe lorsqu'ils surviennent afin d'éviter les complications et l'arrêt de la machine.

Je liste ci-dessous les principaux problèmes rencontrés, qui se situent donc principalement au niveau du logiciel qui contrôle l'ensemble de la station, ce qui rend la tâche plus difficile malgré les versions qui ont été mises à jour à chaque fois, les principaux problèmes techniques rencontrés sont les suivants : (i) Perte soudaine de communication entre le PC serveur et le PC client, entraînant l'arrêt du logiciel et la perte de contrôle, ce qui nécessite l'arrêt de tout le logiciel et son redémarrage avec la perte de certaines conditions et paramètres sauvegardés ; (ii) mauvais rappel des conditions ou des paramètres par le logiciel, ainsi que des valeurs de FOV spécifiques à chaque objectif et ne suivant pas la variation d'énergie ; (iii) lecture erronée des valeurs réelles selon les instructions qui sont totalement différentes des valeurs saisies et demandées et par défaut mises à 0 ; (iv) problèmes de lecture de pression et de vide liés à l'absence de mise à jour de la carte de vide et de sécurité ; (v) problèmes de source AuSi, à la fois dans sa conception et dans son chauffage inopérant. Ceci nous a obligé à changer de source rapidement et de modifier les conditions limites utilisées lors de mes expériences.

Parallèlement à l'identification de ces problèmes et à leur résolution, j'ai pu faire fonctionner la source AuSi et rechercher les conditions ioniques pour la stabiliser en jouant sur différents paramètres : énergie d'extraction et de suppression avec un courant de chauffage approprié. Cette étape prend beaucoup de temps, avant même de faire l'alignement optique de toute la colonne. C'est seulement après que ces deux étapes principales ont été réalisées, que j'ai commencé la création des presets et la dissociation des espèces chimiques afin de préparer des implantations précises et spécifiques pour les enclumes en diamant.

Un autre problème concernant la partie Filtre de Wien est aussi apparu au niveau du logiciel qui n'affiche pas le spectromètre adapté aux espèces dissociées. Pour avancer dans mes expériences, j'ai effectué la dissociation manuellement en utilisant les documents de référence d'OP. A l'aide de cette dissociation, j'ai travaillé plus avant sur la stabilité de la source AuSi à très faible courant d'émission afin de réduire les aberrations et de pouvoir réaliser des motifs

très petits. J'ai pu ainsi réaliser des motifs d'environ 21 nm de diamètre à un courant d'émission de 1 μ A et un courant de travail de 4 pA. La résolution est très dépendante du courant, puisqu'à un courant d'émission de 5 μ A et un courant de travail de 1,4 pA, les motifs ont un diamètre minimal d'environ 40nm.

Ces motifs sont le résultat de tests visant à optimiser la position du croisement optique par rapport aux ouvertures de la sonde et de la masse. Cette idée nous intéresse pour pouvoir définir nos conditions de travail et optimiser également la taille des spots. Cela nous a permis de travailler d'un côté sur la partie filtre de Wien qui nécessite de tester es tests chaque modification du programme selon le type de mesure souhaitée (tests soit internes, soit externes qui nécessitent alors l'utilisation d'un Keithley qui donne des mesures plus précises mais qui doit être implémenté dans le soft). La partie logicielle pour le spectre posait donc aussi problème, et les données n'ont pu être validées que très tard car les mesures des très petits courants n'étaient pas possibles avec l'électromètre.

Par ailleurs, le pc serveur du rack de la station avec le logiciel du constructeur qui posait des problèmes de communication lors des manœuvres, a finalement dû être changé et l'installation d'un logiciel un peu plus stable qu'avant a pu être finalisée.

En résumé en parallèle au développement du logiciel et à la résolution des problèmes durant les travaux, nous avons réussi à :

- Construire un port métallique spécial pour les échantillons au niveau de la chambre de gravure et de transfert. Ce port métallique permet d'une part de protéger la turbopompe et la pompe ionique de la chambre de gravure et de transfert des échantillons, et d'autre part de gagner du temps en éliminant les risques d'incidents, notamment de casse des échantillons (en particulier des plaquettes de silicium habituellement utilisées) avec pulvérisation de miettes d'échantillons dans les pompes (rédhibitoire pour le fonctionnement des pompes) ;
- Développer plusieurs sources AuSi (Orsay Physics) en jouant avec leurs designs, afin de lever les limitations de chauffage de l'électronique de la plateforme et permettre les tâches applicatives visées. Différentes sources ont créé des incidents internes dans la cartouche lors du chauffage de la source. Pour cette raison, nous avons développé une nouvelle source que nous avons testée de la façon suivante : tests de courant de fuite, recherche des conditions ioniques et de stabilisation, tests d'alignement de l'ensemble de la colonne (source, diaphragmes et lentilles d'objectif) puis création des presets. Le principal problème de ces sources est leur manque de stabilité avec une augmentation de leur courant de chauffage à chaque utilisation, ce qui modifie la résistance interne de la source elle-même, paramètre qui ne peut pas être contrôlé. Ceci entraîne une diminution importante de la durée de vie de la source. En raison de

ce manque de stabilité de la source, j'ai travaillé à la fois pour les implantations et pour les nano-gravures à très faible émission (5 μA et 1 μA) ;

- Optimiser les paramètres de gravure (temps de gravure, dose, vitesse de balayage et courant d'émission) et le positionnement du cross-over par rapport aux ouvertures de la sonde et de la masse pour obtenir une forme plus circulaire et une taille de spot plus petite avec des courants faibles. Ceci a permis d'obtenir des tailles de gravures avec Si^+ et Si^{++} , Au^+ et Au^{++} d'un diamètre minimal ~ 20 nm (et donc un gain très faible par rapport à la colonne Lyra qui permettait déjà d'obtenir des gravures de ~ 25 nm).

- Développer la partie filtre de Wien en utilisant différents types de mesures de courant de travail : (i) mesure interne grossière avec l'électromètre via la capsule de Faraday de la colonne et (ii) mesure externe plus précise en installant un Keithley relié à une platine ou à la Faraday de la colonne qui élimine le bruit. Ceci a permis de fournir un spectre de masse plus résolu et permettant une meilleure identification des espèces chimiques.

En conclusion, le développement de la station Nanospace a été interrompu à la fin de ma thèse. La station n'a jamais été passée sous ultra-vide, et de nombreux problèmes ont persisté jusqu'au démantèlement de la station. La station n'est plus opérationnelle et les deux colonnes ont été dispatchées sur d'autres équipements. Le projet est à l'arrêt.

Contents

Affidavit.....	4
List of publications and conference participation.....	5
Résumé.....	6
Abstract.....	9
Acknowledgements.....	11
Résumé de thèse vulgarisé.....	14
Contents.....	25
General introduction.....	27
I. State of-the-art: FIB Microscope and Nano-structuration.....	31
<i>Introduction</i>	31
I.1. Setup and instrumentation.....	32
I.1.1. Brief History of FIB.....	32
I.1.2. Conventional Focused Ion Beam column.....	34
I.1.3. Focused Electron Beam column.....	38
I.1.4. Ion sources.....	41
I.1.5. Beam Interactions with matter.....	48
I.2. FIB Applications.....	55
I.2.1. 3D imaging and tomography.....	55
I.2.2. TEM lamella preparation.....	58
I.2.3. Nanopatterning lithography.....	59
I.2.4. Ion implantation and Defects.....	60
<i>Conclusion</i>	62
<i>References</i>	63
II. Filtered Focused Ion Beam Column technology.....	69
<i>Introduction</i>	69
II.1. Comparaison and innovation : LYRA & NANOSPACE.....	70
II.1.1. Lyra technology.....	70

II.1.2. Nanospace technology.....	80
II.2. Ion Beam alignment with Wien Filter.....	92
II.2.1. Alignment SEM\FIB.....	92
II.2.2. High resolution FIB/SEM imaging.....	95
<i>Conclusion</i>	97
<i>References</i>	99
III. Results of Ion beam lithography.....	101
<i>Introduction</i>	101
III.1. Ion implantation.....	102
III.1.1. Implanation of SiV and GeV in Diamond.....	102
III.1.2. Implantation of SiV in UT- ²⁸ SOI using ²⁸ Si ⁺	108
III.2. Nanopatterning with Ge ions.....	111
III.3. Ge Condensation process.....	115
III.3.1. Thermal oxidation of Si.....	115
III.3.2. Thermal oxidation of Si _{1-x} Ge _x in RTP.....	117
III.4. Nanopatterning with He and Ne ions.....	121
<i>Conclusion and perspectives</i>	126
<i>References</i>	128
General Conclusion.....	130

General Introduction

At the beginning of this century nanoscience and technology had a revolutionary contribution in many fields, including electronics, material science and optoelectronics. The advancements in epitaxial growth techniques and thin film growth technologies enabled growing epilayers as thin as one atomic layer and realizing high crystalline quality and purity materials for semiconductor devices. Semiconductor devices had a rapid evolution from millimeter-sized devices capable of manipulating electricity (transistors) to micrometer-sized devices that can handle both electricity and light (light-emitting diodes) and now to nanometer-sized devices that can interact directly with individual atoms or molecules at nanometer level (quantum electronics). The study of nanostructures opened a new chapter in fundamental physics. Semiconductor microelectronics, is based on silicon with its highly developed and relatively cheap fabrication techniques. New markets in the fields of high-speed devices, optoelectronics or spintronics are not easily accessible with the available Si devices. New materials and device concepts are required to overcome the physical limitation of the semiconductor Si. The introduction of Si/SiGe heterostructures into main-stream Si technology opened a new degree of freedom via band structure engineering. Today commercial applications are mainly restricted to Si/SiGe hetero-bipolar transistors (HBTs) and metal oxide-semiconductor field effect transistors (MOSFET) devices with selective SiGe epilayers. Intense research and development is under way to provide SiGe nanostructures such as nanowires (NW), quantum dots (QD) and quantum bits (Qbits). Strained layer epitaxy allows for the fabrication of self-organized nanostructures via Stranski-Krastanov (SK) growth mode. However, for further reduction of the size of the integrated circuits and semiconductor devices, the processes must rely on novel nanofabrication techniques. Semiconductor world is currently covering and developing various processes of nanofabrication, especially for the increasingly smaller chips, down to ~20 nm that represent the heart of the electronic. The aim is to improve the performances of the devices, reduce their size, without increasing their cost.

Among the nanopatterning approaches, the photolithography is the most widely used lithography process in the high-volume manufacturing of nano-electronics by the

semiconductor industry. The process commonly uses photo masks and positive or negative photoresists. The positive photoresist become more soluble after exposure to a light source, while on the contrary, the negative photoresists become less soluble after exposure. The patterns are first created on the photomask and they are then transferred to the resist during exposure through the mask. However, for the single test devices fabrication, the high-resolution masks are costly (some tens of k€), consequently direct writing techniques have been rapidly developed. In this thesis, we only refer to the direct writing lithography of wafers and other microelectronic substrates. Different processes of lithography can be distinguished depending on the process sequences and the way the patterns have been transferred onto the surface: optical lithography which uses laser beam writers, nanoimprint lithography and charged particles lithography (electrons and ions). The main difference relies in the reproducibility of the resolution and the speed (low or high-volume) fabrication to fit the micro or nano-devices to be realised. The most widely used techniques are the optical direct-writing lithography and the electron beam lithography (EBL). In fact, optical direct-writing lithography has a pattern size resolution in the μm range ($>0.6\mu\text{m}$) and cannot be really considered as a nanopatterning method. Commonly either UV radiation or X-ray sources are used for mass production, while particle beam lithography is used to modify the material properties. In these techniques, the beam of particles is either e-beam or ion-beam. Dots or holes patterns can be realized with interference patterns by scanning the beams onto the resin, to make a network of periodic lines in two directions at 90° from each other.

EBL is considered as a more versatile nanopatterning method, while the ion beam lithography (IBL) is the less known method although its resolution can be similar [1,2]. Nowadays, for these two techniques, the size of the patterns can reach few tens of nanometers. with a focused electron beam in the nanometer range and a minimum feature size in the e-beam resist of $\sim 10\text{ nm}$ [3]. However, this high resolution results in a very slow process, depending on the exposure time of single scan. For that reason, EBL is limited in a restricted number of applications.

IBL has shown its powerful application from patterns writing of resist layers to metal/oxide local deposition (gas injection system), local milling, and also to local ion implantation and direct defects creation. IBL has the capability to produce high resolution patterns (focused ion beam could have a diameter down to 1 nm) with a higher writing speed than EBL since the exposure of resists is faster due to the higher energy of the ion beam with higher mass. In addition, direct writing FIB can be used directly on the substrate without printing a resin; for

that reasons FIB direct writing is superior to EBL, even with the same beam spot size. It is also a more versatile instrument which can serve to local ion implantation for semiconductor doping [4], and also to other steps of nanofabrication (cutting / repairing) of the devices. The implementation of UHV FIB/FEB dual beam system could also allow the 3D morphological characterization of the nanostructures. Such equipment requires specific applications to be tested: (i) qubits based on vacancy colour-centres from nanocavities in Diamond [5] or Ultra-thin SOI substrates and (ii) quantum dots for optoelectronic devices pillared on the generation, modulation and the detection of light and it manifest in solar cells, displays and data storage, sensors, fibre-optical communication... In our study, we used Si ions and Ge ions generated by LMAIS sources, and used for the formation of specific single photon emitters by the patterning with IBL through dot arrays or different shapes embedded in the crystal cavity, that must be done with the right and precise placement relative to the photonic crystal and other settings that will be presented in the parts of experiments.

In this thesis, the two first chapters are dedicated to bibliographic results about direct-writing lithography employing FIB and the description of the different type of sources. The third chapter presents the experimental results obtained.

The first chapter is devoted to a state of the art on the configurations of FIB microscopes and their applications for nanostructuring in general. A brief history on the evolution of FIB is quickly recalled, followed by a description of conventional FIB columns, sources and ion-matter and electron-matter interactions. In a second part of this chapter, I give some examples of FIB applications, starting from 3D imaging and tomography, preparation of transmission electron microscopy (TEM) slides, realization of nanopatterns by ion lithography and localized implantation for the creation of precisely positioned defects.

The second chapter is devoted to the general principles of direct writing lithography by FIB, focusing on LMAIS sources. In particular, I present the instrumental and experimental aspects of this study, with a presentation of the dual-beam stations used in the different experiments: the Lyra station and the Nanospace prototype under development at Orsay Physics (OP) that use AuGe and AuSi sources respectively. Here, I give a detailed explanation of the components of each column and their mechanical and optical alignments enabling the separation of the different chemical species present for the targeted nanofabrication (nanostructuring / implantation) and nanocharacterization (3D analyses and observations) applications.

The third chapter presents the different experiments performed during this thesis. A first part concerns the fabrication process of emitters in diamond and silicon, and the formation of colored SiV and GeV centers by the combination of FIB implantation processes and thermal treatments to activate them and create quantum bits (Qbits). The defects are created either in a diamond anvil or in UT-SOI substrates. In the latter case, the defects were created with purified silicon, using the ^{28}Si isotope which is stable and does not interfere with the qubit, unlike the isotopes naturally present in silicon. The created defects are then characterized in collaboration with other laboratories by photoluminescence spectroscopy (PL).

References

- [1] Ansari, K. et al., 2004. Fabrication of high aspect ratio 100 nm metallic stamps for nanoimprint lithography using proton beam writing.
- [2] Bell, D.C. et al., 2009. Precision cutting and patterning of graphene with helium ions. *Nanotechnology*, 20(45), p.455301.
- [3] Arshak, K. et al., 2004. A novel focused-ion-beam lithography process for sub-100 nanometer technology nodes. *Superlattices and Microstructures*, 36(1-3), pp.335-343.
- [4] Chekurov, N. et al., 2009. The fabrication of silicon nanostructures by local gallium implantation and cryogenic deep reactive ion etching. *Nanotechnology*, 20(6).
- [5] G. Zhang, Y. Cheng, J.-P. Chou, and A. Gali, Material platforms for defect qubits and single-photon emitters, *Applied Physics Reviews* 7, 031308 (2020).

I. State of-the-art: FIB Microscopes and Nano-structuration

Introduction

The understanding of the structure-composition-process relationships of materials for innovative applications, which relies mainly on small-scale imaging and analysis, is the main reason for the challenge of developing new advanced tools by improving the micro- and nano-machining in materials science and semiconductor industries. The Focused Ion Beam (FIB) system has taken its place among the suite of other instruments, in successfully addressing materials challenges. It still promises to meet the continuing demands at the nanoscale in analytical and forensic laboratories, universities, geological, medical, and biological research institutions [1], manufacturing plants, and more. Moreover, a focused ion beam system combines imaging capabilities like those of a scanning electron microscope (SEM) with a precision machining tool. Besides its utility is not limited to the specimen preparation for TEM observation, but also for other analytical techniques, numerous direct micro- and nano-scale deposition, or materials removal anywhere on a solid surface [2]. Next to the complexity of achieving and characterizing new materials and semiconductors nanostructures, there has been a great interest to using more powerful FIBs technologies such as the Dual-Beam FIB systems that

In this chapter, I review the fundamentals of the Focused Ion Beam (FIB) set-up and instrumentation for direct writing applications. A FIB system consists of an ion focusing column differentially pumped implemented with an electron column for performing high-resolution SEM imaging which avoids the specimen damages that could be caused by the ion beam during imaging. A FIB contains an ion source, extractor, condenser, aperture, stigmation control, and objective lens, a specimen stage, secondary electron/ion detector(s), a gas injection system, and possibly other accessories. The main FIB parameters include the acceleration voltage, dose, spot size, beam current, aperture size, scan pattern, and dwell time. There are no standards for FIB milling parameters such as dose values, that should be tuned as a function of the final goal.

I also describe the basics of the ion beam/matter interaction which controls both the milling and the ion implantation. The interaction of ion beam with a material results in momentum transfer and loss of kinetic energy by ion reflection, ion backscattering, emission of secondary electrons,

secondary ions and neutral atoms, sample heating, electromagnetic radiation. It is the emission of ions which is used for the milling of nanostructures. The incident ions can become implanted into the sample as well. Local implantation is also used and described in the applications part.

In a last part, the most common applications in various scientific domains such as 3D imaging and tomography, TEM lamella preparation, nanopatterning lithography, implantation and defects generation are given as examples.

I.1. Setup and instrumentation

I.1.1. Brief History of FIB

In a famous speech in 1959, Richard Feynman, a Nobel laureate in Physics in 1965, first raised the issue of the limits of miniaturization and further manipulation in a small dimension [3]. This talk entitled “There’s plenty room at the bottom” sketches the basis of a research area, which is known today as ‘nanotechnology’. For this purpose, he proposed a method of writing very small dimensions by sending ions beams issued from a source, in the opposite direction through the lenses of the microscope and focusing them into a tiny spot [4]. This concept was the basis of the work on focused ion beam columns. From here, the applications of FIB have been extended and the development of suitable ion sources with high brightness has been pursued; such sources are known as field emission or "point" sources for producing ion beams that can be focused in a spot with a current density by means of high electric fields; either by field ionization from the gas phase in the case of gas phase field ionization sources (GFIS) or by field evaporation from the liquid phase in the case of liquid metal ion sources (LMIS). In the early 1960's, Krohn conducted research on ion beam formation from a LMIS for use in space [5,6]; he worked on the production of charged liquid droplets for rocket propulsion, then he studied charged droplets formation from a variety of liquids including organic fluids, molten fused salts, and metals [7]. In the early 1970's, the possibility of producing a focused ion beam by the application of field emission ion source was demonstrated by Levi-Setti and al. [8], and by Orloff and Swanson [9,10]. They developed a gas field ionization ion source (GFIS) similar to the one invented by Muller [11] (Figure1.1), that was dedicated to surface analysis by field ion microscopy (FIM).

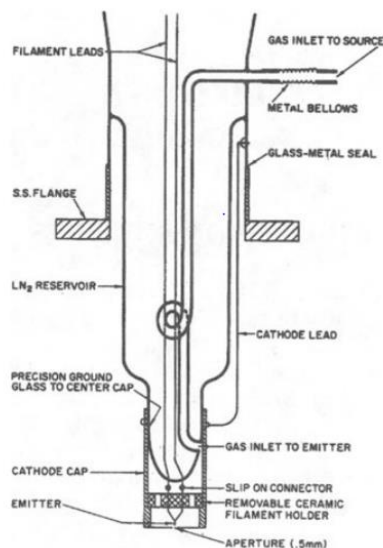


Figure 1.1. Schematic representation of a gun using Gas Field Ionization Source for microprobe work in 1978 by Orloff and Swanson [10].

In the GFIS, the emitter structure is determined beforehand by the shape of a solid field emitter while in the case of the LMIS, a liquid conical structure must be maintained by the balance of electric field stress and surface tension of the liquid; this explains why the LMIS is much more complicated in its description than the GFIS. In fact, GFIS was rapidly abandoned in favour of LMIS because of both low beam currents and the inconvenience of cryogenic operations. Whereas the development of LMIS allowed the use of elements with high vapor pressures such as As [10] and various other elements, smaller angular intensities could also be provided when the current was shared among two or more ion species.

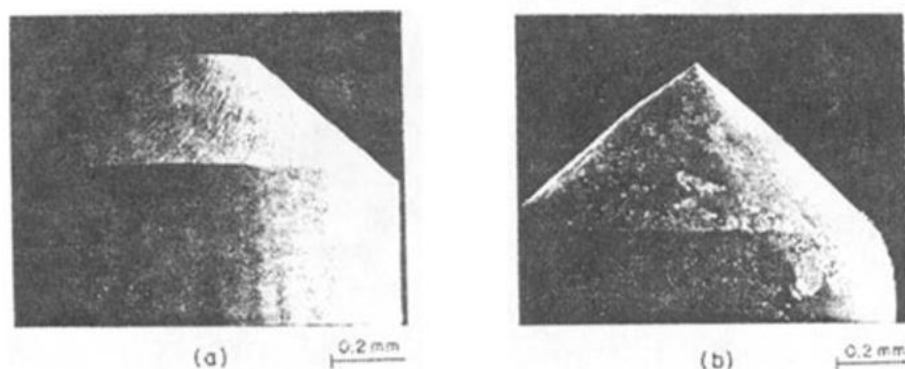


Figure 1.2. SEM observations of the shapes of two LMIS: (a) specially shaped into a tungsten (W) substrate which has been ground to 49° half-angle with an end flat of about $200\ \mu\text{m}$; (b) a frozen Taylor cone shaped into a W substrate covered with an Au film [12].

The first FIB based on LMIS technology was commercialized in 1980 as a performant tool to meet several challenges of materials science, microelectronics and other fields related to nanotechnology [13]. Applications from localized milling, to direct-micro or nano-scale deposition, high precision removal of matter on solid surface, surface analysis [14,15], ion implantation, repairing of integrated circuits, preparation of specimens for transmission electron microscopy (TEM), and micromachining for MEMS or photonics [15,16,17,18].

I.1.2. Conventional Focused Ion Beam column

Basically, the FIB and SEM instruments are similar since they both use a beam of charged particles accelerated from the source gun and focused with lenses electrodes onto the sample surface, except that FIB uses an ion beam and SEM an electron beam, even if high spatial resolution ion images are obtained from secondary electrons generated from the interaction of the ion beam with the target too.

Commonly a FIB column consists of a source of particles, one or more condenser lenses formed with focusing electrodes, probe apertures to adjust the beam current, deflectors allowing the control of the ion beam position on the target holden on a sample stage, gas delivery system for enhancement milling or material deposition, detectors for secondary electrons or ions and a computer to operate the complete station. Since the vacuum system is required to make use of the ion beam (in particular for analysis), the typical FIB system commonly has three vacuum pumping regions, one for the source and ion column, a second for the sample and detectors, and a third for the sample exchange.

Depending on the application and similarly to the SEM, the FIB station can be configured vertically in the case of stand-alone single-beam instruments or tilted at some angle from the vertical in dual-beam platforms (Figure 1.3). It is commonly combined with a SEM but it can also be implemented with another analytical instrument such: Auger electron spectroscopy, transmission electron microscopy, or secondary ion mass spectrometry.

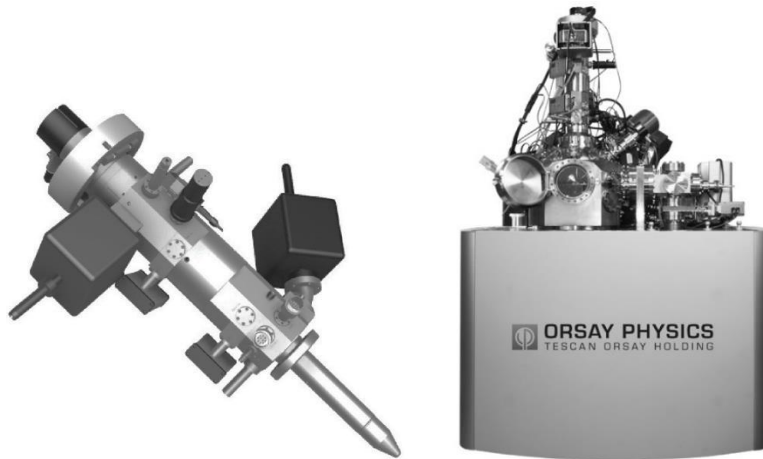


Figure 1.3. Chroma E×B focused ion beam column installed on Nanospace FIB/SEM instrument [19].

Basic FIB column consists of several parts mentioned above and shown on figure 1.4, that can be divided into three main sections:

- The gun section is the top section of the column, it holds the LMIS source in the cartridge with extraction electrodes, and the most used FIB source is the Ga LMIS one.
- The second section is the ion optic and it's the heart of the FIB column which contains the condenser lenses and steering plates for beam adjustment.
- The third part of the column is the objective body part containing the movable apertures, the blanking electrodes, the faraday cup and objective lenses to focus the beam on the area.

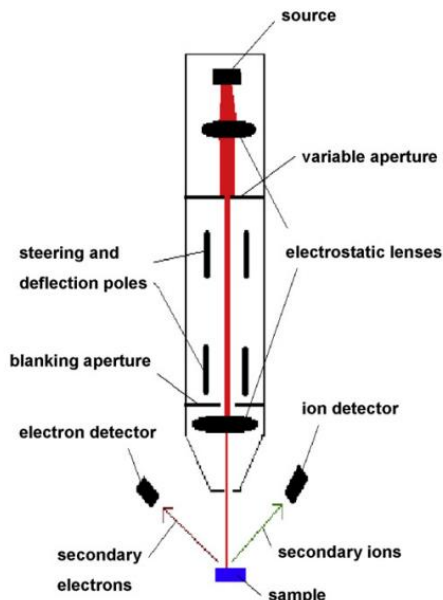


Figure 1.4. Schematic representation of a conventional unfiltered FIB column with a LMIS source [20].

The traditional LMIS ion source of the FIB column is elemental gallium (Ga) among other LMIS sources due to its melting properties, since the liquid metal state is just above room temperature at 29 °C, and also to the combination of low volatility and reactivity with the needle

material, low vapor pressure, and excellent vacuum and electrical stabilities. That's why Ga meets the needs for most FIB applications. Ga properties are grouped in table 1.1.

<i>Properties</i>	<i>Reasons</i>
<ul style="list-style-type: none"> ▪ Low melting point (29.8 °C) ▪ Low volatility at melting point ▪ Low surface free energy ▪ Low solubility of liquid metal in substrate 	<ul style="list-style-type: none"> ▪ Minimises reaction between liquid and substrate ▪ Conserves supply of metal; promotes long source lifetime ▪ Promotes wetting and flow of liquid on substrate ▪ Avoids (i) the dissolution of liquid metal in substrate which alters its resistivity and heating characteristics and (ii) the dissolution of substrate in liquid metal which alters its composition and increases the melting temperature
<ul style="list-style-type: none"> ▪ Can be deposited on an emitter substrate with good mechanical, electrical and vacuum properties 	<ul style="list-style-type: none"> ▪ Substrate emitter must be (i) electrically conductive, (ii) able to withstand high electric fields (~ 10 V/nm), (iii) have low power consumption and (iv) be able to operate in ultimate high vacuum conditions
<ul style="list-style-type: none"> ▪ Good emission characteristics 	<ul style="list-style-type: none"> ▪ High angular intensity (~ 25 μA/sr, I_e = 2 μA), Small energy spread (~ 5 eV, I_e = 2 μA)

Table 1.1. Reasons to choose Ga as ion source and corresponding properties [21].

Other kind of FIB which differs from the conventional FIB column uses a filtered FIB column, and generates a focused beam of different kinds of ions. The source is a liquid metal alloy ion source (LMAIS) based on a low melting temperature alloy, containing the desired elements. It requires the integration of a Wien (or $E \times B$) filter to separate the different ion species produced by the application of a uniform electric and orthogonal magnetic fields and an aperture to select the desired velocity. In chapter II, the Wien filter operation mode will be presented in detail.

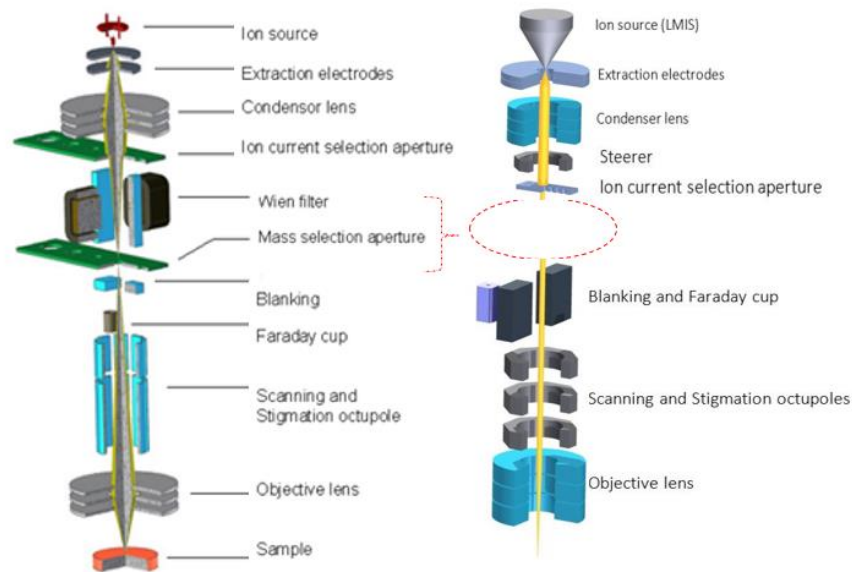


Figure 1.5. Schematic representation of (right) a conventional FIB column employing a LMIS source and ((left) $E \times B$ filtered FIB column employing LMAIS source [OP].

As shown in figure 1.5, the two columns (filtered and unfiltered) are almost the same. The only difference is the presence of a Wien filter followed by mass apertures and the use of a liquid metal alloy ion source (LMAIS) source.

Ion imaging is achieved by the collection of secondary electrons (SE) or backscattered ions which are created from the interaction of the primary ions with the sample surface and detected with the secondary electrons detector (SED). Therefore, the sample should be located in the SEM - FIB intersection so as SE electrons excited by the ions can be detected by a common secondary electron detector (SED). In fact, ion imaging feature is destructive since the specimen is milled by the ion beam. The milling rate depends on the accelerated energy and on the specimen type. In general, hard materials like diamond or titanium are milled at a lower rate than soft materials (like gold and copper). That's why ion imaging is performed with very low ion currents ($\sim 1 - 10$ pA) and for ultra-short durations; however, matter sputtering cannot be eliminated during ion imaging.

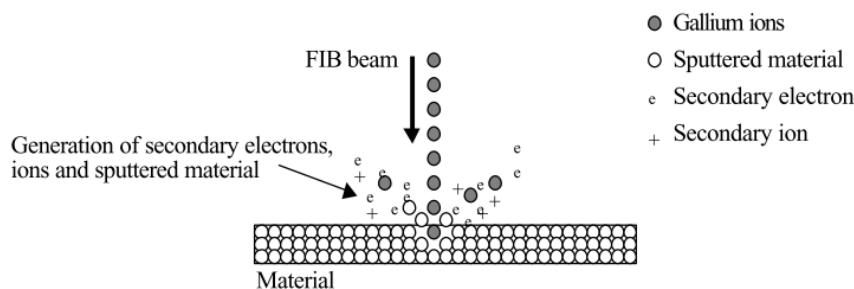


Figure 1.6. Interaction between the Ga ions and matter [23].

Generally, both the imaging and the milling resolution depend on the beam diameter, although the requirements for the two applications are not exactly the same. For the energies, currents, and acceptance angles used in typical FIB systems, the beam spot size is limited mostly by the chromatic aberration that results primarily from the energy spread of the beam due to space charge effects at the ion source and secondarily from the spherical aberration of the lenses. However, the ultimate spatial resolution for FIB imaging is, in fact, limited by the sputtering and is thus sample-dependent. In recent FIB systems, the imaging resolution determined by the sputter-limited signal/noise ratio is usually of the order of few nms. The sample is mounted on a grounded stage with three-axis translation, rotation, and tilt capabilities. FIB also allows a high-resolution investigation of the microstructure of materials in depth (3D tomography) and not only restricted to the study of the very surface of the sample, while most of the high resolution analytical and imaging techniques (like SEM, atomic force microscopy (AFM) and scanning tunnelling microscopy (STM)) only provide information about the surface microstructure of the sample.

I.1.3. Focused Electron Beam column

The field-assisted electron sources are: the room-temperature W emitter (usually called a ‘cold field emitter’); the heated W emitter (generally called a ‘thermal field emitter’, or described as a ‘built-up W Schottky emitter’); and zirconiated W Schottky emitter (often called ‘ZrO/W Schottky emitter’). The sharp W tip has commonly a (100) orientation which appears to be more appropriate for producing a good field electron emission than the classical (110) orientation. The source consists of a W emitter with a sharp tip, an extraction electrode and an acceleration electrode. When a negative voltage is applied, the electric field concentrates on the end of the tip, which gives rise to the emission of electrons by tunnelling effect.

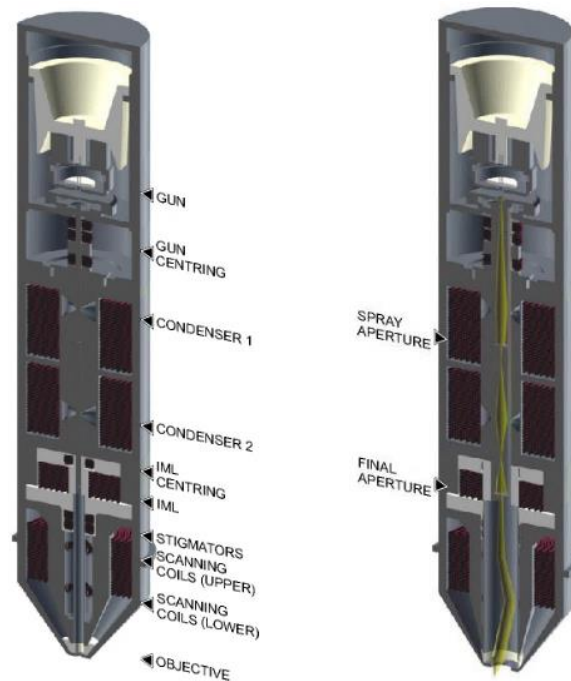


Figure 1.7. Cross section schematic representation of the optical elements of a SEM (from Orsay physics confidential data).

SEM imaging qualities depend on the parameters of the electron beam: spot size, aperture angle and beam intensity. The resolution of the microscope is determined by the spot size as well as usable magnification at stable picture sharpness. The spot is mainly considered circular and has a Gaussian intensity profile; the spot size is specified with half the width of the intensity distribution and could be determined by the demagnification of the primary electron source, optical aberrations of the final lens (objective) and the diffraction aberration of the final aperture. The incident electron beam is cone-shaped and its vertex angle is called the aperture angle: wider is the cone, lower is the depth of focus. In addition, the beam intensity (BI) is the number of electrons passing through the probe in a defined time. The image noise of the electron microscope depends on the number of electrons collected from each picture element. It is necessary to use more time for image scanning at low beam intensity and vice versa.

For more advanced capabilities dual beam systems have been developed for both ion milling and characterization in the same location of a sample. In these systems, an electron column has been incorporated to the ion column in order to use the electron beam for imaging without sputtering. In addition, electron beam deposition of materials can be used to produce very low energy deposition that do not affect the underlying surface of interest as could be done during ion beam assisted deposition. It is possible to add an energy dispersive spectrometry (EDS)

detector to provide elemental analysis, an electron backscatter diffraction detector (EBSD) can also be added to provide crystallographic analysis.

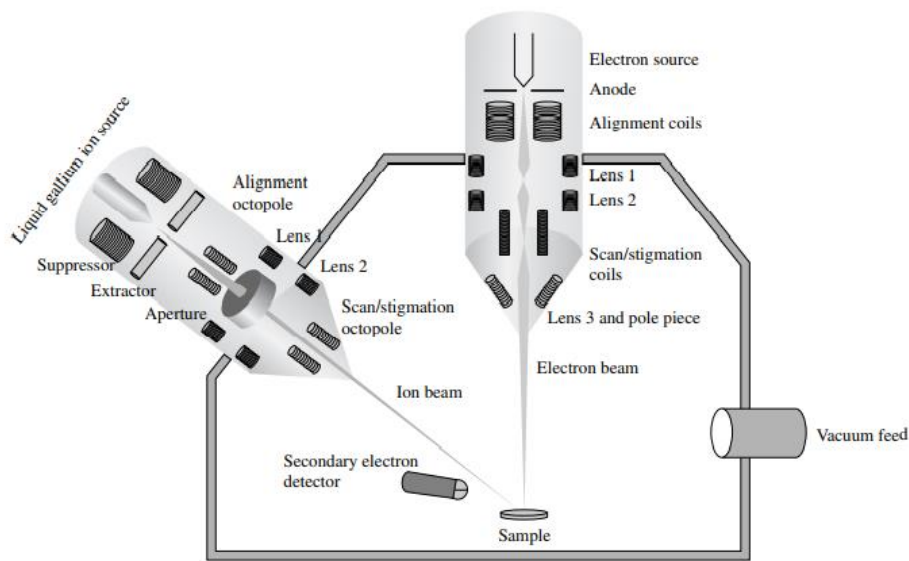


Figure 1.8. Schematic representation of a dual beam FIB-SEM apparatus coupled with a GIS.[26]

Imaging is possible with both ions and electrons since the incident ions produce both secondary electrons and ions. As reviewed in bibliography, scanning ion microscopy (SIM) was the first use of FIB because imaging in some form is always needed to focus the beam, and to see where it is positioned on a sample. Ion imaging is similar to SEM but the contrast mechanisms are different, since the beam which is scanned over the sample, destroys it by sputtering (at a rate determined by the incident beam current and the sputtering yield of the sample); such behaviour limits the imaging time. This destructive interaction, and poorer beam current-probe size characteristics have limited the use of FIB compared to SEM which is widely used for surface imaging. In addition, the resolution of both SEM and FIB are very close, a comparison of their main characteristics is given in Table 1.2. Only in the metrology of resists, ions imaging may be less destructive than SEM.

Particle:	FIB	SEM	Ratio
Type	Ga ⁺ ion	Electron	
Elementary charge	+1	-1	
Particle size	0.2 nm	0.00001 nm	20,000
Mass	1.2×10^{-25} kg	9.1×10^{-31} kg	130,000
Velocity at 30 kV	2.8×10^5 m/s	1.0×10^8 m/s	0.0028
Velocity at 2 kV	7.3×10^4 m/s	2.6×10^7 m/s	0.0028
Velocity at 1 kV	5.2×10^4 m/s	1.8×10^7 m/s	0.0028
Momentum at 30 kV	3.4×10^{-20} kgm/s	9.1×10^{-23} kgms	370
Momentum at 2 kV	8.8×10^{-21} kgm/s	2.4×10^{-23} kgm/s	370
Momentum at 1 kV	6.2×10^{-21} kgm/s	1.6×10^{-23} kgm/s	370
<i>Beam:</i>			
Size	nm range	nm range	
Energy	up to 30 kV	up to 30 kV	~
Current	pA to nA range	pA to μ A range	~
<i>Penetration depth:</i>			
In polymer at 30 kV	60 nm	12000 nm	0.005
In polymer at 2kV	12 nm	100 nm	0.12
In iron at 30 kV	20 nm	1800 nm	0.11
In iron at 2 kV	4 nm	25 nm	0.16
<i>Average signal per 100 particles at 20 kV:</i>			
Secondary electrons	100–200	50–75	
Back-scattered electron	0	30–50	0
Substrate atom	500	0	infinite
Secondary ion	30	0	infinite
X-ray	0	0.7	0

Table 1.2. Quantitative comparison of FIB and SEM columns characteristics (from [26]).

I.1.4. Ion sources

I.1.4.1. Classification

The ion source has been developed through mass spectrometry and ion implantation for semiconductor manufacturing. It is the most important component of the system. It is chosen depending on the application: ion implanters need high current sources for semiconductor manufacturing, whereas to avoid Ga implantation [27], new type of ion source has emerged, that makes use of solid electrolyte ion sources promising high probe current and further micromachining in high speed [28,29], ionic liquid ion sources for the possibility of producing very diverse molecular ions in terms of mass, composition and properties [30,31]. According to their physical basics, ion sources could be divided into four main groups as below:

i. Electron bombardment ion sources

They represent the most used ion sources in low energy accelerators (<500keV); in this kind of sources the electron beam interacts with solid or gas phase atoms or molecules to produce ions. The gas molecules in the irradiated volume become ionized under electron bombardment

without contamination. These sources are widely used in mass spectrometry but they are not common in ion lithography due to the low currents. They have been used for the production of low-energy beams of noble gas ions, such as He^+ and Ar^+ , as well as for H^{2+} and N^{2+} (Dworetsky et al., 1968).

ii. Gas discharge ion sources

They are mainly used in high-energy accelerators and ion implanters for semiconductor manufacturing. These sources employ either capacitively coupled plasma, inductively coupled plasma or microwave-induced plasma or electric discharge to generate ions. However, the glow discharge of a gas at low pressure or spark ionization of a solid sample is another alternative to create ions from gas discharge and emitted over a larger gas volume but with high ion current and therefore they are not suitable for focused beams but interesting sources for ion lithography.

iii. Field ionization sources

Field ionization sources (admitting non-reactive ions such as noble gas), are based on the adsorption of ions from tip through the adsorption of the gas molecules on the surface of sharp needle tip. Adsorption may be enhanced by cryogenic cooling of the tip, followed by the application of high electric at the tip apex for their ionization. Field ionization is observed when a gas is admitted at low pressure (0.01 - 1 mtorr) in the region of the field emitter, to supply the atoms or molecules to be ionized; the emitter is cooled to cryogenic temperatures to maintain a reasonable density of atoms in the high field region (for maximum current the field emitter should be cooled to the boiling point of the gas used). The supply of molecules to be ionized depends on the gas pressure, the temperature of the emitter and the gas and polarization forces which attract the molecules to the highest field region.

iv. Liquid metal ion sources (LMIS)

By applying a strong electrical field and heating the metal source to the liquid state, there is the formation of a thin film of liquid metal ions, which wets completely the surface of the thin needle. Depending on the elements of the alloy, such sources have different melting temperatures which need heating or not, like gallium (29,8°C) or indium (156,6°C) or Be-Si-Au alloys ($\text{Au}_{70}\text{Si}_{15}\text{Be}_{15}$) are employed. In this study, we mainly used dual-beams systems with LMAIS sources such as AuSi and AuGe for nanopatterning at the nanoscale of silicon substrates.

I.1.4.2. Plasma sources

Among familiar states of matter, the plasma state was identified by William Crookes in 1879 [27]. Typically, a plasma is a partially ionized gas composed of free electrons, positive ions, neutral atoms and molecules that are in constant interaction; their composition and concentration are a function of the temperature as stated by Choi [28]. Recently, plasma ion source has found many uses such as in ion implanters, ion projection lithography, and injectors for particle accelerators. Such kind of sources is mainly used for such applications because of its low ion temperature, small energy spreading and good stability. These properties also offer the tantalizing possibility of utilizing such a source to create a noncontaminating focused ion beam (FIB) system for semiconductor fabrication line use and advanced photomask repair applications [29].

Plasmas can be achieved by electric arcs, electrodeless radio frequency (rf) discharge, shock wave, electric arc, micro-wave and laser. The RF driven ion source generates the plasma by passing the ionized gas through a Radio Frequency coil. The RF driven ion sources principle is shown in Figure 1.9.

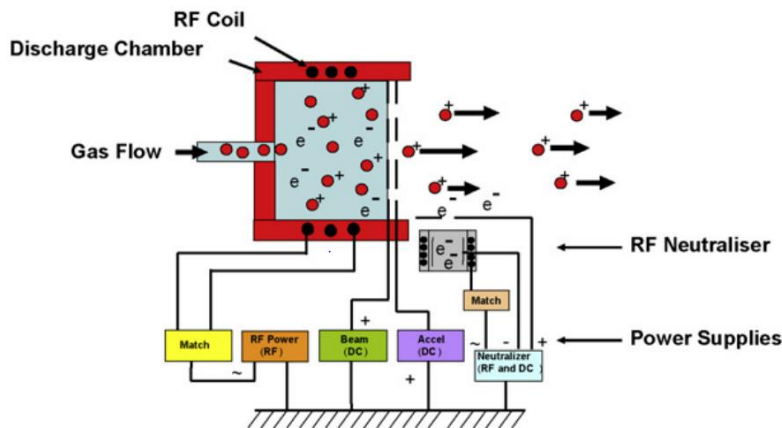


Figure 1.9. RF inductively coupled ion beam source (from Plasma Process Group [12]).

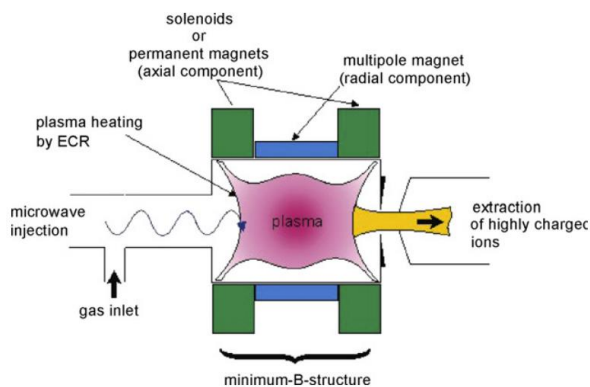


Figure 1.10. Schematic principle of an ECR ion beam source. (from R. Trassl [30]).

Figure 1.10 presents schematically the operation principle of ECR ion sources, so-called hot-plasma ion sources. The Duoplasmatron ion source which was invented by Manfred von Ardenne [31], operates with a cold cathode source but the plasma formed is mechanically and magnetically constricted and accelerated through at least two highly charged grids to form a highspeed ion beam. For the duoplasmatron into a vacuum chamber, when the gas is introduced it has interactions with the free electrons of the cathode, and it is charged and ionized with the formation of plasma (the ionized gas and the electrons). Ions are accelerated through two highly charged grids and form a broad ion beam as shown figure 1.11.

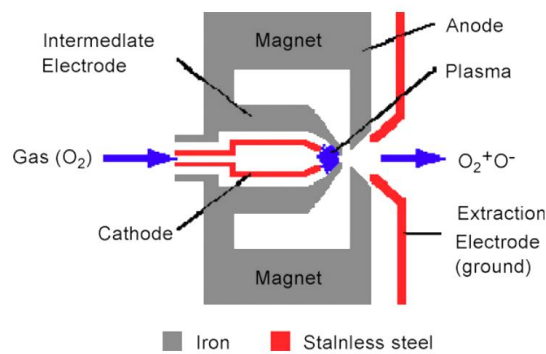


Figure 1.11. Duoplasmatron ion beam source (from [32]).

I.1.4.3. Liquid Metal Ion Source LMIS

The liquid metal ion source is the key element of the focused ion beam system; it consists of a sharpened tungsten needle wetted with a thin film of molten metal (e.g., Ga, Au). Intense ionization of the molten metal takes place at the needle apex when a positive potential of - 3 to 6 kV is applied between the needle and the extraction plate. THIS Ionization occurs when the electrostatic stress pulling on the liquid film exceeds the surface tension stress [33].

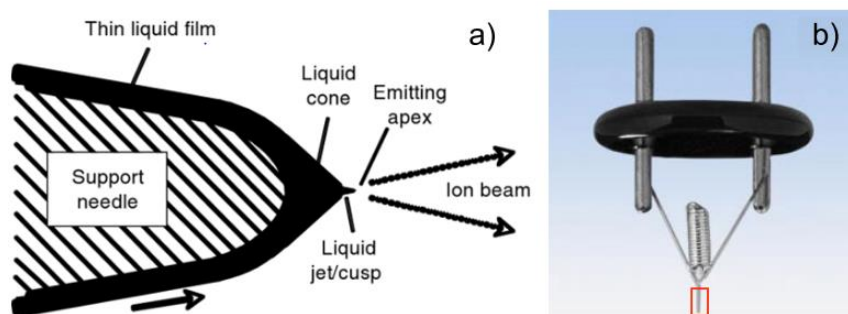


Figure 1.12. a) Schema of a blunt-needle LMIS corresponding to the red rectangle part in b); b) Typical liquid metal ion source substrate showing a W needle and a spiral reservoir spot welded to a heating loop (from FEI Company).

I.1.4.4. Cold Atom Ion source

The cold atomic beam ion source has been developed for surface imaging in scanning ion microscopy [30,31] promising both high brightness and low emittance low energy spread, and a wide choice of ionic species. Based on laser-cooled atomic gases, as the beam of neutral atoms is laser cooled to sub-micro-Kelvin temperature, captured in a magneto-optical trap and photoionized as shown in figure 9. Cold atomic beam ion source is currently one of the subjects of academic researches since the ion beam is focused to a fine spot size (as small as 2 nm for Cs ion beam) [17-34-35] [36].

In a laser-cooled photoionization source, the high brightness is achieved through the extraordinarily cold, microkelvin-range temperatures attainable through laser cooling. These cold temperatures result in a very small angular spread in the ion beam, making possible a high brightness without shrinking the source size to very small dimensions. However, there is a disadvantage when a magneto-optical trap (MOT) is used in the ion source, since a low temperature in the MOT results in a low diffusion rate of the cold atoms, limiting the rate at which the ionization region can be refilled with neutral atoms, as ion current is created. The resulting trade-off between low angular spread and beam current imposes a brightness limit on this type of ion source.

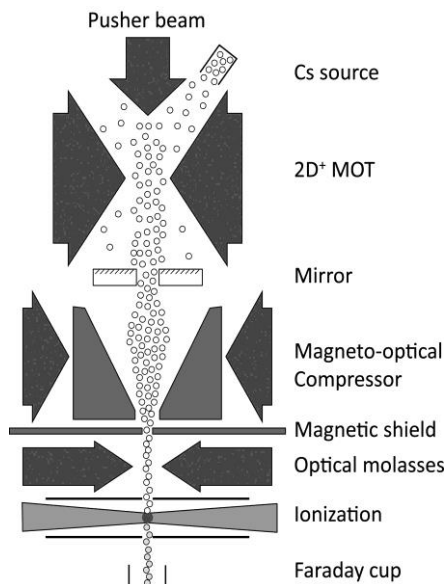


Figure 1.13. Schematic representation of the cold atomic beam ion source, showing the four stages of ion beam production: 2D magneto-optical trap with pusher beam (2D+-MOT), magneto-optical compressor, optical molasses, and ionization [37].

At only a few thousand electron volts or even less, the cold atom ion sources are well suited for operation at low-beam energies that can be used to probe the composition and structure of surfaces with high sensitivity to the topmost layers with minimal sputtering.

High-resolution imaging has been demonstrated with Li, Cs, and Cr ion beams. For example, the brightness measured for a source with Cr ions, was more than 24 times higher than the best one observed with a Ga liquid metal ion source.

I.1.4.5. Helium Ion source

The helium (He) ion source is mostly used for surface imaging and analysis using with He ions which are about 8000 times heavier than electrons with a Broglie wavelength that is approximately 300 times smaller than an electron beam. Thus, a He ion beam exhibits very little diffraction when passed through an aperture or across an edge and it can be focused to a much finer spot size, which enables sub-nanometer resolution with high material contrast and improved depth of focus without the need for sacrificial sputter coating [27–33].

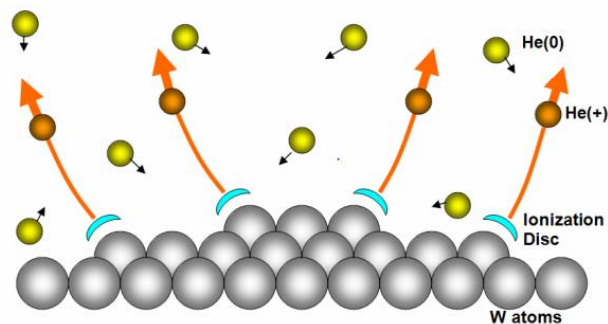


Figure 1.14. Diagram of the He source region where the W atoms (grey) near the topmost ~ 50 Å of the ion emitter and the neutral He ions (yellow) which pass through the ionization disc (blue) are ionized and are then accelerated away (orange arrows) from the tip [33].

He ions sources are appropriate for insulator materials, and reflection ion imaging mode at low angles of incidence can be used to image the surface at high resolution. The high resolution arises from the use of: a finely-sharpened needle and of a process that strips individual atoms away from the source until an atomic pyramid is created with just three atoms at the very end of the source tip.

The He ion sources have resolution of less than 0.3 nm at energy of 25–30 kV, which is the best resolution provided by FIB. The total number of secondary electrons produced is greater than with an electron beam. This larger secondary electron yield and the large difference in yields between different materials, provide higher contrast imaging, making it easier to differentiate the materials. The collected backscattered helium ions enable also the analysis of materials composition using Rutherford backscattering spectrometry. When low acceleration voltages are used for SEM imaging, surface charging remains a problem and consequently a low-energy flood gun charge neutralization system is used to enable high precision metrology.

I.1.4.6. Neon ion source

Besides He (24.5 eV), Ne (21.6 eV) is the only noble gas with an ionization energy significantly higher than that of contaminants such as O (13.7 eV), N (14.5 eV) and CO₂ (13.8 eV). It is why, Ar (15.8 eV), Kr and Xe (11.1 eV) which are less suitable ions for the ionization process are not used so far. Ne gas ion sources have been developed and similarly to He GFIS sources, the Ne ion sources use a trimer-gas-field ion source.

The minimum beam diameter measured is about 1.5 nm at 28 kV, with a sputter yield around 1 atom per incident ion for Si and 4 atoms per incident ion for Cu, while a Ga is by a factor of 2x lower. It is also a factor of 100x higher than the one for the light He ions. According to nanomachining tests performed in a 600 nm SiO₂-CDO dielectric stack and in 30 nm Cr– SiO₂ using 24 kV beam energies (1 pA beam current) the smallest via obtained have a 40 nm lateral size at the mid-point and 30 nm at the basis, with a depth of 240 nm. These results indicate that structures have widths larger than expected and side wall profiles poorer than expected, so that further improvements have to be implemented. The benefit of heavier ion species such as Ne ions, should lie in the field of milling (or of beam-induced deposition and etching).

The comparison of the characteristics of Ga LMIS FIB, ZrO/W Schottky and He GFIS FIB sources is given in table 1.3. The source design is very different providing different sources properties; each type of source is then used for specific applications / kind of samples. GFIS FIB He ions is used for sub-nanometer resolution imaging. The high resolution imaging is related to the small probe radius ~0.12 nm, the high source brightness and the lowest angular intensity and energy spread. As compared, the ZrO/Schottky and the Ga LMIS sources have beam radius of ~ 0.5 nm and 3 nm respectively. However, gas sources have not demonstrated long lifetime, high-brightness operation, except for He sources.

Property	Unit	ZrO/W Schottky (SEM) Value	Ga LMIS (FIB) Value	He GFIS (SIM) Value
Typical extraction voltage	kV	~ 5	~ 5	20
Energy-spread (FWHM)	eV	0.6	5	0.35
Source optical radius	nm	20	25	< 0.08
Typical angular intensity	$\mu\text{A sr}^{-1}$	~ 400	10	2.5
Reduced Angular intensity	$\text{A sr}^{-1} \text{V}^{-1}$	~ 7×10^8	2×10^{-9}	10^{-10}
Source brightness	$\text{A m}^{-2} \text{sr}^{-1}$	~ 5×10^{11}	5×10^9	$> 10^{14}$
Reduced source brightness	$\text{A m}^{-2} \text{sr}^{-1} \text{V}^{-1}$	~ 10^8	10^6	5×10^9
Typical emission current	μA	40 - 400	2	0.5 - 0.8
Typical probe current	pA	variable	variable	variable
Typical probe voltage	keV	variable (0.1 - 30 for ZEISS)	variable (1 - 30 for SII)	variable
Best probe radius	nm	0.5	3	0.12

Table 1.3. Comparison of sources specifications for: ZrO/W Schottky, Ga LMIS FIB and He GFIS sources [12].

I.1.5. Beam Interactions with matter

The interactions between the charged particles with the sample surface, whether electrons or ions, produces the emission of mainly secondary and back scattered particles extracted from the surface, while other particles are slowed down within the solid. The emitted particles can be collected and then amplified to be displayed as a source of information depending on the type of ejected signals, which can be used for imaging, etching and deposition.

As shown previously in table 1.2, the differences between ions and electrons characteristics lie mostly in the intrinsically large difference in the mass and size of particles: ions charged positively or negatively are massive and much larger than electrons. As a consequence, the ion-solid interactions are substantially different from the electron-solid ones. For example, the surface alteration created by ion beams and due to the collision between the primary ions and the surface atoms (which can be determined by the dose, overlap, dwell time and various other ion beam parameters) could not be achieved with electrons. Some details about the different interactions are given below.

I.1.5.1. Electron-solid interactions

When an electron beam is scanning a solid sample, there are different interactions between electrons and the target solid: elastic large-angle scattering, principally with the nucleus of target solid atoms, which includes the backscattering; inelastic scattering, that causes Plasmon excitation, electron-electron binary collisions and ionization.

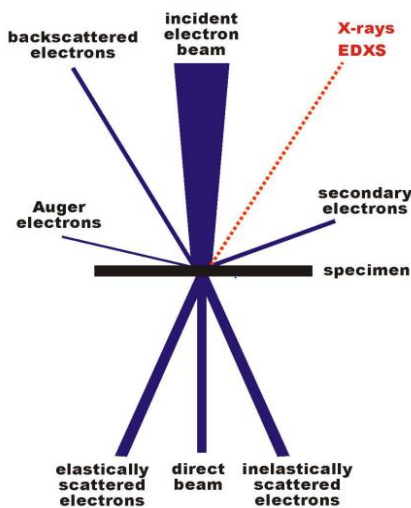


Figure 1.15. Electron-matter interactions arising from the impact of an electron beam onto a specimen. A signal below the specimen can be observable if the thickness of the specimen is small enough to allow the electrons to pass through [38].

These interactions also depend on the nature and the thickness of the samples (inorganic and organic materials, minerals, biological objects). In the case of thin specimen, the electrons may be unabsorbed, transmitted and used to form the image; they are used in transmission electron microscopy (TEM). In the case of thicker specimen, the electrons are not transmitted and only particles (e.g., electrons, x-ray/photons) emerging from the surface can give information; they are the main signals used in a conventional SEM to provide various information on surface topography, crystalline structure, chemical composition and electrical behaviour of the top $\sim 1\mu\text{m}$ depth of specimen. The interactions are classified into two different types, namely elastic and inelastic interactions:

i. Elastic Interactions

there is no energy transferred from the electron to the sample. As a result, the electron leaving the sample still has its original energy E_0 : $E_{el} = E_0$

Such electrons contribute to the direct beam which contains the electrons passing through the sample in the direction parallel of the incident beam. Furthermore, elastic scattering happens if the electron is deflected from its path by Coulomb interaction with the positive potential inside the electron cloud. In this case, the primary electron loses no energy or only a negligible amount of energy. These signals are mainly exploited in TEM and electron diffraction methods.

ii. Inelastic Interactions

If energy is transferred from the incident electrons to the sample, then the electron energy of the electrons after interaction with the sample is consequently reduced: $E_{el} < E_0$

The inelastic interactions can result in different signals such as X-rays, Auger or secondary electrons, plasmons, phonons, UV quanta or cathodoluminescence. Inelastic electron-matter interactions cause signals that are predominantly used by analytical techniques associated to electron microscopy.

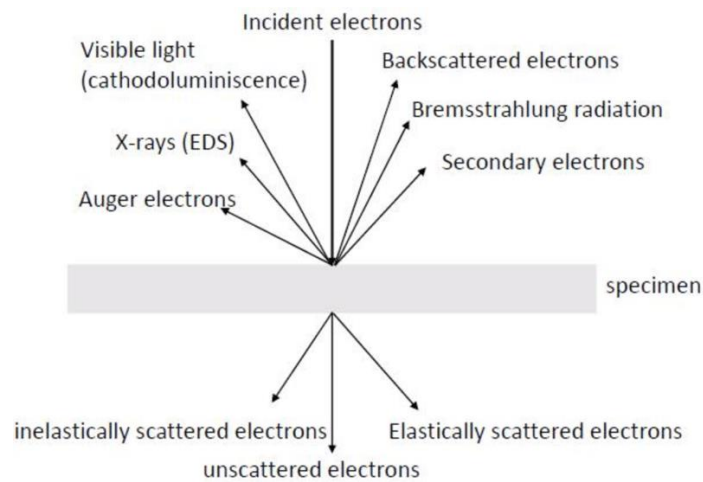


Figure 1.16. Schematic representation of elastic and inelastic electron matter interactions.[39]

Figure 1.17 shows the origin of the different signals that can be detected. In fact, Auger electron and other secondary electrons with rather small energy are readily absorbed in any material. Only the signals generated close to the surface can leave the sample. Back-scattered electrons have the same energy as the incoming beam and thus have larger penetration depths. The absorption of X-rays depends on their energy.

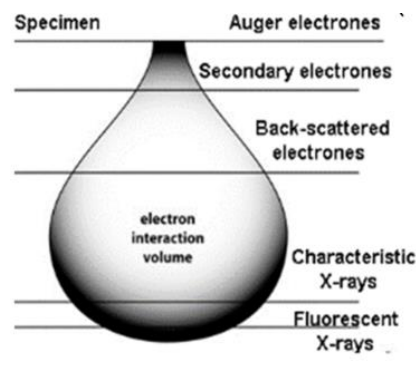


Figure 1.17. Interaction volume at the origin of the signals generated during electron-matter interaction.[40]

I.1.5.2. Ion-solid interactions

During the impingement of energetic ions into the solid, some of the ions lose kinetic energy through inelastic interactions with the specimen and there is an energy transfer from ion beam to solid which leads to different effects according to the energy (milling, sputtering, imaging and deposition).

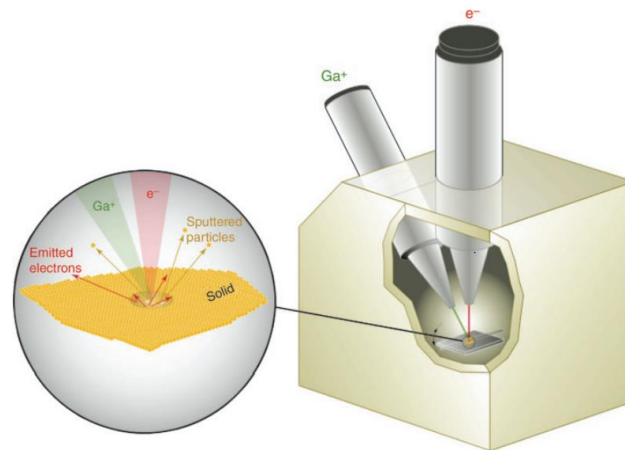


Figure 1.18. Schematic illustration of a dual-beam FIB-SEM instrument with an expanded view showing the electron and ion beam sample interaction.[41]

Basically, the energetic beam hits a solid, collides with constituent atoms and a fraction of these particles is backscattered from the surface layers, while the others are eventually slowed down, implanted within the target at some depth. However, the atoms collisions induce recoil and sputtering of constituent atoms, defect formation, electron excitation and emission, and photon emission. The surface morphology is changed by ion implantation and sputtering; craters, facets, grooves, ridges, and pyramids and/or blistering, exfoliation, and a spongy surface may develop too. Besides, thermal and radiation-induced diffusion contributes to various phenomena of mixing of constituent elements, phase transformation, amorphization, crystallization, track formation and permanent damages.

Moreover, the elastic scattering events (nuclear interactions) result in the displacement of lattice atoms, surface sputtering, and formation of defects, while the inelastic scattering events (electronic losses) cause the production of secondary electrons (SE), X-rays and phonons. All those processes are interrelated in a complicated way and several processes have to be included for the understanding of individual phenomena. The former and the latter work mainly at high and low velocity ranges respectively. The term of stopping power is also used instead of the

energy loss. In the high velocity range, the ions lose their energies by the process of photon generation and by inducing nuclear reactions.

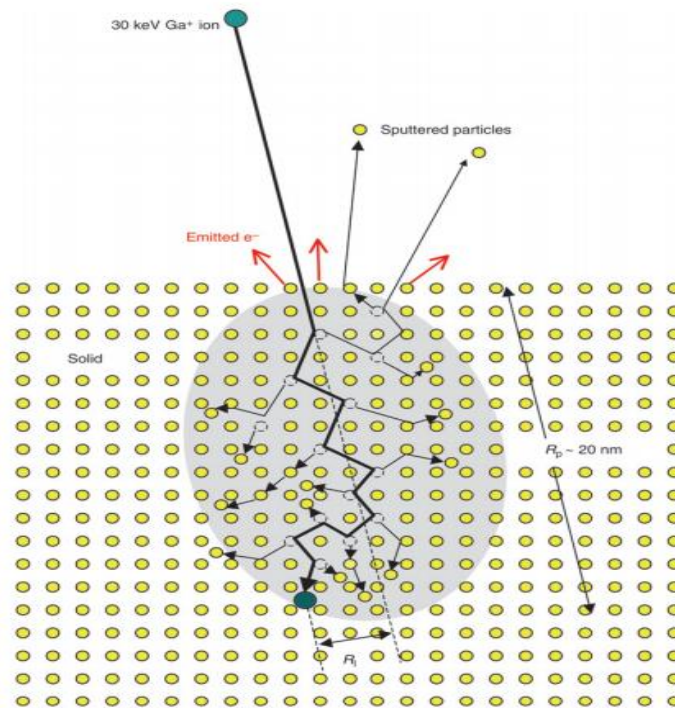


Figure 1.19. Schematic illustration of a collision cascade generated by a 30 keV Ga^+ incident beam on a crystal lattice and of the damages created during the collision cascade volume, and the projected range R_p and lateral range R_l of the implanted ion (from [42])

The secondary particles like neutral atoms, ions and electrons that leave the sample, are collected on a biased detector which is at a positive or negative voltage, for collecting secondary electrons (SE) or secondary ions (SI) respectively (figure 1.20.(a)). The SI that are emitted are also used for secondary ion mass spectroscopy (SIMS) if a mass spectrometer is incorporated in the system. In parallel, a small amount of Ga^+ ions are implanted in the sample during FIB imaging over time while a large number of secondary electrons leave the sample. The substrate can be flooded with electrons from a separate electron source (only when collecting secondary ions for imaging) to prevent positive surface charges from accumulating.

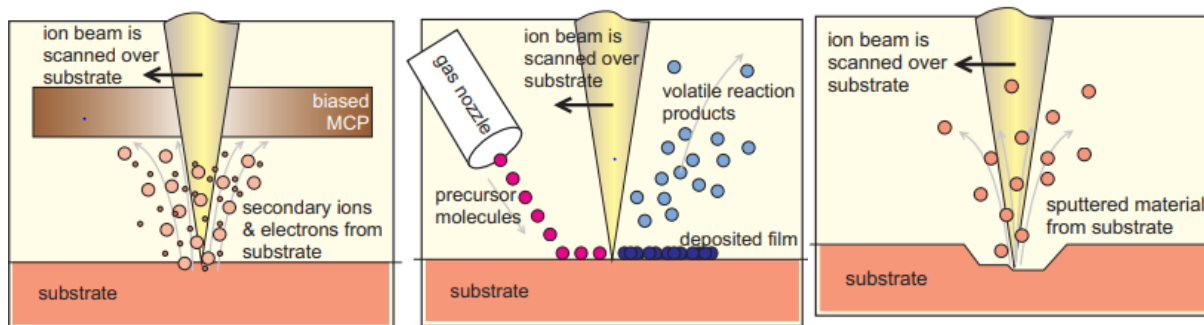


Figure 1.20. Principles of FIB: (a) imaging; (b) deposition process; (c) milling [43].

In metal substrates (i.e., aluminium or copper), which are crystalline materials, the ion penetration depth varies due to channelling along open columns of the lattice structure. Since the secondary electron emission rate depends on the penetration depth, FIB is used to image crystal grains, revealing different crystal orientations.

It is inevitable to have sample damages during FIB imaging, due to the Ga^+ ions that penetrate the sample creating ion implantation. The depth of the implanted region is related to the ion beam energy and to the angle of incidence of the beam. Besides implantation, some milling also always occurs it can be drastically reduced when using a fine ion beam at low ion current.

Localized maskless deposition (with high resolution but low deposition rate) of both metals and insulator materials (e.g., SiO_2) can be provided by FIB. Platinum (Pt) and tungsten (W) are widely used for deposition using organometallic precursor gas (like $\text{W}(\text{CO})_6$ in the case of W) in conventional and commercial FIB station.

During the deposition process (figure 1.20.(b)), a precursor gas is sprayed by a fine nozzle on the surface where it adsorbs, then it is decomposed by the ion beam. The volatile reaction products desorb from the surface and are removed through the vacuum system, while the desired reaction products (Pt, W or SiO_2) remain deposited on the surface as a thin film. It is known that the deposited material is not pure because of organic contaminants (mainly Carbon) that deposit as well as Ga^+ ions (from the ion beam).

Applying a high ion current beam, the material sample is removed easily as illustrated in figure 1.20.(c). Through calculating the yield sputtering of the material, it is possible to pattern and cut various shapes in any specimen. The gas-assisted etching (GAE) technique that uses an etching gas can be applied in parallel to speed up the process or to increase the selectivity towards different materials.

Understanding the sputtering which occurs from a series of elastic collisions where momentum is transferred from the incident ions to the target atoms within a collision cascade region needs to consider the interaction between an ion beam and the target. When a surface atom receives ions with sufficient high kinetic energy to overcome the surface binding energy (SBE) of the target material, it is ejected as a sputtered particle. The ejected atoms may be ionized and collected either to form an image or to analyse their mass using a SIMS (FIB supplementing SIMS). Although, milling takes place as a result of physical sputtering of the target, the inelastic scattering events (production of phonons, plasmons (in metals), and secondary electrons) are also the result of ion bombardment.

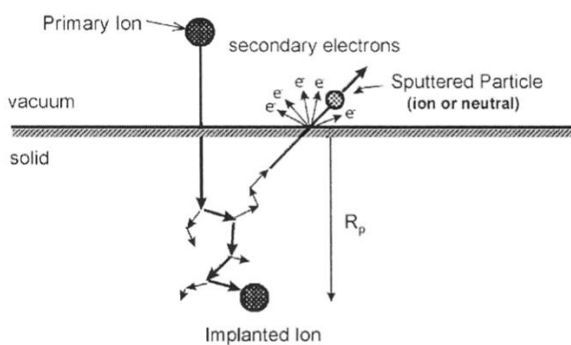


Figure 1.21. Ion beam / matter interactions from ion bombardment of a solid [44].

The degree of ion implantation depends on ion energy, angle of incidence, ion species, and target material. FIB uses the process of ion bombardment to selectively remove material and atoms that are displaced from their equilibrium positions by the impingement of energetic ions that generate a collision cascade within the target material. Sputtering occurs if sufficient momentum is transferred to a surface atom, it is associated to two major processes:

i. Amorphization

One consequence of ion implantation can be the development of a surface amorphous phase which is typically metastable; its formation results from the collision cascade and depends on unit cell size, chemical ordering, and width of an intermetallic phase field [100]. The restoration of the induced disorder requires correlated and cooperative motion of alloying atoms. The more complex the material unit cell, the thicker the amorphous zone is. Likewise, smaller unit-celled materials are difficult to amorphized. Additionally, alloys or materials with a broad phase field will remain crystalline, since the atomic packing arrangement is less stringent than line compounds or stoichiometric inter-metallics.

ii. Local Heating

During ion implantation, almost all the ion kinetic energy is eventually converted to heat, with only a small fraction stored as defects in the sample or emitted as energetic particles or radiated. For time longer than nanoseconds and distances larger than ~100 nm, the ion beam can be approximated as a continuous heat source. At shorter times, there are large temporal variations in heating, and at times shorter than 10–12 s, the atoms barely have time to interact with each other, and the temperature of the solid is not well defined. The maximum temperature reached in a sample depends on the beam power (P), sample thermal conductivity (k), sample geometry, and contact to a heat reservoir. Beam powers in commercial systems have maximum values of 1 mW.

When an incident ion beam impacts a flat surface, the transfer of heat is so effective in absence of a heat reservoir, that the sample is heated even away from the incidence point. Heating can be diminished by placing the samples in contact with a heat reservoir. During imaging or TEM lamellae preparation, much higher temperatures may be reached when the sample geometry limits the transfer of heat.

I.2. FIB applications

Combined to high resolution imaging and deposition (suitable gas delivery system), the dual beam FIB/SEM is the best tool for nano-structuring. It combines precise material removal and deposition capabilities with high-resolution navigation, alignment, and real time process control. Various physical effects can be used such as substrate milling enabled by the sputtering of neutral and ionized substrate atoms, imaging which is enabled by electron emission that may cause charging of the sample, damage induced by displacement of atoms in the solid, heating by the emission of phonons and deposition due to chemical interactions including the breaking of chemical bonds, thereby dissociating molecules. These effects are applied in failure analysis, defect characterization, design modification, and process control in a variety of industries

I.2.1. 3D imaging and tomography

3D tomography techniques are becoming crucial for semiconductor devices fabrication and in medical technology. Their features are given Figure 1.22. The technique with the lowest resolution is Magnetic resonance imaging (MRI) which has a resolution of a few hundreds of μms .

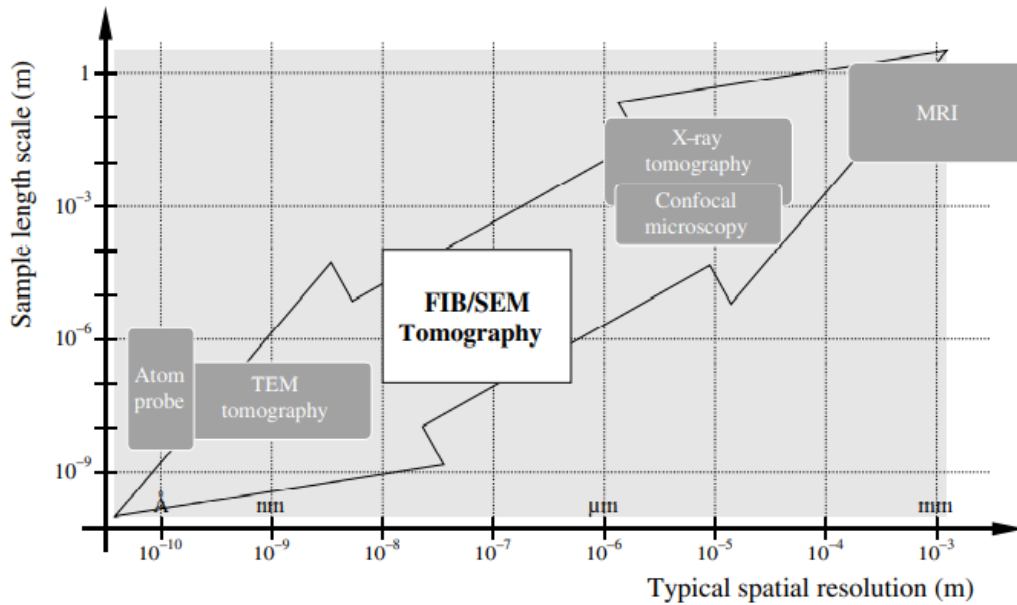


Figure 1.22. Examples of spatial resolution and sample scale for 3D characterization techniques [26].

Confocal microscopy provides 3D model reconstituted from an optical through-focus series of images of the same sample with a bas lateral resolution ($\sim 0.2\mu\text{m}$) because of its light optical nature. Sample sizes are $\sim 1\text{ mm}$, the same size used during X-ray tomography, which is also a non-destructive technique that provides 3D tomography. The best synchrotron X-ray sources provide spatial resolution $\sim 10\mu\text{m}$ for complete 3D representation using series of 2D images recorded during the attenuation of X-rays travel through the length of the sample.

TEM tomography is the best powerful technique for small volumes of material analysis having a few mm^2 in surface area and no more than 100-300 nm thick. It provides 3D analyses of series of images from various angles of tilt. Atom probe or field-ion microscopy (FIM) techniques that use a very thin and sharp needle-like specimen have the best resolution. The ions are field emitted from the sample by a strong electrical field applied to the specimen tip. It is dedicated to conductive and small samples and requires extensive preparation, for generating the 3D elemental information from combined time-of-flight (TOF) mass-spectrometry and a position-sensitive detector.

Between all these techniques, FIB fills an obvious gap and it is increasingly used for small samples or for the analysis of small volumes of materials. The samples size can reach 100 mm and preparation slides are about $10\mu\text{m}$ long. 3D structures provided by sequential sectioning in the FIB with variable slopes and nm tolerances. Ion/surface interactions effects may affect the surface roughness during the 3D characterization process.

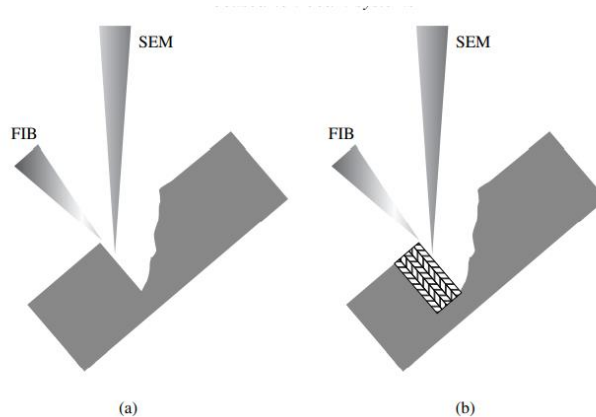


Figure 1.23. Schematic representation of (a) preparation of a cross section in a Dual-Beam and (b) multiple, serial cross sections where the dashed boxes represent thin layers of material that are polished off sequentially after SEM imaging.[47]

In Dual Beam FIB/SEM 3D imaging is the result of the combination of images generated with the typical times for SEM (secondary electron or backscattered electron images) and FIB images (using secondary electron or secondary ion images), including EDS and EBSD maps are given in table 1.4.

Instrument type	Type of “image” (data) acquired	Sample position manipulation?	Typical cycle time
DualBeam	SEM (SE, BSE)	No	1–5 minutes
	FIB (SE, SI)	Yes	2–10 minutes
	EDS	No	2–15 minutes
	EBSD	Yes	5–30 minutes
FIB only	SEM (SE, BSE)	n/a	n/a
	FIB (SE, SI)	Yes	2–10 minutes
	EDS	Yes	Currently not known
	EBSD	n/a	n/a

Table 1.4. Possibilities and limitations of Dual Beam and FIB only systems (n/a in the FIB section means that this combination is not applicable since it requires a primary electron beam) [47].

Three-dimensional analysis using FIB tomography is essentially a two-step process as shown in figure 1.24.

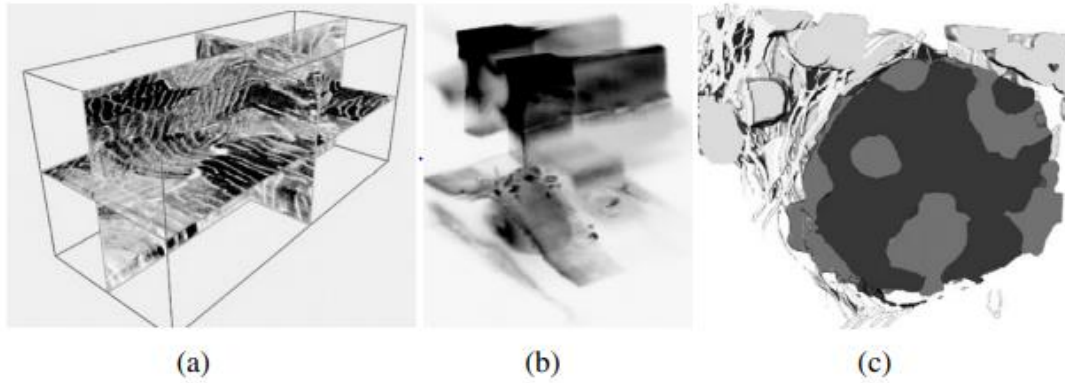


Figure 1.24. Examples of FIB tomography based on 3D characterization using different visualization techniques. (a) Orthogonal sections through a steel sample; (b) volume observation based on voxel transparency of a semiconductor defect; (c) surface observation after segmentation of a biological cell sample. The length scale of the images is $1\mu\text{m}$. [48]

I.2.2. TEM lamella preparation

The most important FIB application in micromachining, is the preparation of thin cross-section samples necessary for TEM observations. During preparation, FIB is used for both imaging the sample and removing material from both sides of the sample. The polishing is done till getting the transparency of lamella for electrons. Lamellae preparation can be achieved using two ways, even pre-thinning [49, 50, 51] or lift out [52]. The difference is that pre-thinning technique is made up on cutting sample parts of samples for thinning range around $10\text{--}50\ \mu\text{m}$, followed by FIB thinning using low beam currents. The main advantage is a very accurate positioning of the TEM slice; the sample can even be returned to the FIB for further thinning if needed [53]. However, the lift-out technic is totally based on the FIB thinning with undercuts of the milled target using low beam currents too. Lamella prepared with FIB has around $10\text{--}20\ \mu\text{m}$ length size and less than $100\ \text{nm}$ thickness. The main drawbacks of this approach are the damages artifacts induced by FIB during the preparation i.e., gallium ions implantation that amorphized the surface of the crystalline specimen, the mixing of components and loss of fine structural details by sputtering effects [54,55,56,57]. For that reason, care should be taken to protect the sample surface by platinum layer deposition using GIS, incorporated in FIB/SEM dual beam station, before starting the thinning steps, electron and ion platinum deposition are efficient to avoid sample damages and keep the top surface. However, FIB specimen preparation has an interesting advantage which is the ability to map out compositional dopant variations at the 10

ppm level [58,59,60], in the case of InP-based and similar materials (e.g., InGaAs, InGaAsP) that were prepared only by the FIB preparation techniques. It was demonstrated that the absorption contrast observed upon clustering of P point defects in differently doped layers is in fact associated with isoelectronic Ga1 centers introduced by the FIB.

FIB and TEM are also used in biological fields for visualising biological samples for instance the details of cells, tissues and small organisms, contrary to SEM which doesn't provide this kind of observation. However, the preparation can cause the destruction of tissues and cells and modify their appearance. It is then actually a challenge for scientists to develop new approaches to preserve their biologic samples like they are in the living organism and to do the observation at their natural state as much as possible.

I.2.3. Nanopatterning

Direct pattern writing of a substrate with FIB is one among the others FIB applications. For such application, the stage motion and the beam deflection need to be integrated. This can be done by computer control, in the same way as with e-beam lithography systems. If one needs to align to existing features, the scanning ion microscope capability is used. Typically, crosses with well-defined edges are fabricated as alignment marks [61]. These crosses can be located on the screen visually, or a precise location can be determined by scanning the beam over the arms of the cross under computer control and detecting the electrons emitted. The secondary electron emission for various geometry sidewalls has been studied [62]. The interferometer reads the stage position to an accuracy of $\pm 0.01 \mu\text{m}$. The error signal between the desired position and the achieved position (usually less than 2 nm) can be added to the deflection signal automatically.

The use of FIB for lithography with resist exposure is the direct analogue of electron beam lithography. The beam is scanned in a computer-generated pattern which defines the shapes in the resist (a material sensitive to ions), which is later processed to form structures such as optical gratings, masks and archived data. This process can be used, for example, to pattern a mask that will serve for the patterning by optical lithography of a semiconductor wafer or for the "direct writing" lithographic step. Research in lithography using FIB was stimulated by the fact that many resists exhibit a greater sensitivity to ions than to electrons, sometimes by orders of magnitude, so that exposure rates could be decreased improving throughput. In addition, there

is no "proximity effect" with ions while it occurs with electrons due to back scattered electrons; such effect limits the minimum feature sizes obtainable with e-beam writing.

I.2.4. Ion implantation and Defects

The predominant use of FIB was the direct maskless implantation for the doping of semiconductors. In this case, the implanted atoms have different valences than the semiconductor matrix to create the charge carriers. After implantation, since the spatial distribution of dopants is maximum at a specific depth below the surface, a high temperature annealing should be performed in order to activate these implanted elements (activation occurs when the implanted atoms occupy the crystalline lattice sites). The annealing is also used to improve the depth homogeneity of doping and to restore the crystallinity of the substrate. Indeed, the implantation is associated to the formation of defects and to amorphization created in a speed time due to substrate sputtering effect. Experimental parameters for the implantation process depend on the matrix and the implanted atoms. Contrary to conventional lithography which uses masks that cover and protect areas not to be implanted while the target areas are exposed to ion bombardment, the FIB permits a direct patterning lithography and implantation to desired areas which facilitates the preparation of samples and saves processing time.

Doping with different gradient profiles and/or modifying the pattern shape with homogeneous doses differing from one device to another requires to vary the ion beam parameters such as dwell time in adjacent pixels and the number of scans. Various devices are concerned: bipolar transistors, GaAs MESFETs and tuneable Gunn diodes, etc. Many lithographic steps can be removed to make experimentation and production much easier and less costly in both time and money. In MOS transistors and GaAs MESFETs, channel implantation doses are low and cover limited areas; typically, in the implanted areas, the doses are in the E^{11} to E^{13} ions/cm² range. Ga⁺ ions implantation with subsequent wet etching with FIB have been reported by Brugger et al [10] and Schmid et al [26]. It was used for the fabrication of micro- and nanomechanical elements in silicon with an optimum concentration of p⁺ doping in Si since it drastically reduces the etch rate of certain etchants such as potassium hydroxide (KOH) in the implanted region [49]. The critical dose reported by J. Micromech et al.,[60] is a dose of E^{15} ions cm⁻² which is optimal for an effective etch stop; these doses are obtained with the use of typically 100 pA beam currents. For higher doses (above E^{16} ions cm⁻²), amorphization and sputtering effects must be taken in account. Implantation is also used for Cantilevers fabrication with a length and

a width of 0.5 to 10 μm and 0.1 to 1 μm respectively. The thickness of implantation is limited to 30 nm due to the ion energy as presented schematically in figure 1.25.

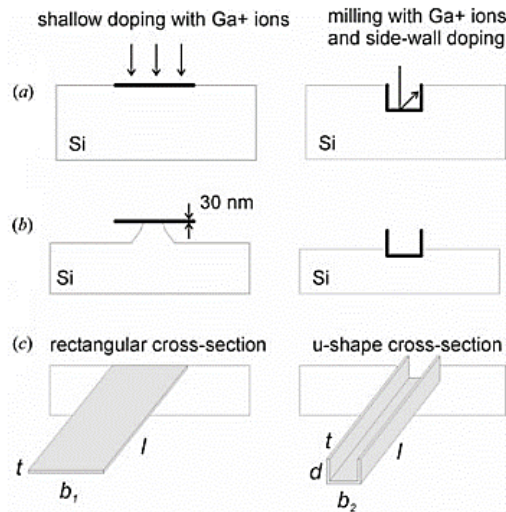


Figure 1.25. Schematic representation of cantilevers fabrication by shallow doping (left-hand side) and milling + sidewall doping (right-hand side): (a) FIB exposure (milling and/or implantation), (b) during KOH etching and (c) after etching is completed [62].

For micromachining applications FIB milling is not limited. It is used also for tunnelling gap milling [63], channel and cantilever milling [64], trimming of magneto-resistive heads [65], TEM membrane preparation [66, 67, 68] and micromachining of Si nanomechanical elements. A nice example is the fabrication of nano-cups in silicon, with 200 nm diameter and a few μm depth is reported on figure 1.26. They are obtained by FIB modification of the Silicon, followed by subsequent etching. The nano-cups produced can have ultrasmall volumes of about 3×10^{-8} nl. In this case, the FIB damages generated in the sample are valued as a benefit.

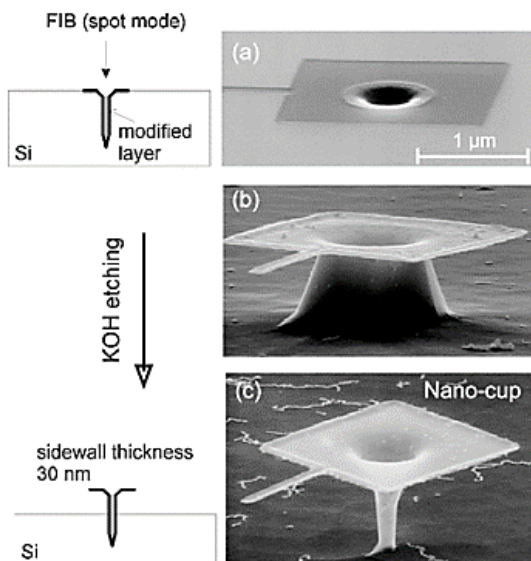


Figure 1.26. Fabrication of a nanocup: (a) after FIB milling a hole, followed by KOH etching during: (b) 10min and (c) 15 min. [69]

Conclusion

For a variety of microfabrication and nanofabrication applications, FIB systems have been developed thanks to the development of LMIS sources (typically Ga source). With the introduction of LMAIS, a larger number of applications were accessible and various processes were combined for semiconductor devices manipulation. The nature of the source was chosen as a function of the nature of the samples, the desired application and the following steps of the process. The experimental parameters for the nano-structuration were optimised according to the beam-solid interactions to improve the nanofabrication process. FIB columns provide more capabilities when combined with other techniques: FEB column, SIMS, AFM, Wien filter and GIS incorporated in one station.

In this chapter, I have given an overall short review of the conventional FIB instruments, their components, the experimental parameters, the ion/matter interactions and some common applications.

References

- [1] P.D. Prewett, G.L.R. Mair, Focused Ion Beam from Liquid Metal Ion Sources, Taunton Somerset (UK); Research Studies Press, 1991.
- [2] Y.G. Kim, Y.S. Kim, E.H. Choi, S.O. Kang, G. Cho, H.S. Uhm, J. Phys. D: Appl. Phys. 31 (1998) 3463.
- [3] L.W. Swanson, Nucl. Instr. and Meth. 218 (1983) 347.
- [4] C.A. Crox, Statistical Mechanics of the Liquid Surface, Wiley, Chichester, USA, 1980, p. 161.
- [5] P.D. Prewett, D.J. McMillan, D.K. Jeeries, G.L.R. Mair, Proc. SPIE 393 (1983) 120.
- [6] W. Knauer, Optik 59 (1981) 335.
- [7] L. Bischof, J. Teichert, E. Hesse, D. Panknin, W. Skorupa, J. Vac. Sci. Technol. B 12 (1994) 3523.
- [8] G.L.R. Mair, J. Phys. D: Appl. Phys. 25 (1992) 1284.
- [9] Ansari, K. et al., 2004. Fabrication of high aspect ratio 100 nm metallic stamps for nanoimprint lithography using proton beam writing.
- [10] P. Marriott, Appl. Phys. A 44 (1987) 329. [10] T. Ishitani, K. Umemura, Y. Kawanami, J. Appl. Phys. 61 (2) (1987) 748
- [11] Bell, D.C. et al., 2009. Precision cutting and patterning of graphene with helium ions. Nanotechnology, 20(45), p.455301.
- [12] Arshak, K. et al., 2004. A novel focused-ion-beam lithography process for sub-100 nanometer technology nodes. Superlattices and Microstructures, 36(1-3), pp.335-343.
- [13] Chekurov, N. et al., 2009. The fabrication of silicon nanostructures by local gallium implantation and cryogenic deep reactive ion etching. Nanotechnology, 20(6).
- [14] G. Zhang, Y. Cheng, J.-P. Chou, and A. Gali, Material platforms for defect qubits and single-photon emitters, Applied Physics Reviews 7, 031308 (2020).
- [15] Yasaka, A. et al., 2008. Application of vector scanning in focused ion beam photomask repair system. Journal of Vacuum Science and Technology B: Microelectronics and Nanometer Structures, 26(6), pp.2127-2130.
- [16] Notte, J., 4th et al., 2010. Diffraction imaging in a He⁺ ion beam scanning transmission microscope. Microscopy and Microanalysis: The Official Journal of Microscopy Society of America, Microbeam Analysis Society, Microscopical Society of Canada, 16(5), pp.599- 603.
- [17] D.S. Swatik and C.D. Hendricks, AIAA 6 (1968) 1596. [8] R.L. Seliger, J.W. Ward, V. Wang, and R.L. Kubena, Appl. Phys. Lett. 34 (1979) 310.
- [18] V.N. Tondare, J. Vac. Sci. Technol. A 23(6) (2005) 1498.
- [19] Erwin W. Müller and Tien T
- [20] Namatsu, H. et al., 1998. Nano-patterning of a hydrogen silsesquioxane resist with reduced linewidth fluctuations. Microelectronic Engineering, 41-42, pp.331-334.

- [21] Ziegler, J.F., 2004. SRIM-2003. Nuclear Instruments and Methods in Physics Research, Section B: Beam Interactions with Materials and Atoms, 219-220(1-4), pp.1027-1036.
- [22] Orloff, J., Swanson, L.W. & Utlaut, M., 1996. Fundamental limits to imaging resolution for focused ion beams. Journal of Vacuum Science & Technology B: Microelectronics and Nanometer Structures, 14(6), p.3759.
- [23] Rau, N., 1998. Shot-noise and edge roughness effects in resists patterned at 10 nm exposure. Journal of Vacuum Science & Technology B: Microelectronics and Nanometer Structures, 16(6), p.3784.
- [24] Persson, A., Thornell, G. & Nguyen, H., 2010. Rapid prototyping of magnetic tunnel junctions with focused ion beam processes. Journal of Micromechanics and Microengineering, 20(5).
- [25] Taniguchi, J. et al., 2006. Rapid and three-dimensional nanoimprint template fabrication technology using.
- [26] Nan Yao. FOCUSED ION BEAM SYSTEMS Basics and Applications, Princeton University, New Jersey. First published 2007.
- [27] Perspectives on Plasmas (1994) General Atomics, <http://www.plasmas.org/what-are-plasmas.htm>.
- [28] Choi HK (1988) Thermal Plasmas in Chemical Processings. Chemical Industry and Technology 6(2):176–188.
- [29] Plasma Science and Technology for the 21st Century, <http://www.plasmas.org/rot-manufacturing.htm>
- [30] Trassl R (2002) Development of ECR Ion Sources, Institut für Atom- und Molekülphysik, Universität Giessen, Germany, accessed at <http://www.strz.uni-giessen.de/eZR/english/prinzip.html>.
- [31] von Ardenne M (1956) Tabellen der Elektronenphysik, Ionenphysik und Ultramikroskopie (VEB- Deutscher Verlag der Wissenschaften, Berlin).
- [32] Beck PA, Roos BFP, Demokritov SO, Hillebrands B (2005) Ion Beam Smoothing with Low-energy Argon Ions and Reduction of Ne⁺ el “Orange Peel” Coupling in Magnetic Tunnel Junctions. Journal of Magnetism and Magnetic Materials 290– 291:1108–1111.
- [33] An Introduction to Helium Ion Microscopy J. Notte*, R. Hill, S. McVey, L. Farkas, R. Percival, B. Ward *ALIS Corporation, 10 Technology Drive, Peabody, MA 01960, jnotte@ALIScorporation.com.
- [34] Biersack JP, Ziegler JF (1985) The Stopping and Ranges of Ions in Matter, vol. 1. Pergamon Press, Oxford.
- [35] Schmidt, B., Bischoff, L. & Teichert, J., 1997. Writing FIB implantation and subsequent anisotropic wet chemical etching for fabrication of 3D structures in silicon. Sensors and Actuators A: Physical, 61(1-3), pp.369-373.
- [36] Bradley RM, Harper JME (1988) Theory of Ripple Topography Induced by Ion Bombardment. Journal of Vacuum Science and Technology A 6(4):2390– 2395.
- [37] M. Nastasi, J. Mayer, and J. K. Hirvonen. Ion-Solid Interactions: Fundamentals and Applications. Cambridge University Press, USA, 1996.

- [38] Orloff, J., Swanson, L. & Utlaut, Mark, 2002. High Resolution Focused Ion Beams: FIB and Applications 1st ed., Springer.
- [39] S. Reyntjens and R. Puers. A review of focused ion beam applications in microsystem technology. *J. Micromech. Microeng.*, 11:287–301, 2001.
- [40] C.A.Volkert and A.M. Minor, Guest Editors; Focused Ion Beam Microscopy and Micromachining.
- [41] P. Sigmond, *Phys. Rev.* 184, 383 (1969).
- [42] P. Sigmond, *J. Mater. Sci.*, 8, 1545 (1973).
- [43] Townsend P. D., Hartley N. E. W., and Kelly J. C. Ion implantation, sputtering and their applications. Academic Press, New York, NY, 1976.
- [44] J. F. Ziegler and J. P. Biersack. The Stopping and Range of Ions in Matter. Springer US, USA, 1985.
- [45] Adams DP, Mayer TM, Vasile MJ, Archuleta K (2006) Effects of Evolving Surface Morphology on Yield During Focused Ion Beam Milling of Carbon. *Applied Surface Science* 252. pp. 2432–2344.
- [46] Reyntjens, S. & Puers, R., 2001. A review of focused ion beam applications in microsystem technology. *Journal of Micromechanics and Microengineering*, 11(4), pp.287-300.
- [47] Boulos MI (1985) The Inductively Coupled R.F. (radio frequency) Plasma. *Pure and Applied Chemistry* 57(9):1321–1352.
- [48] Sidorkin, V. et al., 2009. Sub-10-nm nanolithography with a scanning helium beam. *Journal of Vacuum Science & Technology B: Microelectronics and Nanometer Structures*, 27(4), p.L18.
- [49] M.W.Phaneuf.et.al, *Micron* 30(3), 277–88 (1999).
- [50] J. Melngailis, *J. Vac. Sci. Techn. B* 5(2), 469-495 (1987).
- [51] L. A. Giannuzzi, F. A. Stevie, *Micron* 30, 197–204 (1999).
- [52] S. Shankar Y. W. Riddle, M. M. Makhlof, *Metallurgical & Materials Trans A* 34, 705-707 (2003).
- [53] M. Jublot, M. Texie, *Micron* 56, 63-67 (2014).
- [54] Jian Li, T. Malis, S. Dionne, *Materials Characteri* 57, 64–70 (2006).
- [52] Platzgummer, Elmar & Loeschner, Hans, 2009. Charged particle nanopatterning. *Journal of Vacuum Science & Technology B: Microelectronics and Nanometer Structures*, 27(6), p.2707.
- [50] Albarede, P.H., Lezec, H.J., 1998. Transmission electron microscopy of focused ion beam induced damage at 50 keV in Si. In: Calderon Benavides, H.A., Yacaman, M.J. (Eds.). *Electron Microscopy 1998, ICEM14, Symposium HHInstitute of Physics, Bristol*, pp. 431.
- [51] Bender, H., Vanhellemont, J., Schmolke, R., 1997. High resolution structure imaging of octahedral void defects in as-grown Czochralski silicon. *Japanese Journal of Applied Physics, Part 2: Letters* 36, L1217–L1220.

- [52] Prenitzer, B.I., Giannuzzi, L.A., Brown, S.R., Irwin, R.B., Shofner, T.L., Stevie, F.A., 1998. The influence of incident ion range on the efficiency of TEM and SEM specimen preparation of focused ion beam milling. In: Calderon Benavides, H.A., Yacaman, M.J. (Eds.). *Electron Microscopy 1998, ICEM14, Symposium K*Institute of Physics, Bristol, pp. 711.
- [50] Prenitzer, B.I., Giannuzzi, L.A., Brown, S.R., Irwin, R.B., Shofner, T.L., Stevie, F.A., 1998. *Microscopy and Microanalysis 1998 Proceedings*, Microscopy Society of America p. 858.
- [51] Sheng, T.T., Goh, G.P., Tung, C.H., Wang, J.L.F., Cheng, J.K., 1997. FIB precision TEM sample preparation using carbon replica. *Proceedings of the International Symposium on the Physical and Failure Analysis of Integrated Circuits, IPFA 1997 IEEE*, Piscataway, NJ
- [52] Tarutani, M., Takai, Y., Shimizu, R., Uda, K., Takahashi, H., 1993. Development of a focused ion beam apparatus for preparing cross-sectional transmission electron microscope specimens. *Technology Reports of the Osaka University*, Vol. 43, no. 2142–2162. pp. 167–173.
- [53] Overwijk, M.H.F., van den Heuvel, F.C., Bulle-Lieuwma, C.W.T., 1993. Novel scheme for the preparation of transmission electron microscopy specimens with a focused ion beam. *Journal of Vacuum Science and Technology* 11 (6), 202.
- [54] Tsujimoto, K., Tsuji, S., Takatsuji, H., Kuroda, K., Saka, H., Miura, N., 1997. Cross-sectional TEM sample preparation method using FIB etching for thin-film transistor. In: Anderson, R.M., Walck, S.D. (Eds.). *Materials Research Society Symposium Proceedings*Materials Research society, Pittsburgh, pp. 207.
- [55] Giannuzzi, L.A., Drown, J.L., Brown, S.R., Irwin, R.B., Stevie, F.A., 1997. Focused ion beam milling for site specific scanning and transmission electron microscopy of materials. *Microscopy and Microanalysis* 3 (Suppl. 2), 347.
- [56] V.E. Krohn and G.R. Ringo, *Appl. Phys. Lett.* 27 (1975) 479 .
- [57] A review of focused ion beam milling techniques for TEM specimen preparation L.A. Giannuzzi*, F.A. Stevie a University of Central Florida, Advanced Materials Processing and Analysis Center, Mechanical Materials and Aerospace Engineering, Orlando, FL 43816- 2450, USA.
- [58] Anderson, R., Klepeis, S.J., 1997. Combined tripod polishing and FIB method for preparing semiconductor plan view specimens. In: Anderson, R.M., Walck, S.D. (Eds.). *Materials Research Society Symposium Proceedings*, 480. Materials Research Society, Pittsburgh, PA, pp. 187.
- [59] Susnitzky, D.W., Johnson, K.D., 1998. Focused ion beam (FIB) milling damage formed during TEM sample preparation of silicon. *Microscopy Microanalysis*, Vol. 4(Suppl 2), Microscopy Society of America, p. 656.
- [60] Stevie, F.A., Downey, S.W., Brown, S., Shofner, T., Decker, M., Dingle, T., Christman, L., 1998. Microscale elemental imaging of semiconductor materials using focused ion beam SIMS. *Microscopy Microanalysis*, Vol. 4 (Suppl 2), Microscopy Society of America, p. s650.
- [61] Y. Lec and R. L. Kubena, *Appl. Phys. Lett.* 48,668 (1986).
- [62] R. L. Kubena, C. L. Anderson, R. L. Seliger, R. A. Jullcns, and E. H. Stevens, *I. Vac. Sci. Technol.* 19, 916 (1981).

- [63] R. H. Reuss, D. Morgan, and A. Goldenetz, *J. Vac. Sci. Technol.* B4, 290 (1986). 97S. D. Chu, J. C. Corelli, and A. J. Steckl, *J. Vac. Sci. Technol.* B 4, 375 (1986).
- [64] E. Miyauchi and H. Hashimoto, *Nucl. Instrum. Methods Phys. Res. B* 7/ 8, 851 (1985).
- [65] R. H. Reuss, D. M. Morgan, E. W. Greeneich, W. M. Clark, and D. B. Rensch, *J. Vac. Sci. Technol.* B 3, 62 (1985). 93M. Tamura, S. Shukuri, S. Tachi, T. Ishitani, and H. Tamura, *Jpn. J. Appl. Phys.* 22, L698 (1983).
- [66] Bernardi D, Colombo V, Ghedini E, Mentrelli A (2005) Three-Dimensional Modeling of Inductively Coupled Plasma Torches. *Pure Applied Chemistry* 77(2):359–372.
- [67] K. Nakamura, T. Nozaki, T. Shiokawa, K. Toyoda, and S. Namba, *Jpn. J. Appl. Phys.* 24, L903 (1985)
- [68] R. Clampitt, K.L Aitken and D.K. Jeffries, *J. Vac. Sci. Technol.* 12 (1975) 1208.
- [69] R. L. Kubena, J. Y. M. Lee, R. A. Jullens, R. G. Brault, P. L. Middleton, and E. H. Stevens, *IEEE Trans. Electron Devices* 31, 1186 (1984).

II. Filtered Focused Ion Beam Column technology

Introduction

Three basic types of microscopes: optical, scanning probe and charged particle (electrons or ions). In the world of microscopes, the optical microscope is the easiest to deal with, using visible light with transparent lenses to magnify while observing samples or objects as small as one micro-meter. However, instead of light, charged particles form a focused ion or electron beam used in the electron and the ion microscope, which require to be focused in tiny spot with electrostatic or electromagnetic lenses to raster scanning the surfaces as small as 0.1 nano-meter. Furthermore, the scanning probe microscope uses a very small tip needle which scan the surface in direct contact or near-contact to form images. In this research, various microscopies were deployed as SEM, FIB, AFM, TEM and optical microscope in order to characterize the samples surfaces and observe the patterns created with FIB lithography and the de-wetted objects in RTO process.

Today, FIB technology is the gold technique used in semiconductor manufacturing and many research laboratories for nanoparticle elaboration, TEM lamellae preparation and IC characterization and other micro and nanodevices analysis. FIB is a popular instrument due to its high potential in various applications lead many companies to contribute to the development of its components in order to improve its performance for research and semiconductor industry such as: FEI, JEOL, Orsay Physics, Hitachi, Seico, Carl Zeiss, Raith, Tescan, Micrion, Advantest, Schlumberger, AMAT, Micro Beam, and others. In this work, two dual-beam stations Lyra platform and Nanospace prototype which have been fabricated and commercialized by Tescan France and Orsay Physics companies respectively, are used in our research studies on nanopatterning and etching performance which would be presented in the next sections. Since a single FIB is insufficient even for nanomaterial elaboration or characterization because of milling and amorphization effects generated by ion imaging even at low energy, low ion beams current and small-time exposition; each single station combines a filtered-FIB column for nano-structuring and SEM column for imaging simultaneously. However, the main difference between the two Cross-beam systems rely in their configuration, and the presence of other accessories which marks the specificity of each station and its prominent key features that would be detailed in the following parts. Finely focused ion beam generated with field emission ion source of FIB systems has in diameter from a few nm to a

few μm , with currents from 1 pA to several tens of nA with high resolution through positive ions with energies ranging from 5 keV - 150 keV depending on what can be done with the beam, according to the physical processes which occur from the interactions of ions with solid. Image formation, image analysis, scattering theory, optical design, aberration theory, electron microscope design, particle accelerators and other considerable components are crucial in charged particles optics field.

II.1. Comparison and innovation: LYRA & NANOSPACE

II.1.1. LYRA technology

The Lyra platform is a dual beam which incorporates SEM column and a FIB column. The ion column is tilted at 52 degrees from the SEM column. They are incorporated into one system and working under a high vacuum environment (around 10^{-5} mbar). The Lyra station is monitored with a Tescan software which allows users to operate easily each beam. It includes a fully automated microscope set-up, working either with the ion or the electron beam, and graphical user interface to define and operate the FIB patterns.

The Lyra FIB column is equipped with two ion pumps for ultra-low ion scattering effect. A gun valve can isolate the gun system to facilitate the exchange of the ion source . The FIB ion column is specifically design to work with Liquid Metal Ion Source (LMIS). The gun can emit either Si, Au, Ge, Ga, etc. ions, depending on the alloy of the ion source. In these studies, we mainly worked with AuSi, GeSi and Ga sources. Ga source are the most commonly used. As gallium liquefaction temperature is close to room temperature, the start up and set up of the source is ease. Depending on the application targeted, other ions can be more relevant. In our case, Si ions avoid any contamination of the sample during etching of a silicon-based wafer. On the other side, Au ions offer a higher sputtering rate, compared to Ga ions. It is useful to reduce etching time for large or deep patterns.

A LMAIS generates simultaneously all the ions and their different species (monomers, dimers, single ionized, double ionized, ...) at the same time. For instance, an AuSi source emits Si^+ , Si^{2+} , Si_2^+ , Au^+ , Au^{2+} , ... species. It is therefore necessary to select the working specie. In a Lyra column, a Wien filter is introduced between condenser and objective lenses. It deviates the ions as a function of their mass. When tuned, the Wien filter let the desired specie travelling straight through the filter. The other species are deflected and stopped by a “mass” aperture. The filter has a resolution higher than the neutron mass. I other words, a Wien filter is able to select a specific isotope of a chemical specie. It is mandatory as the lenses focus depends on the ions

mass. To achieve a good etching resolution, the beam must be composed of a single isotope. In the Wien filter, two opposite forces are applied to the travelling ions. One is due to an electric field, the other one to a magnetic field. By adjusting finely the value of each field, these two forces exactly compensate for a specific ion mass. For other masses, the ions are deviated from their original trajectory (parallel to the optical axis), and stopped by the mass aperture.

The ion current is selected thanks to a “probe” aperture located between the condenser lenses and the Wien filter. A higher aperture diameter induces a higher current, and therefore a higher signal to noise ratio. But it also increases the probe size and reduces the FIB resolution. A Faraday cup and stage current collector with a Keithley pico-amperemeter, are used to measure the probe current. The probe and mass apertures can be changed automatically as they are motorized. After aligning the optical axis of each component of the column, the FIB can be used for ion implantation, ion imaging or an ion etching.

The Lyra station includes an additional tool that can be used either for local layer deposition, or selective etching: the Gas Injection System (GIS). This device injects a specific gas close to the surface by means of a needle, that reacts with the incident beam and the substrate. The GIS setup of the Lyra consists in 5 independent gas reservoirs supplying capillaries with an automated temperature control. For our applications, it is mainly used for platinum or silicon oxide deposition.

The SEM column incorporated in the Lyra station uses an innovative and powerful four lens Wide Field Optics™ design, offering a variety of working and displaying modes. Moreover, a fast and precise motorized specimen stage eases the observations. However, as the electron gun is a tungsten heated filament, the resolution of the SEM is limited.

The station chamber is pumped via a turbomolecular and a primary pump which ensure quick and easy sample exchange and short times to reach the working pressure.

II.1.1.1. Scanning electron microscope

A SEM image is performed by scanning the sample surface with a focused electron beam. The electrons ejected from the analyzed surface, namely the Secondary Electrons (SE), are then collected. The pixel intensity of the final picture is “proportional” to the amount of SE collected at the corresponding location on the sample surface. The resolution of the SEM depends on the probe size and the acceleration voltage used. The probe size corresponds to the magnification of the primary electron source and the optical aberrations of the lenses. It is mainly required to

work with a circular probe shape and a gaussian intensity profile. The lens aberrations are reduced for short working distances. Therefore, a best resolution is achieved when the sample is close to the objective lens. In this case the depth of field is reduced. As a matter of fact, increasing the cone angle of the incident electron beam decreases the depth of field.

II.1.1.2. The electron column of the Lyra station

The electron column shown in figure 2.1 consists of:

- *An electron gun* which contains the source of accelerated electrons, a cathode, a Wehnelt cylinder and an anode. For electron emission, the cathode, consisting in a tungsten filament, is heated to a high temperature. The accelerating voltage of electrons (and therefore their energy) is determined by the voltage applied between the Wehnelt cylinder and the anode. The emission current can be changed by applying negative potential between the Wehnelt cylinder and the cathode. The whole gun system works as a “virtual source” of electrons with the following specifications:
 - Dimension: 25 – 50 μm ,
 - electrons energy: from 200 eV up to 30 keV,
 - emission current: up to 300 μA
 - brightness: 106 $\text{A}/\text{cm}^2\text{sr}$.

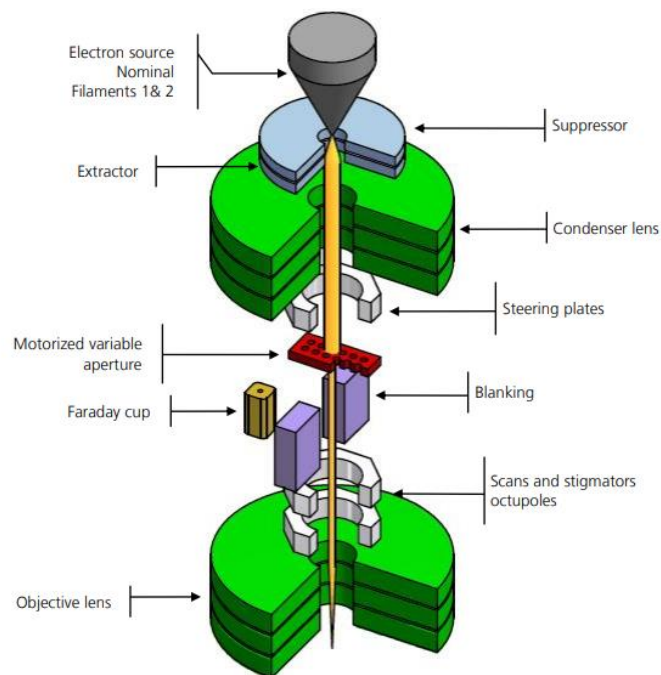


Figure 2.1. SEM electron column presenting the main components. [OP]

- *A system of electromagnetic deflection coils* called “gun centering option”, which is located after the gun in order to tilt the electron beam emitted from the gun. It centers the axis of the optical system of the column. It is controlled by the “gun alignment” function. The gun is correctly centered if the electron beam is parallel and close to the optical axis of the column. Experimentally, the image is brightest.
- *Spray apertures* that are placed under the centering coils of the gun. They stop the marginal parts of the electron beam emitted by the gun.
- *A pair of condensers lens (C1 and C2)* that are used to both form the beam and limit the amount of current in the beam. It works in conjunction with the condenser aperture to eliminate the high-angle electrons from the beam .
- *A Condensor aperture* that is used to define the size of the final incident beam. It is placed at the end of the central vacuum pipe of the column, around 60 mm under condenser C2 with an optimum aperture 50 μm .
- *An auxiliary lens* type IML which is a magnetic lens for displaying an image if the objective lens is off. The change of the IML excitation causes the shifting of the electron beam across the optical axis and therefore it is necessary to compensate this shifting by means of the IML centering coils.
- *A stigmator* consisting in an electromagnetic octupole. It is used to compensate for astigmatism in all the displaying modes.
- *Scanning coils* that are formed by two stages of the deflection coils. First a scanning ramp is connected to the coils and the scanning speed of the electron beam is determined by the ramp frequency; thus, the microscope's field of view and the magnification is determined by the amplitude.
- *An objective lens* that is the last magnetic lens of the column. It focus the electron beam on the sample.

II.1.1.3. The ion column of Lyra station

The ion beam is created and positioned by the ion column. It can be used for sample surface imaging or for creating locally defined structures on the specimen. All these applications depend on the ion beam parameters: ion energy, beam current and spot (beam) size. As mentioned before, the spot size determines the resolution and the sharpness of the created patterns. Without lens aberrations, the spot size would be determined by the ion source size and the demagnification. In practice, the spot size is mainly defined by the aberrations of the final

lens. If the beam energy decreases, the spot size increases because of the chromatic aberration of the objective lens and the influence of the spatial charge.

The ion optics can work in different modes. A high ion beam current ($\sim 1\text{--}10\text{ nA}$) is used for the milling of big structures (rough etching), by the means of a high etching speed. But the spot size is big in this mode, and consequently the sharpness of the objects created is poor. Moreover, it is not used for imaging because of the highly destructive effect on the observed sample.

A medium ion beam current ($\sim 100\text{ pA}$) can be used for short term imaging at low magnification. But it is mainly used for polishing of rough created objects, using a small spot size for the sharpening the structures edges.

A low ion beam current ($\sim 1\text{ pA}$) can be used to perform ion imaging on high magnification with a minimized destructive effect on the sample. Very small objects with maximal edge sharpness can be patterned. Unfortunately, the etching speed is very low and this mode is not suitable for creating big patterns.

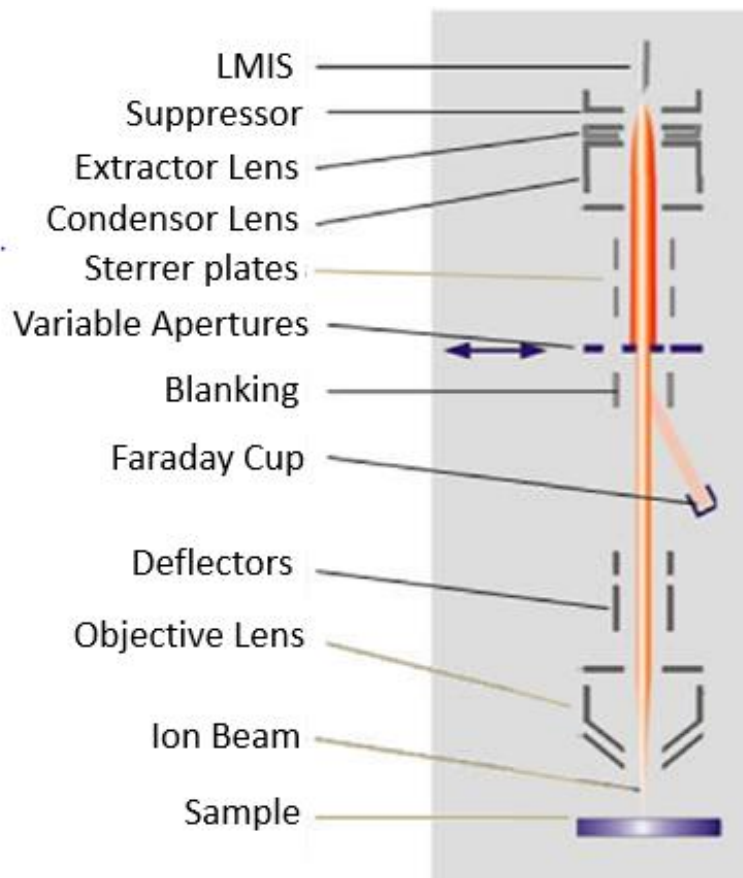


Figure 2.2. scheme of internal view of the FIB column [OP].

The ion column has different parts. The top part contains the ion gun which is the source of the accelerated positive ions; it has a tip, a suppressor and an extractor. Connected to a positive electric potential, the tip is a tungsten spike, dipped into a suitable material according to the required ion type. The material could be simple metallic elements (such as Ga, In, Sn, Al, Cs...) forming LMIS sources or an alloy of multiple elements (Au-Si-Be, Pd-As-Be, Au-Ge, Au-Si, Au-Si-Ge...) forming LMAIS sources. A Taylor cone is created by applying a high electric field. It forms a very thin tip acting as a virtual source with a size of several nanometers. Using an extractor electrode, a strong electric field is created just in front of the tip with a negative potential of several kilovolts. The emission current corresponds to the ions emission from the tip and depends on the extraction voltage. The accelerating voltage of the ions (and thus their energy) is defined by the potential difference between the tip and the ground. The emission current is stabilized with the suppressor electrode. During the heating procedure of the source, generally a gallium one, a thin layer of the liquid metal (Ga) is restored on the tip, and in order to avoid ion material evaporation and protect the ion source's life time, the heating must be performed on purpose for LMIS sources and continuously for LMAIS sources.

The final ion current and final spot size of the ion beam are controlled by the condenser lenses which are strong electrostatic lens. The intensity of the beam is selected by means of an aperture. Several sizes of molybdenum aperture, can be selected and aligned with a high precision motorized control system. Indeed, both the ion beam current and the beam spot size are defined by the couple of the aperture changer and the condenser voltage.

The ion column is a filtered one due to the presence of the Wien filter and mass apertures, that can make possible the selection of one type of ion from the ion beam in the case of alloy-based ion sources.

In order to prevent an unwanted impact of the ion beam on the specimen, the FIB uses blanking electrodes which deflect the beam to a Faraday cup during the "blanking time". The Faraday cup is located just below the blanking electrodes system. The beam is precisely positioned on the sample by an electrostatic octupole. It monitors the beam scans over the specimen and corrects beam astigmatism.

Finally, the objective electrostatic lens is used for focusing the beam on the specimen surface, which is located in the FIB/SEM beam-intersection. To get high resolution ion images and sharpest edges for the patterns, a proper centering of the ion optics is required.

II.1.1.4. Focused Ion Beam Imaging

As already mentioned in chapter I, secondary electrons (SE) are created from the interaction of the primary ions with the surface. They have a low energy and can be detected by a common SED for surface imaging of the specimen. The ion imaging is destructive since the specimen atoms are ejected from the surface. The scattering rate depends especially on the type of material. It is low in case of hard materials (diamond, titanium), and higher for soft materials (gold, copper).

Ion imaging is performed with a very low ion current ($\sim 1 - 10$ pA) and as quick as possible in order to limit the sample change. For that reason, single scan imaging is the best recommendation to use. Ion imaging is more sensitive to the surface of the sample. As a matter of fact, compared to an electron beam, an ion beam much more interacts with the substrate atoms. As a consequence, the SE comes from a lower specimen depth. Ion images offers better information about surface topology. Furthermore, the incoming ions can experience the channeling effect, depending on the ion size. The penetration of ions in the target depends on the crystallographic orientation of the crystal; it may be much deeper along the crystallographic planes. When channeling occurred, both the sputtering rate and secondary electron emission are lowered. In the image, it is displayed as darker areas, compared to the areas where there is no channeling effect. The image contrast caused by the channeling effect can be observed in for polycrystals, and used for the detection of the grain boundaries, as shown in the figure below:

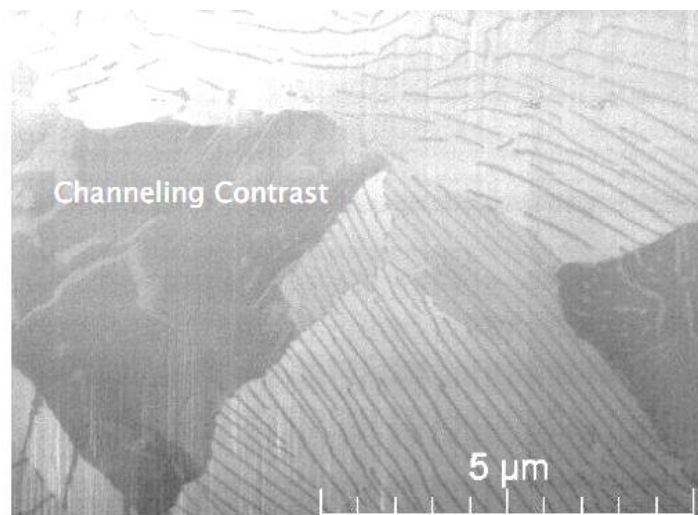


Figure 2.3. Detail of steel cross section showing the effect of ion channeling contrast [OP].

II.1.1.5. Focused Ion Beam Assisted Etching and Deposition

Various range of applications can be performed with a dual beam-FIB (nanopatterning, implanting, sputtering...) as presented in the following table:

Process	Necessary devices	Example of use
Electron Beam Lithography (EBL)	SEM with beam blanker	Photo resists exposure
Electron Beam Deposition (EBD)	SEM with beam blanker, GIS	Deposition of nanodots or initial protection layers for TEM lamellae
Ion Beam Etching (IBE)	FIB	Cross sectioning, preparation of TEM lamellae
Ion Beam Deposition (IBD)	FIB, GIS	Deposition of protection layers for TEM lamellae

Table 2.1. Particular processes with the devices for different applications with examples. [OP]

II.1.1.6. Gas Injection System (GIS)

The Lyra station is equipped with a GIS presented in the figure 2.4. It allows either the deposition of finely shaped metallic/insulating microstructures or a locally enhanced/selective etching of various materials.

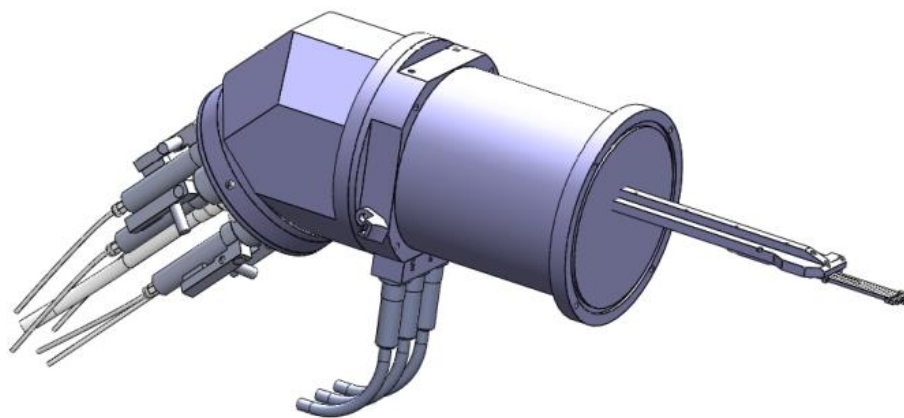


Figure 2.4. GIS in combination with FIB in Lyra platform [OP].

II.1.1.7. Detectors

A set of detectors are designed for collection of various signals, resulting from electron or ion beam interaction with the sample surface.

i. SED

Contrary to material contrast of back-scattered electrons, Secondary electrons enhance topographic contrast. They are detected by SED that works in high vacuum only and it is a basic standard detector always present in the microscope. In Lyra, the SED is of Everhart-Thornley type, designed with the grid on the front part which has positive potential for the attraction and acceleration of the low-energy secondary electrons arising from the specimen surface and focus them onto the scintillator. The impact of the electrons on the scintillator produces light flashes that are transferred to the photo-multiplier outside the chamber of the microscope, through the light guide.

ii. LVSTD

The Low Vacuum Secondary Tescan Detector is also another detector of secondary electrons, but working under low vacuum mode as illustrated in figure 2.5, and suitable for non-conductive samples investigation. The LVSTD consists of a standard Everhart-Thornley detector situated in a separated detector chamber which is pumped by a small turbo molecular pump.

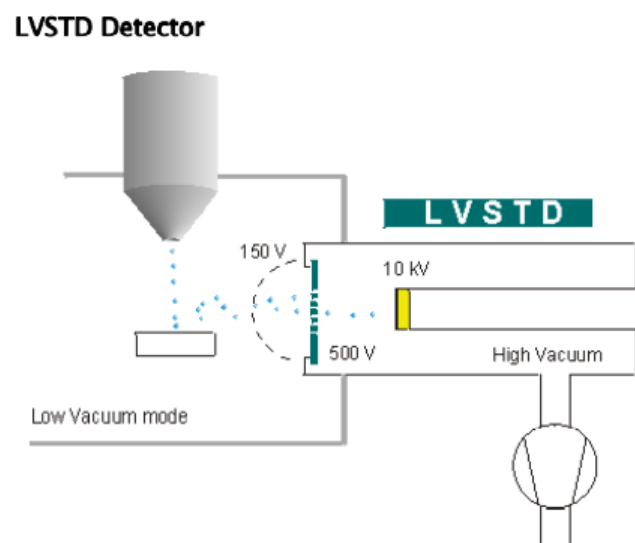


Figure 2.5. Scheme explaining the principle of work of an LVSTD. [OP]

iii. BSED

The Back-Scattered Electrons Detector works under both high and low vacuum. It is an annular (YAG) mono-crystal scintillator with a conductive surface placed in the optical axis directly under the lower pole extension of the objective. The BSE is sensible to the chemical composition of the sample. Atoms with high atomic number produce more BSE. These electrons impact the scintillator with the primary energy. The emitted photons are guided through the side outlet of the scintillator and by means of the light guide to the cathode of the photo-multiplier. The photons are the processed in the same way as the signal coming from the secondary electrons. To allow the retraction of the detector from under the pole piece position if the detector is not used, the BSED is manufactured in an R-BSE (Retractable BSE) version, as close as possible to the objective

iv. CLD

Depending on the wavelength range of the detected light: in the mainly visible and near UV light (350 – 650 nm range) or in the near IR, UV and visible light (185 – 850 nm range), the cathodoluminescence detector is available in two versions, and working also in high as well as low vacuum. It is necessary that the Lyra IR camera (Chamber View) must be switched off during operation of the CL detector.

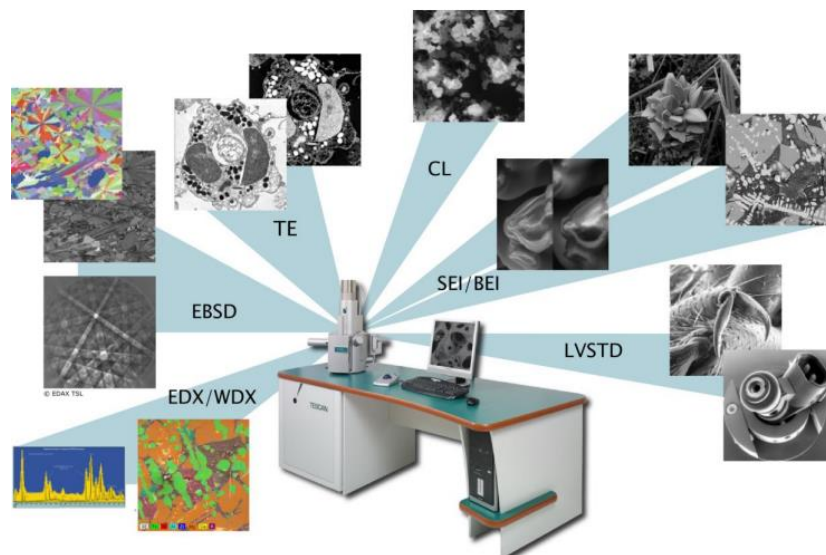


Figure 2.6. Different types of detectors that might be incorporated in the Lyra station for more data characterization with nature of samples. [OP]

II. 1.2. Nanospace technology

The NanoSpace configuration is a Stand-alone UHV device with a Chroma-(ExB) Mass separating FIB (MS-FIB) and an e-CLIPSE plus SEM column. It is fully customizable system in which each element constituting the instrument is chosen to best meet user requirements. It can be connected and adapted to any other instruments/UHV chambers despite some mechanical modifications. For instance, it can be integrated to an MBE to avoid the samples contamination between epitaxy deposition and FIB patterning.

Basically, the FIB is combined with a SEM, where the electron and ion beams intersect at a 52° angle at a coincident point, near the sample surface, allowing immediate, high resolution SEM imaging of the FIB-milled surface.

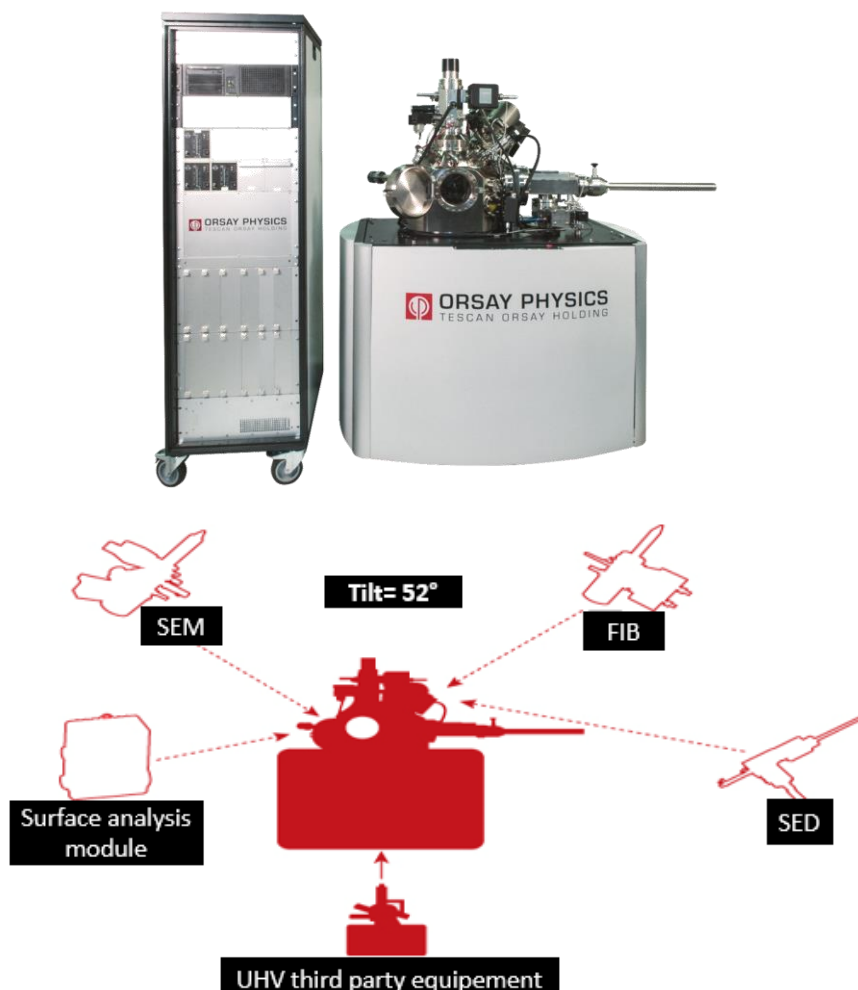


Figure 2.7. Nanospace dual-beam FIB/SEM platform design.

The Nanospace use the same Wien filter as for the Lyra, when coupled with LMAIS.

II.1.2.1. FIB components

i. FIB column

A schematic view of the FIB column of the NanoSpace system is shown in Figure 2.8. The various components of the column are described hereafter.

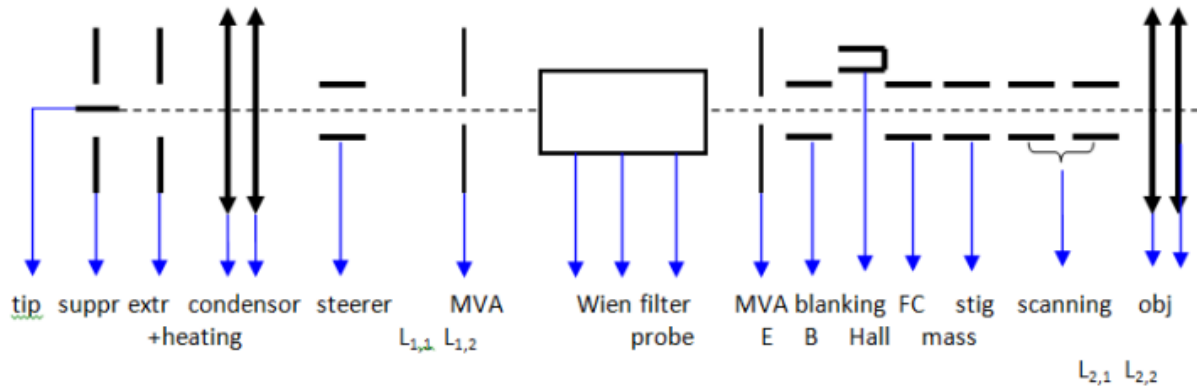


Figure 2.8. CHROMA FIB column schematic view. [OP]

ii. LMIS source

In FIB instruments, liquid metal ion source, LMIS, due to their relevant performance, are mostly used as ions source. Among them, LMIS using Ga as a metallic element source, which presents several advantages [13], are generally used. Liquid metal alloys sources (LMAIS) have also been developed to address various applications (e.g local implantation/doping).

The ion field emission mechanism of LMIS source relies upon the extraction of ions emitted from the source under the application of an intense electric field (see figure 2.9).

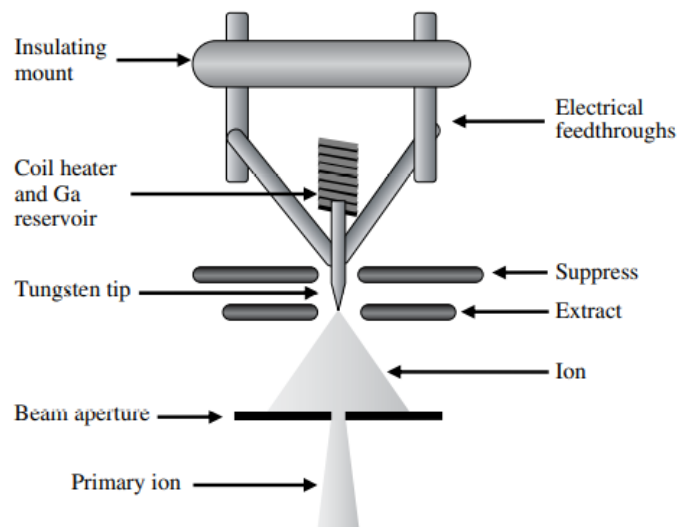


Figure 2.9. The focused ion beam formed from LMIS source. [1]

A tip of a blunt needle of 5-10 μm radius has its apex coated with a thin film of liquid metal flowing from a heated reservoir; A high voltage around 6 keV relative to the source is held on the extractor electrodes creating an intense electric field at the tip needle which ionizes the gallium (or other element LMIS/LMAIS) and the liquid metal is drawn into a fine tip which is called ‘Taylor cone’ [2] (or Taylor-Gilbert cone) of Ga LMIS in FIB systems. Through the field evaporation phenomena at the tip in the high electric field (Ga) ions are emitted from the tip then are pulled out subsequently to pass through the column, condenser lenses and probe apertures and focused into a beam which can be scanned over the sample surface. Conventional FIBs systems use an acceleration voltage around 30 keV, and it may be as high as 50 keV or as low as 0.5 keV.

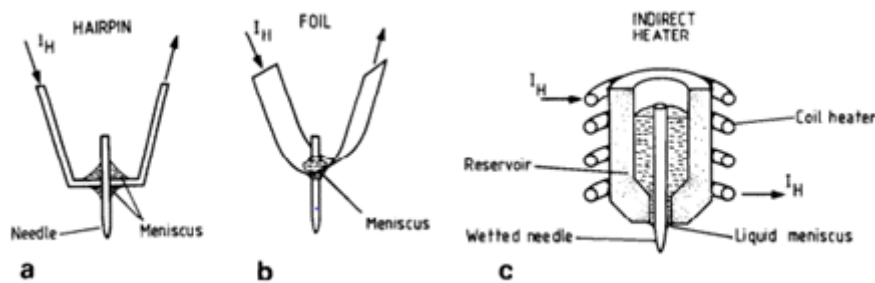


Figure 2.10. Three basic design of blunt needle LMIS: (a) Hairpin filament source, (b) Hughes type, (c) Culham type. [3]

LMIS sources have different designs, figure 2.10 shows the three basic source configurations: direct heating is applied for both the hairpin [4] and ribbon heater or Hughes type [5] sources, whereas for Culham type, the separate resistive heater assembly is used to maintain the source temperature since it has a larger more substantial reservoir through a heater filament which is not in contact with the liquid metal or alloy [2].

The performance of the source is related to the good wetting of the liquid film to the tip of the blunt needle emitter since if it is badly wetted, formation of droplets would occur with subsequent drying up of the emitter surface leading to a loss of the liquid metal on the needle resulting in a source failing. In addition, in the case of direct heating type sources, needle and reservoir materials must be both undissolved and uncorroded when they are wetted by the thin film of liquid metal. For example, tungsten is well adapted as needle and filament material when Ga and also other metals alloys source elements are used. In general, the source energy is defined by V_{source} , and the source can operate from 0.5 to 5 kV (in low energy mode) and from 10 to 30 kV (in high energy mode), after a threshold of extraction, the source is emitting and the emission current increases with the extraction voltage (see figure 2.11). The suppressor

(V_{sup}) is used to regulate the emission to a given current. The main advantage of the suppressor is that the modification of its voltage V_{sup} has no influence on the optics. Here also, the higher the suppression voltage, the higher the emission current is. Emission current can so be adjusted between 1 uA and 30 μ A, optimum operation conditions are between 1.0 and 3.0 μ A values, depending on the application and the nature of the sample.

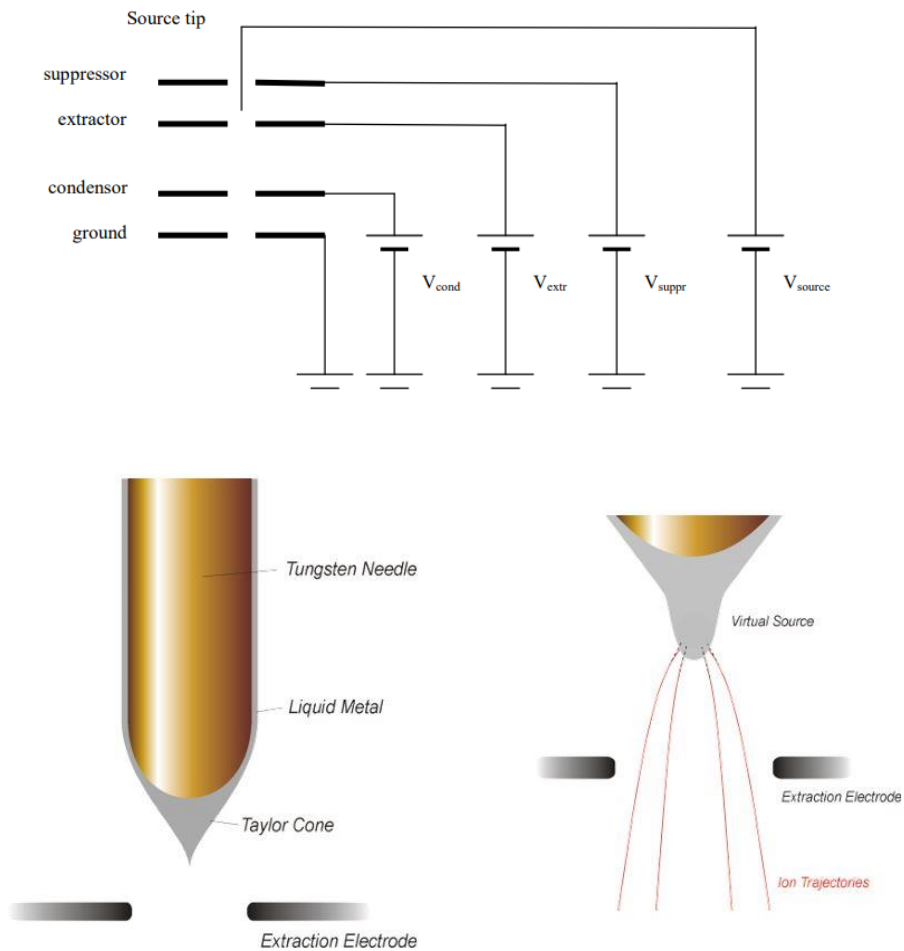


Figure 2.11. Potentials applied on the tip of LMIS source for ion emission through the formation of the Taylor's cone at the apex. [OP]

LMIS is practically a "point" source with high angular current intensity which facilitates its operation with beam currents of a few micro amperes and stable for many hours (> 1000h) in a modest vacuum (10^{-5} ~ 10^{-7} torr). The emitting area is ~ 10 nm in physical diameter but the effective area looks like ~50nm to the focusing optics because of the Coulomb interactions in the beam.

iii. LMAIS source

To expand FIB applications, in addition to Ga ions, the benefit from other ion species in the μm or nm range has been possible for local ion implantation, ion beam mixing, ion beam synthesis, or Focused Ion Beam Lithography (IBL) thanks to the use of the promising LMAIS. Over electron beam lithography or other lithography techniques, IBL has showed potential advantages since the ion species used in FIB has significantly influence on the physical and chemical nature of the resulting nanostructures—in particular, their electrical, optical, magnetic or mechanic properties. Continuous investigations on alloy sources yield to the availability of LMAIS in the FIBs including nearly half of the elements of the periodic table (Figures 2.12 and 2.13) with long life-time, high brightness, and stable ion current sources [XX]. To produce beams of elements other than Ga for various applications like local implantation, AuSi and AuGe alloy sources have been developed and integrated in our stations, Nanospace and Lyra platforms.

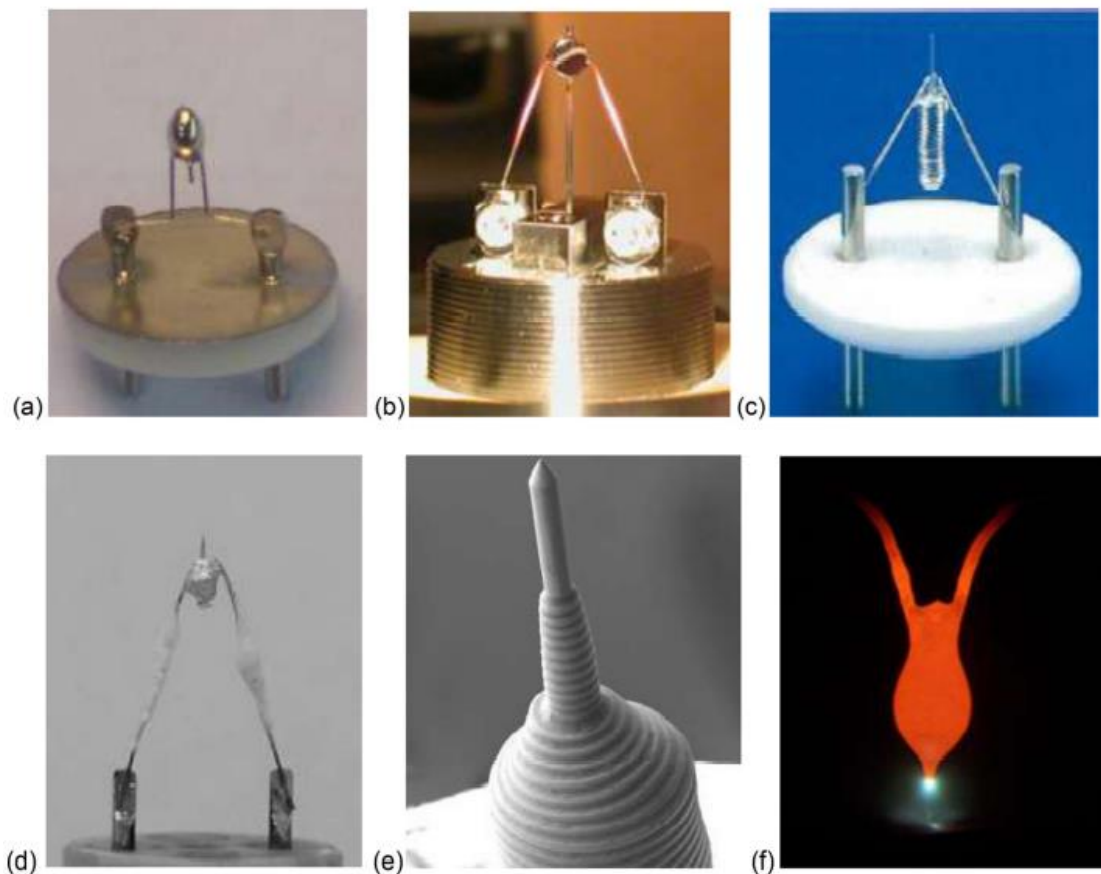


Figure 2.12. Various images of alloy sources: (a) AuGeSi LMAIS (HZDR), (b) AuSi LMAIS (Raith GmbH), (c) typical Ga—LMIS (FEI and Denka), (d) AuDySi (RUB), (e) Ga—LMIS and (f) CoNd LMAIS emitter during high current operation at $T\sim 700^{\circ}\text{C}$ (HZDR). [6]

H																			He
Li	Be											B	C	N	O	F		Ne	
Na	Mg											Al	Si	P	S	Cl		Ar	
K	Ca	Sc	Ti	V	Cr	Mn	Fe	Co	Ni	Cu	Zn	Ga	Ge	As	Se	Br		Kr	
Rb	Sr	Y	Zr	Nb	Mo	Tc	Ru	Rh	Pd	Ag	Cd	In	Sn	Sb	Te	I		Xe	
Cs	Ba	La	Lu	Hf	Ta	W	Re	Os	Ir	Pt	Au	Hg	Tl	Pb	Bi	Po	At	Rn	
Fr	Ra	Ac	Lr	Rf	Db	Sg	Bh	Hs	Mt	Ds	Rg	Cn							

La	Ce	Pr	Nd	Pm	Sm	Eu	Gd	Tb	Dy	Ho	Er	Tm	Yb
Ac	Th	Pa	U	Np	Pu	Am	Cm	Bk	Cf	Es	Fm	Md	No

Figure 2.13. The red marked elements in the periodic table can be provided as single or doubly charged mono- or even as heavy polyatomic ions (cluster) by LMIS and LMAIS in FIB columns [7]. Additional or same ions may be used in FIB systems applying different source types like ILIS [8], MOTIS [9], GFIS [10] or others [11], in particular, high current [12] or plasma sources for Xe ions from [13].

iv. Ion beam current profile

In FIB, a good approximation for the radial distribution of the ion beam is assumed to be a Gaussian beam profile. Beam profile is usually affected by the true shape of the beam-defining apertures in the ion column, the ion column alignment, and the vacuum in the ion column. However, none of these parameters will exactly be known.

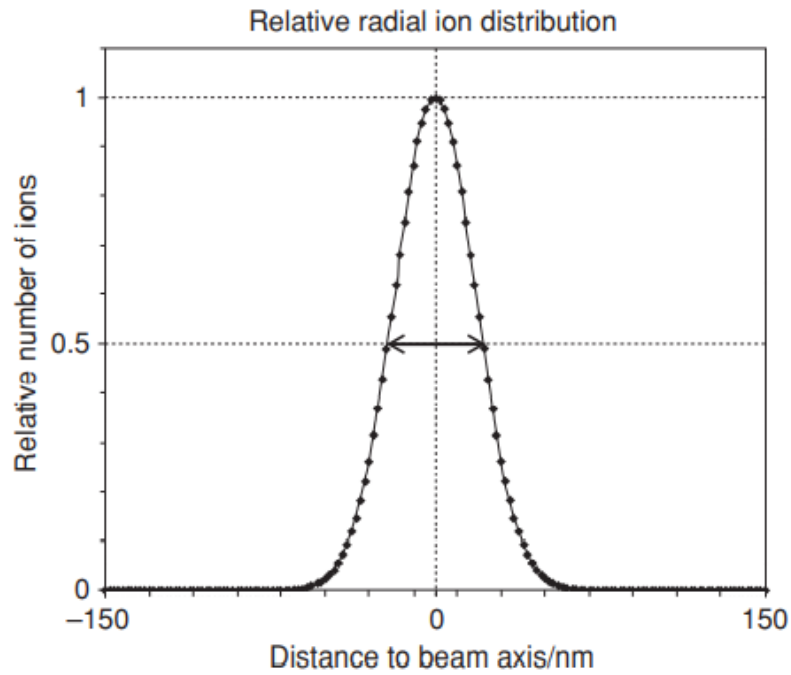


Figure 2.14. Gaussian distribution as an approximation of the radial distributions of ions in the beam for an accelerating voltage of 30 kV and a beam current of 93 pA. From [14]

In figure 2.14, the arrow illustrates the full width at half maximum (FWHM) of 24 nm of the Gaussian distribution of FEI-FIB column [xx];

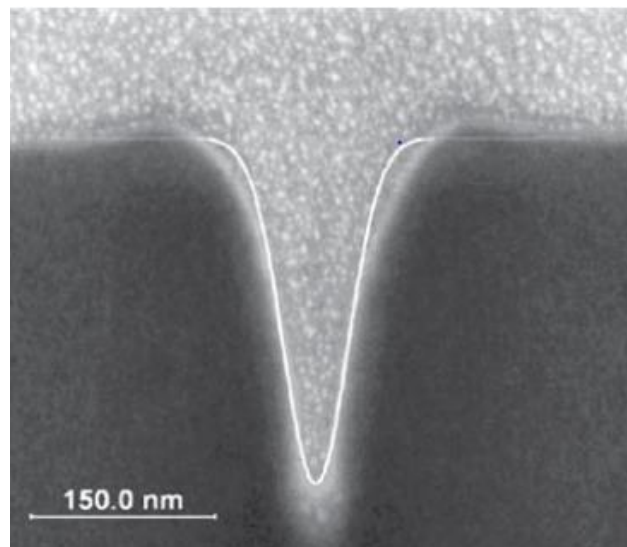


Figure 2.15. Single pixel line profile milled with FIB at 30 kV and 93 pA into an Si surface.

Figure 2.15 shows a SEM cross-section image of a silicon layer after FIB milling. The dark material refers to the Si-substrate patterned by FIB while the brighter grainy material, is used

to fill the trench during the FIB-cross-sectioning., a Gaussian profile is overlaid to validate the assumption of a Gaussian FIB beam by comparing it to the real trench profile [15].

v. *Steering plates*

Localized between the condenser lens and the apertures, steerers, composed of four plates operating in pairs along the X and Y axes, are used either to tilt or to shift the beam, and also to correct the astigmatism when the correction obtained by the octupole lens is not sufficient.

vi. *Blanker and Faraday cup*

The FIB is equipped with an electrostatic fast beam blanker that allows to deviate the beam from its normal path so that the beam doesn't reach the sample at all. Thanks to the blanker, the beam can be deviated in a Faraday Cup present in the column for probe current measurement. For this purpose, a well-defined blanking voltage is applied on the beam by the blanker. The Faraday Cup is coupled to an electrometer from the station electronics. Also an external pico-amperemeter is available and can be coupled with either the Faraday Cup column or the sample stage to measure a precise probe current value in the range from 0.1pA to 100nA

vii. *Condensor and objective lenses*

- *Condenser Lens*

The condenser consists of three electrostatic lens which are directly placed at the output of the source and are used to adjust, in combination with the aperture and the energy, the shape the beam and make it convergent, parallel or divergent depending on the desired optical mode. Moreover, depending on the condenser tuning, the beam can have a real cross over or a virtual one (collimated mode) where the symmetrical mode refers that the first electrode of the lens is at zero potential while the asymmetrical mode is obtained when the first electrode is at the potential of the electrode of the extraction.

- *Objective Lens*

The objective is an electrostatic lens specially designed for low aberration coefficients allowing focusing the beam to reach ultimate spot size at the sample. We have two objective lenses in the Chroma column, the first one is situated at 6 nm from the sample surface used for high current and high energy applications, whereas the second one, is at 12nm distance from the surface and used for low both energy and current.

viii. *Scanning and Stigmators octupoles*

They are performed by variable voltages applied on two octupoles, located after the Faraday Cup and before the objective lens. These components perform the functions of scanning, correcting astigmatism and beam shifting.

ix. Detectors

In the Nanospace station, only a SED is installed (Figure 2.16) . It allows for greater topography imaging even at low particle emissions due to the highly effective secondary electron collection performing best images quality with a sufficient brightness. It is based also on the **Everhart-Thornley detection** principle including a scintillator, a light pipe and a photomultiplier to intensify effectiveness of gathered secondary electrons. In addition, it works under any vacuum chamber and range. Some of the OrsayPhysics SED key features are given in table 2.2.



Figure 2.16. Orsay Physics SED.[OP]

Key Features	
Adjustable parameters	Collector voltage / Accelerating voltage / Brightness / Contrast
Main Characteristic	Non-sensitive to light detector
Adaptation Requirement	35 CF flange
Optional UHV configuration	Maximum bakeout temperature is 120°C

Table 2.2. Nanospace station SED key features [OP].

II.1.2.2. Chroma FIB column

As described above the simplest and most widely used ion beam columns consist of two lenses (a condenser and objective lens) to define the beam and then focus it on the sample, beam-defining apertures to select the beam diameter and current, deflection plates to raster the beam over the sample surface, astigmatic poles to ensure a spherical beam profile, and a high-speed

beam blunker to quickly deflect the beam off the sample and onto a beam stop such as a Faraday cup. Because the focusing strength of an electromagnetic lens is directly related to the charge/mass ratio of a particle, it is impractical to build electromagnetic lenses for ions (which would weigh thousands of kilograms); thus, focusing and steering are performed using electrostatic components rather than the electromagnetic components used for electrons. The size and shape of the beam intensity profile on the sample determines the basic imaging resolution and micromachining precision.

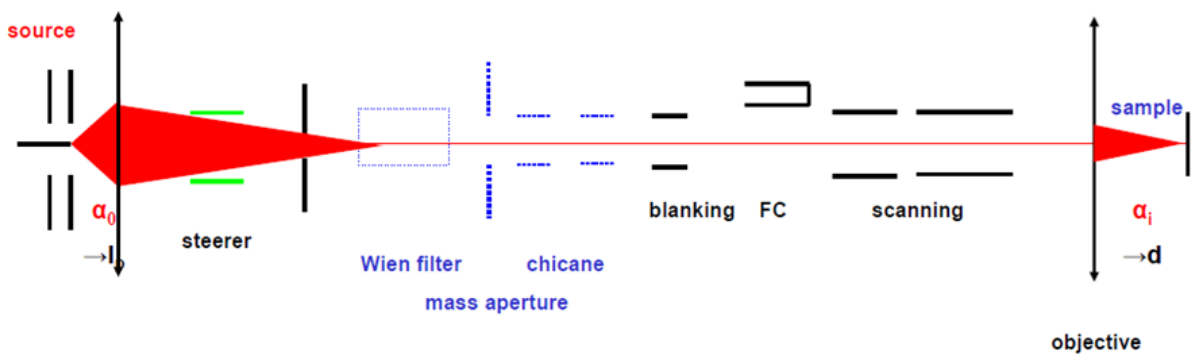


Figure 2.17. The optical scheme of the focused ion beam column.

However, in the Chroma FIB column, the ion beam which is extracted from the source, passes first through the condenser lens, then is straightened by the steerer plates ahead of the Wien filter (described in the next paragraph) in order to separate all the masses of the different ionic species present and emitted by the LMAIS. After that, the desired ions are selected using an electrostatic force applied in the Wien filter, and then the ion beam is scrolled in front of one of the mass diaphragms. The choice of the mass diaphragm allows a compromise between beam intensity and resolution. At the output of the mass diaphragms, the beam is deflected to the Faraday cage by means of blanking, so as to measure the value of the probe current. A series of metal plates mounted in an octupole form allow partial correction of astigmatism effects due to the lenses and the Wien filter. Focusing of the beam on the surface of the specimen is achieved by the objective lens.

II.1.2.3. Mass separating FIB column [E*B]

Providing the best separation of one species of ion out of a beam consisting of a mixture of ions with different axial velocities is the main purpose of the Wien Filter, also called E x B mass separator. The important design parameters for the E x B mass separator have been analysed by

Seliger [16]. However, the performance of the column can be seriously degraded possibly by two inherent aberrations that are astigmatism and chromatic aberration.

The forces inside the separator also focus the beam along with the spatial dispersion of the beam, since they are not axially symmetric, so that a circular beam entering the separator emerges in elliptical shape because of the astigmatism introduced into the undeflected beam. Particles which arrive between the electric field plates at different positions and therefore different voltages, experience a difference in total acceleration which make the astigmatism arising. Figure 2.18 shows a schematic of the separator and the principle of its operation.

The separator used was 7.6 cm long, with a 0.32 cm spacing between the plates, with a permanent magnet of 1 T and a maximum voltage of 6500 V, (from Hughes Research Labs). As known, there is a limitation on the smallest beam size obtainable when an $E \times B$ mass-separator is employed which introduces chromatic aberration that can also be appreciable.

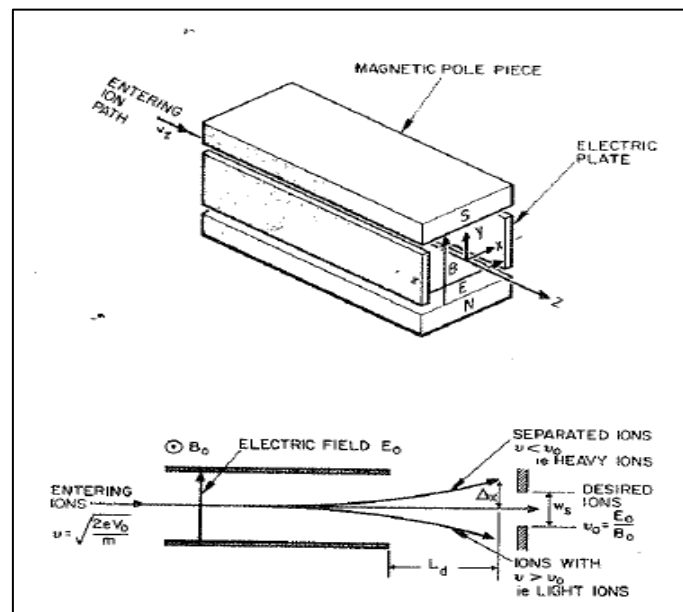


Figure 2.18. schematics of the mass separator and the principle of its operation. [16]

An LMAIS is composed of two elements chemicals at a minimum, the goal is to be able to separate them perfectly, out of column, so that each ion species can be used completely independently. In the case of an AuGe liquid metal alloy ion source, several ionic monomeric species, dimers with different degrees of ionization would be emitted, such as Au_n^{m+} , $Au_pGe_n^m$ + in greater or lesser quantity.

The Wien filter uses a crossed electrostatic field \mathbf{E} producing a force which is expressed as: $F_{Ex}=q \cdot E_x$ and magnetic \mathbf{B} field which produces a force $F_{By}=q \cdot v \times B_y$ to select the moving

particles based on its velocity (Figure 2.19). These two fields create an electromagnetic force, given by $F = q \cdot E + q \cdot v \times B$.

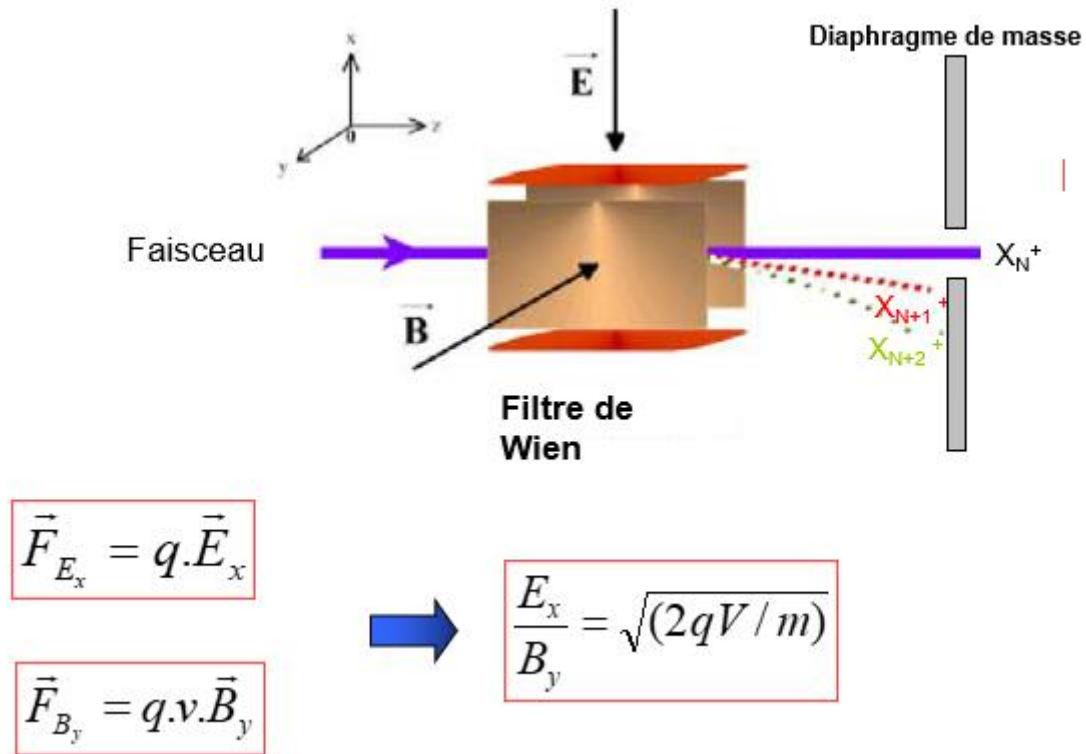


Figure 2.19. Schematics of the electromagnetic forces in the Wien filter. [OP]

Table 2.3 gives some of the key features of the Nanospace platform FIB column .

Key Features	
Source	LMAIS (Liquid Metal Alloy Ion Source) AuGe / AuSi / Bi / Ga
Ion Species	Au ⁺ , Au ⁺⁺ , Au ₂ ⁺ , Au ₃ ⁺ , Ge ⁺ , Si ⁺ , Si ⁺⁺ , Gold clusters (Au _n ^{q+} with n/q up to 100), Bi ⁺ , Bi ⁺⁺ , ...
Energy Range	500 eV - 30 keV
Probe Current	0.1 pA - 50 nA
Characteristics	High mass resolution ExB Wien Filter with 30 movable acceptance apertures (M/ΔM > 45)
Miscellaneous	Alternative LMAIS can be available upon request

Table 2.3. Some key features of the Nanospace station FIB column. [OP]

II.2. Ion Beam alignment with Wien Filter

II.2.1. Alignment SEM\FIB

There are different kind of techniques to align the beam to the centre of a lens, in general the main principle is the same but differences are made up with the configurations of each dual beam system (Figure 2.20). The sample must be at FIB/SEM intersection, and each column is aligned properly from this configuration.

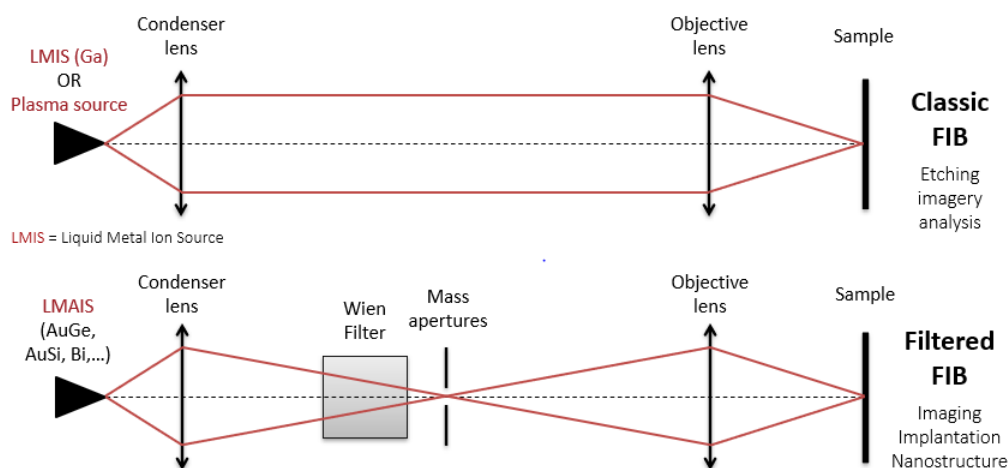


Figure 2.20. Schematics of LMIS and LMAIS main differences in ion optics. [OP]

The column is tuned for high resolution work when the beam is in the "optical" center of the lens which minimizes the aberrations also, (the ray that passes through the center of a lens, will then be undeflected by the lens). Since the beam consists of bundles of rays, there is a point of placement within the lens for the beam which causes the image to go into and out of focus without lateral image motion when the lens strength (i.e., focal length) is changed.

To align FIB/SEM station, a point of FIB-SEM intersection must be found firstly with the Z axis of the stage-sample, a little image-shift could be corrected, in the case of tilted stages with SEM beam shift and image transformation correction to minimize the distortion of the SEM image caused by the tilt angle of the electron column and vis versa. After that, each particle column is aligned separately on a feature big enough in the intersection area of the sample.

The alignment of the FIB column usually consists of two-step process: a primary and a secondary alignment; the primary alignment is based on the alignment of the source on the condenser (L₁₂) axis where the beam is in Cross-Over mode, while the second alignment aims

at aligning the beam from the couple (source/condenser) on the objective lens (L_{22}) axis by adjusting the position of the aperture.

II.2.1.1. Align the source on the condenser and the beam in Cross-over mode

The primary alignment consists of : at an energy of 30 keV with a stable emission of 5 uA from the AuSi LMAIS source, generally, the source must be aligned to the first objective lens L_{21} , and then that beam must be aligned to the second objective lens L_{22} for multiple lens systems such as our prototype (two condenser lenses L_{11} and L_{12} , and two objective lenses L_{21} and L_{22}) , however in this procedure the alignment is accomplished using, for low currents and high-resolution mode, L_{12} condenser and the L_{22} objective.

After assuring a stable emission after starting the source, a pre-aligned condition, saved in the data base, corresponding to large probe apertures and 600 um or 400 um mass apertures is loaded; it is also possible to use centred conditions of (600\600) um as well as probe and mass apertures respectively or even (100\50) um alignment conditions saved after the last alignment. At this stage, Piezo Gun regulation of source centering and Wien filter are deactivated . Next, the condenser is set to 15kV, looking for the maximum current that results in maximum brightness by manually adjusting the gun screws that align the source in the optical axis of the column, then the probe and ground MVAs are centered. Another step is to raise the condenser up to 30 keV in +500 V steps, and in the case of a beam cut, try to bring it back in the same axis of the condenser and the objective, still using the side gun screws; once the signal has been resumed, return to 15 kV and centre the diaphragms and realign with a wobbling on the mass diaphragm, checking that the probe diaphragm does not cut the beam. This procedure is to be repeated until reaching 30 kV and at each beam cut until the whole range of the L_{12} condenser is reached. Note that it must be verified that in a range between L_{12} [15 kV; 30 kV] there is no current cut-off.

II.2.1.2. Align the source/condenser pair with the Objective L2

Once the primary alignment is complete, small apertures are used for the secondary alignment, then begin the isotope filtration. Reduce the Probe and Mass diaphragms to 100 μ m and repeat the exact same steps of the primary alignment from 15keV to 30keV in a loop. Then stop the wobbling on L_{22} by moving the Mass diaphragm while checking that it does not cut into the

Probe diaphragm (to be sure not to cut the beam through it). Then close the top and bottom diaphragms 50 μm and activate the WF for filtration and desired ions.

The Nanospace and Lyra stations were first aligned using this procedure and then the Wien Filter is switched on and combined with a set of mass apertures for ion species and isotopic filtration.

As an example, for the Nanospace station, the ions were accelerated under 30 keV in energy, and the condenser lens L12 dedicated to low current and low energy applications was fixed at 25,64 kV and using Wien Filter to discriminate the AuSi ion species with their sample current measured with a picoammeter and a Faraday cup stage to get the filtering conditions given in table 2.4 below:

Nanospace station	Electric Field (V)	Associated element	Ion mass sample current
<i>CHROMA- FIB</i>	14	Au ₄ ⁺	2,9 pA
	17	Au ₃ ⁺	6,9 pA
	20,6	Au ₂ ⁺	1,2 pA
	*****	AuSi ⁺	*****
	25,5	Au ⁺	80 pA
	30,1	***	20 fA
	33,7	AuSi ⁺⁺	60 fA
	36,3	Au ⁺⁺	41,5 pA
	66,2	³⁰ Si ⁺	60 fA
	67,4	²⁹ Si ⁺	140 fA
	68,8	²⁸ Si ⁺	1,6 pA
	69	****	1,5 pA
	94,3	³⁰ Si ²⁺	740 fA
	96	²⁹ Si ²⁺	1,2 pA
	97,7	²⁸ Si ²⁺	23,2 pA

Table 2.4. Filtering conditions with Wien Filter at 0,5 A for ion mass separation in an AuSi LMAIS in a CHROMA FIB column of Nanospace station.

Similarly, the Lyra station were aligned under 30 keV to accelerate ions, and the condenser lens L1 was fixed at 25,8 kV and using Wien Filter to discriminate the ion species from AuGe LMAIS with their sample current measured with also a picoammeter and a Faraday cup stage for the following data (Table 2.5):

Lyra station	Electric field (V)	Associated element	Ion mass sample current
<i>VEGA- FIB</i>	59	Au ⁺	110 fA
	83,4	Au ²⁺	25 pA
	95	⁷⁶ Ge ⁺	0,5 pA

	96,4	$^{74}\text{Ge}^+$	2 pA
	97	$^{73}\text{Ge}^+$	0,5 pA
	97,6	$^{72}\text{Ge}^+$	1 pA
	99	$^{70}\text{Ge}^+$	1 pA
	134,6	$^{76}\text{Ge}^{2+}$	3 pA
	136,2	$^{74}\text{Ge}^{2+}$	17 Pa
	137,2	$^{73}\text{Ge}^{2+}$	3 pA
	138,2	$^{72}\text{Ge}^{2+}$	13 pA
	140,2	$^{70}\text{Ge}^{++}$	9 pA

Table 2.5. Filtering conditions with Wien Filter at 1 A for ion mass separation in an AuGe LMAIS in a VEGA FIB column of Lyra station.

i. Operating mode

Different modes can be used to operate a FIB column, high current applications, a cross-over for weaker resolution or high-resolution operation mode at low current using small aperture (Figure 2.22), For our experiments, only the cross-over mode coupled to small apertures of 10 μm and 20 μm in size were used for high resolution and low current with small ion beam spot size.

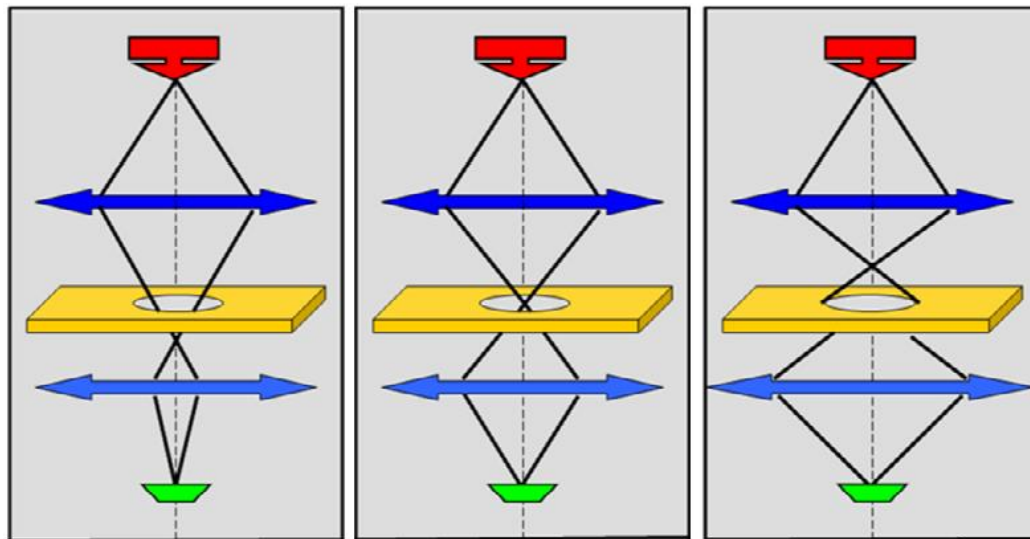


Figure 2.22. Scheme of different configuration of Crossover. [OP]

II.2.2. High resolution FIB/SEM imaging

Daily life, the unaided human eye can distinguish two points 0.2 mm apart with sufficient light, however being closer down to this distance, which is called the resolution of the eye, only one dot would be seen as appearance of the two dots or more. In microscope, there is even single

objective lens or more that are used to distinguish sample surface and structural data of small and closest details which exceeds human eye resolving power.

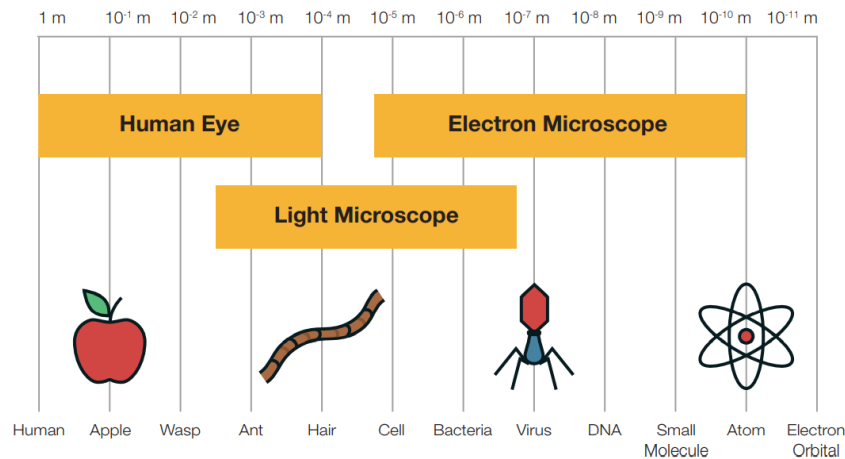


Figure 2.23. different scale of microscopes. [Thermo fischer]

The interaction between a focused beam whether electron or ion and the sample surface is the main base of either ion or electron imaging. Formed by the succession of pixel after pixel of the sample scanned synchronously to form a sample's image through the viewed, which has a brightness intensity that refers to the intensity of interaction of the particles with each point of the sample, it is noted that the beam is blanking only the selected area observed and shown in the screen. The specific detectors are incorporated in dual beam station depending on the desired information, for example the secondary electrons are used for topographical contrast, while the backscattered electrons are used for the chemical contrast, also the secondary ions are dedicated to crystallographic contrast data and the X-ray photons for elementary analysis of materials.

Images formed from either secondary electrons and ions are possible, since the incident ions produce both secondary electrons and ions. During ion imaging, the beam destroys the sample because it is scanning over its surface, even by sputtering, or modifying it at a rate determined by the incident beam current and sputter yield of the sample, limiting the time that it may images. Although the resolution of both techniques that are converging, and because of this destructive interaction, also poorer beam current-probe size characteristics, scanning ion imaging is not as widely used as SEM, however it might be less destructive than scanning electron imaging in the case of metrology of resists. A stable picture sharpness, and an usable magnification with the spot size measure permit the determination of the resolution of the microscope, the spot is mainly considered circular and has a Gaussian intensity profile.

Electron imaging depends on various parameters, in addition to the type of signal which itself can be influenced by the incident beam angle, the spot size of the beam and its energy, the composition of the sample and the dimension of the scanned area which emits signal,

Through the entire range of accelerating voltages, only voltages below 1 kV offered the best SEM resolution below 1 nm, explained by the physical phenomena of electron-matter interactions, in which the electron beam which has does not have a long trajectory into the sample under lower voltages, in this condition, the spot size determines mainly the electron image resolution charging and/or beam damage free whereas the electrons accelerated under high energy, the interactions would be voluminous and deeply and the emitted signal is mainly providing rich information.

Conclusion

FIBs are widely applied for nano-fabrication: lithography, imaging, implantation. In this chapter, two dual beam stations made by Orsay Physics, were presented with internal view of FIB and SEM columns configured differently, in addition certain basic notions of how a beam of ions can be focused, and how the current density is distributed with the concept of resolution were reviewed. The development of LMIS has been the responsible of FIBs development due to their implication in various application from nanofabrication, ion implantation to ion imaging. By the apparition of LMAIS in the semiconductor field, dual-beams have known a wide success and potential with incorporated detectors for various applications and highly information rich ultrastructural images. LMAIS and LMIS sources were described with their optical properties and real experiments data using ExB mass separator for different ion mass issue from an AuGe and AuSi were illustrated. A brief description of each component of the charged particle columns was reported showing the FIB operation principle from the emitted ions to the focused beam on the target, in addition to the ion column alignment.

Ion beam lithography is a versatile technique with several variations of the process. Dual focused ion beams of Ge and Si ions have been successfully used for nanofabrication experiments and process development combining FIB lithography and dewetting or Ge condensation processes. Also, these ions were used to pattern surfaces in the ion implantation process. Combined to the FIB, SEM performs the characterization in real time of either the implanted areas or the nanopatterned objects, which offers remarkable advantages over

Transmission Electron Microscopy (TEM): no limits for the sample dimension and easy to prepare (200 mm diameter wafers, or even larger), while for TEM sample dimensions and their long preparation are limited to around 2.3 mm or 3 mm in diameter, with complex lamellae preparation that destructs sample.

References

- [1] R G Forbest. Understanding how the liquid-metal ion source works. *Vac.*, 48:85–97, 1997.
- [2] L.W. Swanson, G.A. Schwind, A.E. Bell and J.E. Brady, *J. Vat. Sci. Technol.* 16 (1979) 1864.
- [3] V. Wang, J.W. Ward and R.L. Seliger, *J. Vat. Sci. Technol.* 19 (1981) 1158.
- [4] P.D. Prewett, D.K. Jefferies and T.D. Cockhill, *Rev. Sci. Instr.* 52 (1981) 562.
- [5] N. Anazawa, R. Aihara and M. Okunuki, "10th Conf. on Electron and ion beam science and technology" (ECS, Princeton N J, 1982).
- [6] Von Ardenne M (1956) *Tabellen der Electronenphysik, Ionen-physik und Ubermikroskopie* (VEB- Deutscher Verlag der Wissenschaften, Berlin).
- [7] Hill, R. & Faridur Rahman, F.H.M., 2010. *Advances in helium ion microscopy*. Nuclear Instruments and Methods in Physics Research Section A: Accelerators, Spectrometers, Detectors and Associated Equipment.
- [8] Giannuzzi LA, Stevie FA (2005) *Introduction to Focused Ion Beams; Instrumentation, Theory, Techniques and Practice*. Springer Science + Business Media, Inc., New York, USA. pp. 3–5, ISBN: 0-387-23116-1.
- [9] Taniguchi N (1989) Chapter 1. in Taniguchi N, Ikeda M, Miyamoto I, Miyazaki T, (Eds.) *Energy Beam Processing of Materials*. Oxford University Press, p. 38. ISBN: 0198590059.
- [10] Buchholz B, *Physics of Ion Beam Sources*, Internal Publication of Plasma Process Group, Inc., Loveland, CO, USA, 2009, accessed at www.plasmaprocessgroup.com/itemdocs/tech/Ion_Beam_101.pdf.
- [11] Trassl R (2002) *Development of ECR Ion Sources*, Institut fu" r Atom- und Moleku"lphysik, Universita"t Giessen, Germany, accessed at <http://www.strz.uni-giessen.de/Fezr/english/prinzip.html>.
- [12] Gailly P, Collette J-P, Renson L, Tock JP (1999) *Ion Beam Figuring of Small BK7 and Zerodur Optics: Thermal Effects*. *Proceedings of the SPIE* 3739:124–131.
- [13] Orloff J, Utlaut M, and Swanson L, *High Resolution Focused Ion Beams: FIB and Its Applications*, Kluwer Academic/Plenum Publishers, NY (2003).
- [14] Henry, M.D. et al., 2010. Ga+ beam lithography for nanoscale silicon reactive ion etching. *Nanotechnology*, 21(24).
- [15] R. Levi-Setti, T.R. Fox and K. Lam, *SPIE* 333 (1982) 158.
- [16] Orloff J, *Handbook of Charged Particle Optics*, CRC Press, Boca Raton (1997).

III. Nanofabrication with FIB and results

Introduction

The local doping of semiconductors can be a relevant application of FIB implantation, with the development of new alloy sources that provide the emission of both singly and doubly charged ions. For the latter, the energy of implantation is doubled with species such as Si, B, C, In, As and Be that are the main dopants of various semiconductors.

The focused ion beam implantation, which is a maskless process, offers the capability to vary the dose from point to point on the selected area of the sample surface or wafer. Preliminary it has to be established that implantation of a given dose by a focused ion beam is identical to conventional implantation, since the current density in a focused ion beam is several orders of magnitude larger than the current density of a conventional implanter.

Due to its particularity to accommodate a large number of different colour centers, that give access to a large spectral range and variety of different spin and optical properties, Diamond is used in a large set of applications such as luminescent markers [1], magnetic field sensing with high spatial resolution [2] or as single photon emitter in quantum optics applications [3, 4]. Although the most studied colour center is the negatively charged nitrogen-vacancy centre (NV^-) that has a unique set of properties and applications [5], new colour centers in diamond are increasingly attractive so several researches are dedicated to find colour centers with improved spin and optical properties. There is a variety of emission of single photons that have been demonstrated with Cr-based colour centers [6] and Ni-based centers (NE8) [7], but their engineering is difficult. However, a critical resource for quantum optical communication are systems based on nitrogen [1, 3], silicon [4], carbon [5] impurities since they have been shown to generate non-classical states of light and emit single photons at room temperature.

In this scientific research context, the objective of our study is to create SiV and GeV colour centers in diamond (anvil and flat diamond substrate) samples using FIB ion implantation and annealing treatment.

III.1. Ion implantation

III.1.1. Implantation of SiV and GeV in Diamond

This work is part of a collaboration with the Aimé Cotton Laboratory in Paris, basically consists of creating SiV and GeV centers in diamond anvils by the implantation of Si and Ge ions. The SiV/GeV centers were then annealed at high temperature for activation of the defects and characterised by PL spectroscopy.

III.1.1.1. Implantation of Si into diamond

Firstly, I implanted the Si ions in squares and circles of 2 μm and 3 μm in length and/or diameter respectively, spaced by a distance of 5 μm , and changing the dose from one pattern to another in a predefined direction; starting with the low dose of E^{+9} Si/cm² to the high dose of E^{+15} Si/cm². Such doses are expected to avoid the diamond anvil charging effect. The ions have two different charges (Si⁺/Si²⁺ and Ge⁺/Ge²⁺) and they are implanted at two different accelerated energies (15 keV and 30 keV) with variable doses. Implantation areas have the shape of squares and circles with predefined dimensions given by the Aimé Cotton team (Figure 3.1),

The optical and electrical implantation parameters that allow the dose to vary from low to high values are the following: I used currents from a few picoamperes to a few femtoamperes. I also used the de-focusing of the ion beam, by modifying the excitation the objective lens, which produces a variation of the width of the beam size, this is the compromise found as a result of the minimum etching time limitation per pixel fixed by the station electronics, which cannot be modified and which was 42 ns for the squares and 21 ns for the circles.

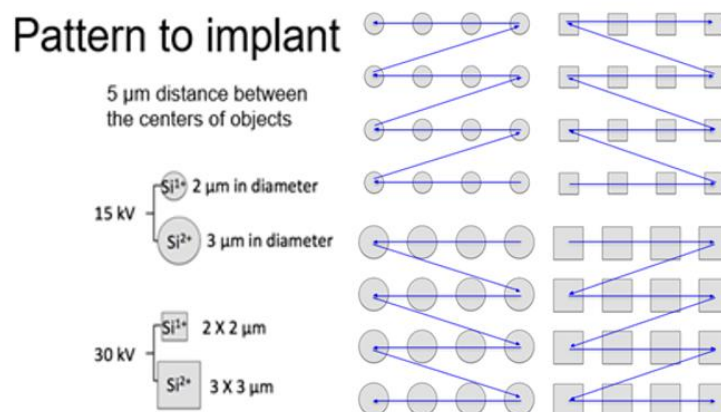


Figure 3.1. Schematic representation of the patterns dimensions to be implanted in diamond and the increase of doses is indicated with blue arrows.

To avoid possible contamination related to charging, smallest doses for all four conditions should be always in the center of the total pattern.

Our experiments are performed using AuSi LMAIS source, which emits Si ions, with the optical alignment of the FIB column to prepare the specific settings dedicated to this implantation; primary based on low current of 280 fA to 1 pA, depending on the energy and on the single or double charged ions, then the increasing doses start from $E^{+9} \text{ Si/cm}^2$ to $E^{+15} \text{ Si/cm}^2$.

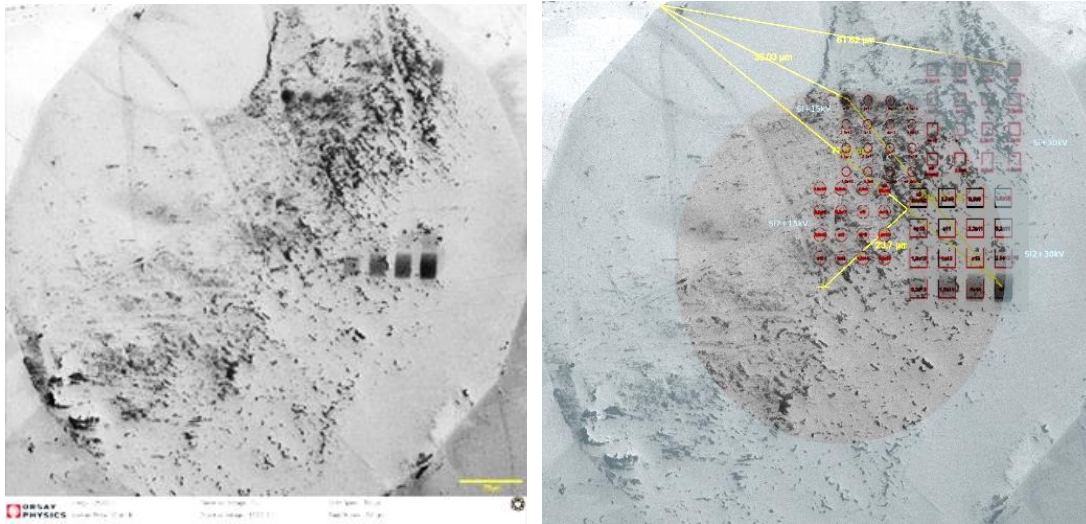


Figure 3.2. SEM observation at 25 keV energy of the Si patterns implanted in the diamond anvil1957 with the FIB filtered column.

Implantations areas have been observed by SEM (figure 3.2). On this series of implantations, we can see that the patterns are not well positioned in relation to the centre of the diamond capsule, and that the patterns are not well positioned in relation to each other. This is due on the one hand to the FOV (Field Of View) of the FIB filtered column lens which was not well calibrated at the energies used, and on the other hand to the FOV of the SEM column, despite the good coincidence between the two FIB columns. And to the FOV field of view of the SEM column on the other side, despite the good coincidence between the two FIB and SEM columns. This experiment shows a large shift of the FOV of the ion column when changing the energy from 30 keV to 15 keV.

This experiment gives a good measure of the shift and helps to recalibrate the FOV of the two columns FIB and SEM under different energies. In order to position the patterns correctly, I worked on developing a script to eliminate the shift due to the energy change. Then the good coincidence between the two columns of FIB and SEM allows to know the focus of the objective lens of the SEM which is used as reference during all the diamond implantation. The

use of SEM has two advantages: first to keep the optimizations made on the FIB conditions and second to avoid the ionic imaging (which would induce the implantation on unintended areas) using only non-destructive electronic imaging. Once all these optimizations are done, I performed implantation tests on several samples such as Si bulk, SOI (for Silicon On Insulator) and SGOI (for Silicon Germanium On Silicon On Insulator) before moving on to diamond samples. Figure 3.3 shows the Si patterns implanted in the flat diamond sample (which has a length of 2 mm, and a thickness of 500 μm). From the in-situ SEM observation, one can clearly see the good positioning of the patterns attesting that the FOV calibrations of the two columns were correctly modified, as well as the shift due to energy (via the script).

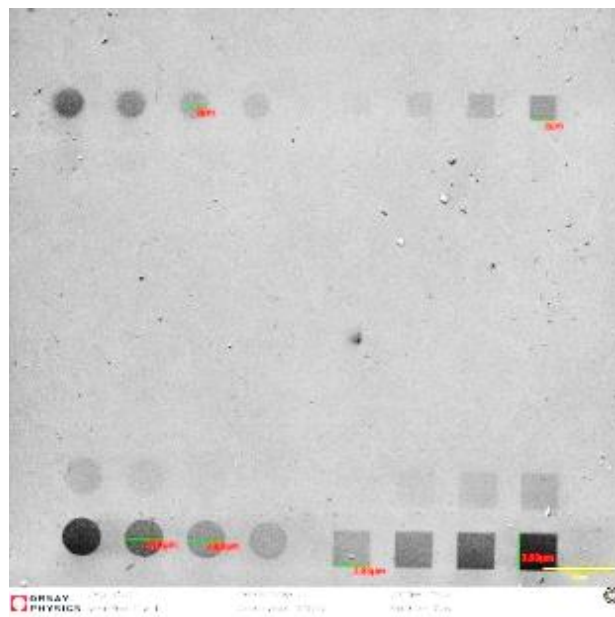


Figure 3.3. SEM observation at 25 keV energy of the patterns implanted with Si ions in the flat diamond sample with the FIB filtered column.

This work has allowed us to further optimise the limits of the filtered column and to improve its ergonomics in the field of implementation with the use of scripts adaptable for future experiments, and to further develop these scripts and the software in such a way as to be able to introduce several actions and commands at the same time in order to facilitate the piloting of the sample through the script as well as the loading of the ionic conditions in an automatic way (contrary to previous experiments for which I did everything manually).

These samples were then annealed at 900 °C for 2 hours for the activation of defects, before they were characterised by Photoluminescence (PL) spectroscopy in the Aimé Cotton Laboratory (LAC). From the spectra obtained by the collaborators, it was found that the best implantation conditions were those performed at high energy (30 keV) and with a dose of $E^{+14} \text{Si/cm}^2$. Si^{2+} ions also give better SiV emission efficiencies, when compared to Si^+ ions. The

spectra of the PL emission intensity of the SiV centers as a function of dose and energy of the implantations are presented in figure 3.4 on the left and right respectively. Since these PL characterisations were time consuming for the LAC team, following the installation of a new PL microscope and its commissioning and calibration of the annealing conditions, we received the information quite late.

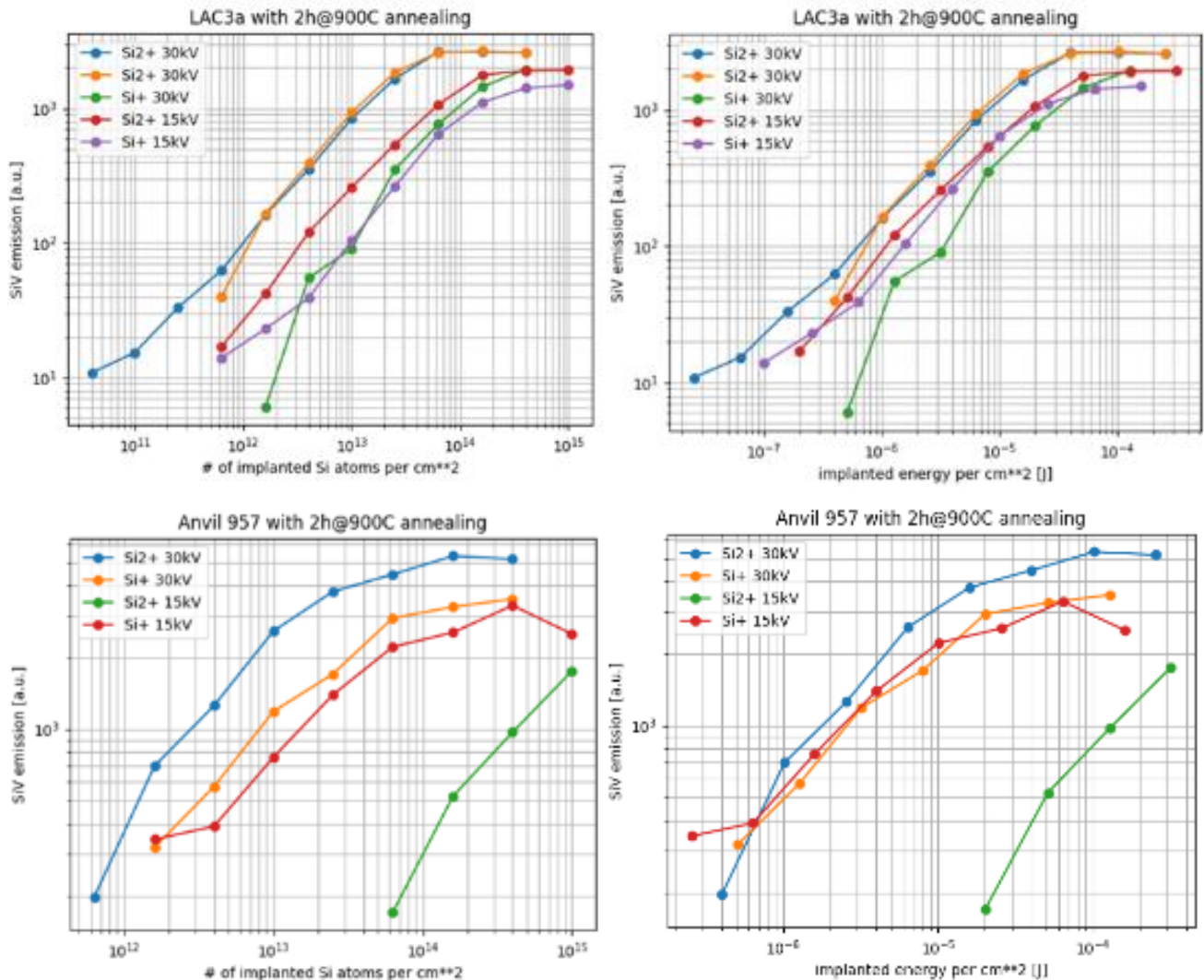


Figure 3.4. PL Emission spectra of SiV centers for implantations at 30 keV and 15 keV, using Si⁺ and Si²⁺ ions and as a function of: (left) Si ion implantation dose and (right) energy. Implantations have been performed in: (top) the diamond flat sample (LAC3a) and (bottom) the diamond anvil (Anvil 957)

From these preliminary PL results and those carried at low temperature, it was decided to repeat the implantations with the optimal conditions; i.e., implanting with Si²⁺ ions, in the form of 2 μm stop squares in the center of the anvil, accelerated under an energy of 30 keV and at a high dose $\sim 10^{14}$ of Si/cm². The SEM observations (Figure 3.5) exhibits the implanted areas in Anvil957.

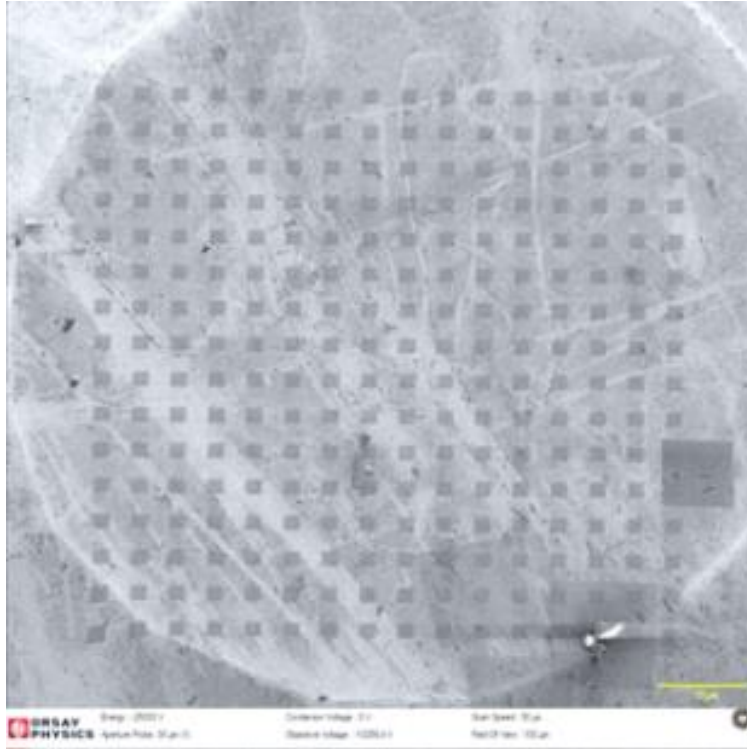


Figure 3.5. SEM observation at 25 keV energy of the patterns implanted with Si ions in the flat diamond sample with the FIB filtered column.

Unfortunately for our study we could not continue on this Si implanted anvil since it was broken by the LAC team, during the low-pressure tests that was requested to obtain the finest PL pic of SiV centers (as already reported in the literature).

III.1.1.2. Implantation of Ge in diamond

In a second series of experiments, I have also implanted Ge ions using the minority isotopes of $^{76}\text{Ge}^{2+}$ and $^{70}\text{Ge}^{+}$ at 30 keV and 15 keV a new diamond anvil (Figure 3.6). The AuGe LMAIS source mounted in a filtered ion column in the LYRA dual-beam system of the NOVA team (IM2NP) was used. The implanted areas had the same geometries (series of squares and circles) and the same dimensions as those implanted with Si ions using the Nanospace platform. Unfortunately, since more than one year, no PL characterizations came back from the LAC team.

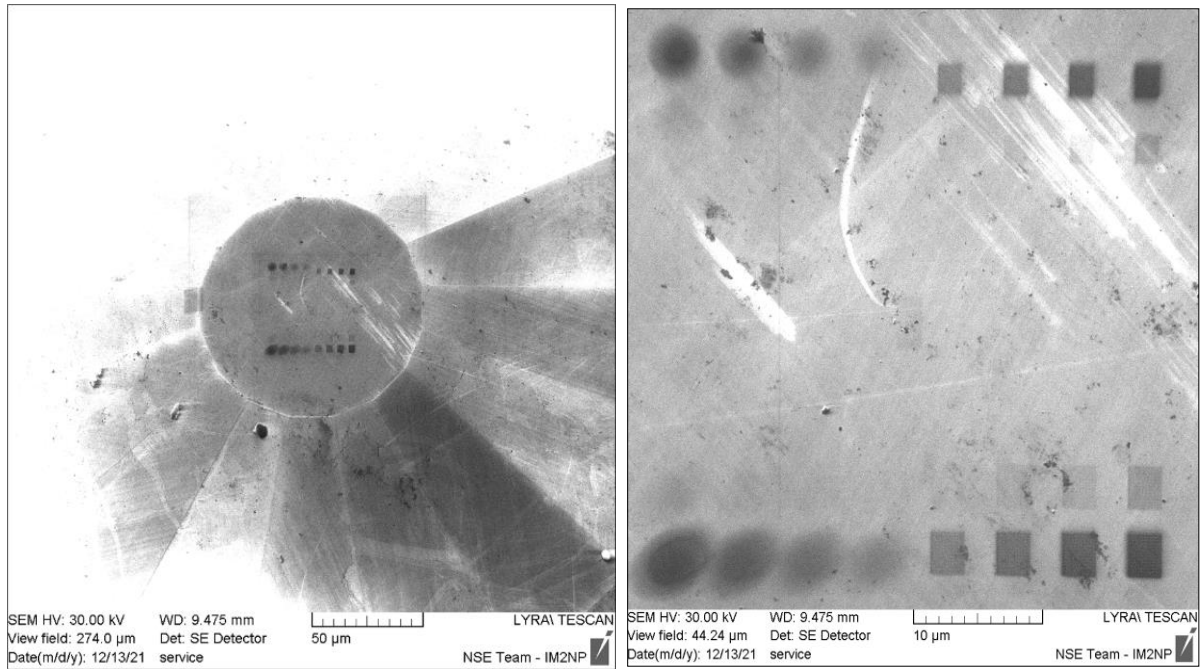


Figure 3.6. SEM observation at 30 keV energy of the patterns implanted with Ge ions accelerated to 30 keV and 15 KeV in the diamond anvil with the FIB filtered column of the LYRA station.

These samples were supposed to undergo a thermal treatment before the PL characterization at room and low temperature and at low pressure (coll. LAC). The aim was to compare the implantations with the two ions (Si and Ge) and their efficiency in the creation of SiV and GeV limited-lifetime emitters in diamond.

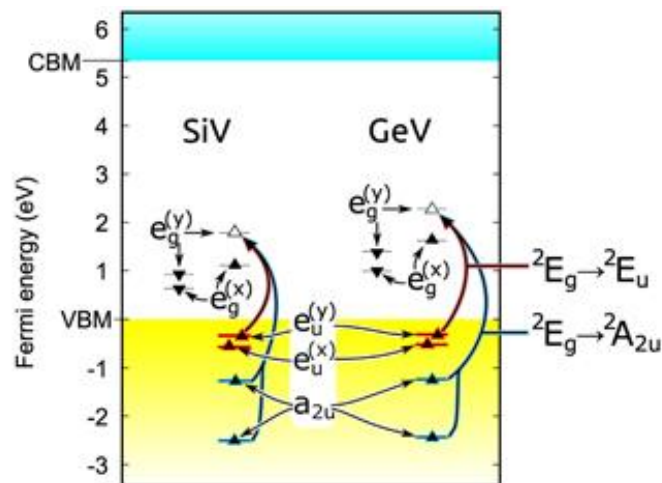


Figure 3.7. Electronic configuration for the ground state (2E_g) as calculated by HSE06 functional in a 512-atom supercell.

A schema of the excitation states at the origin of photon emission is given in Figure 3.7. The energy of the valence band maximum is aligned to 0eV. The optical transition associated with

the first excited state (2E_u) and the second excited state (${}^2A_{2u}$) are depicted by red and blue inclined arrows, respectively. The 2E_u Kohn–Sham state is getting localized when a hole is induced on it according to constraint DFT calculations (see also [29]). This does not hold for (A_{2u}) bands.[30].

The SiV and GeV have a great importance in quantum technology. It was reported that SiV centers have unique set of optical properties [8] such as a comparably large Debye–Waller (DW) factor of ~ 0.7 , a single photon emission with good polarization contrast [9], a very small inhomogeneous line broadening [10]. GeV centers are expected to offer a very similar structure than that of SiV [12]. A zero-phonon line (ZPL) emission at 602.5nm with a full width at half maximum (FWHM) of 4.5nm was measured experimentally at room temperature in high-pressure-high-temperature (HPHT) synthesized diamond crystals [13, 14].

III.1.2. Implantation of SiV in UT- ${}^{28}\text{Si}$ using ${}^{28}\text{Si}^+$

Another way to create photon emitters is to implant ${}^{28}\text{Si}^+$ ions by FIB in ${}^{28}\text{Si}$ Silicon On Insulator (${}^{28}\text{Si}$ SOI) (Figure 3.8). I then worked on the ion implantations of several samples of Ultra Thin-Silicon On Insulator (UT-SOI), but with a more accentuated filtering to get an isotopic dissociation of Si ions (${}^{28}\text{Si}^+$). For this purpose, I first separated the Si isotopes with the Wien Filter: ${}^{28}\text{Si}^+$, ${}^{29}\text{Si}^+$ and ${}^{30}\text{Si}^+$ at 30 keV energy. Isotope dissociation at 15 keV and 20 keV was impossible due to the limitations of Nanospace prototype. A previous study performed the simulation using the SIMIO software to optimise the Nanospace dissociations of all chemical species at low energy in the perspective of increasing the panel of the FIB filtered column and widening its use in optoelectronic applications.

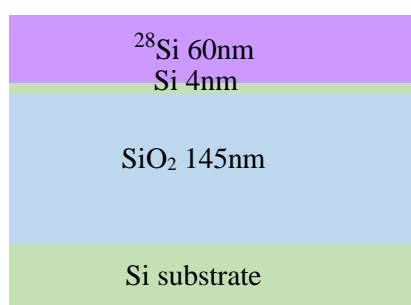


Figure 3.8. Cross section view of ${}^{28}\text{Si}$ SOI ultra-thin sample supplied by CEA.

Concerning the design, I performed square arrays of patterns with $10\mu\text{m} \times 10\mu\text{m}$ size and spaced $3\mu\text{m}$ apart. Again, the dose and ion beam de-focusing were varied from one line to another as presented previously. On the other hand, I also varied the dimensions into the limitations of the Nanospace station. I used again a script to position each matrix well in the set (Figure 3.9). Time was spent to optimize the position of the patterns and the setting of the stage

offset along the X and Y axis when going from one line to another (because of the software problems).

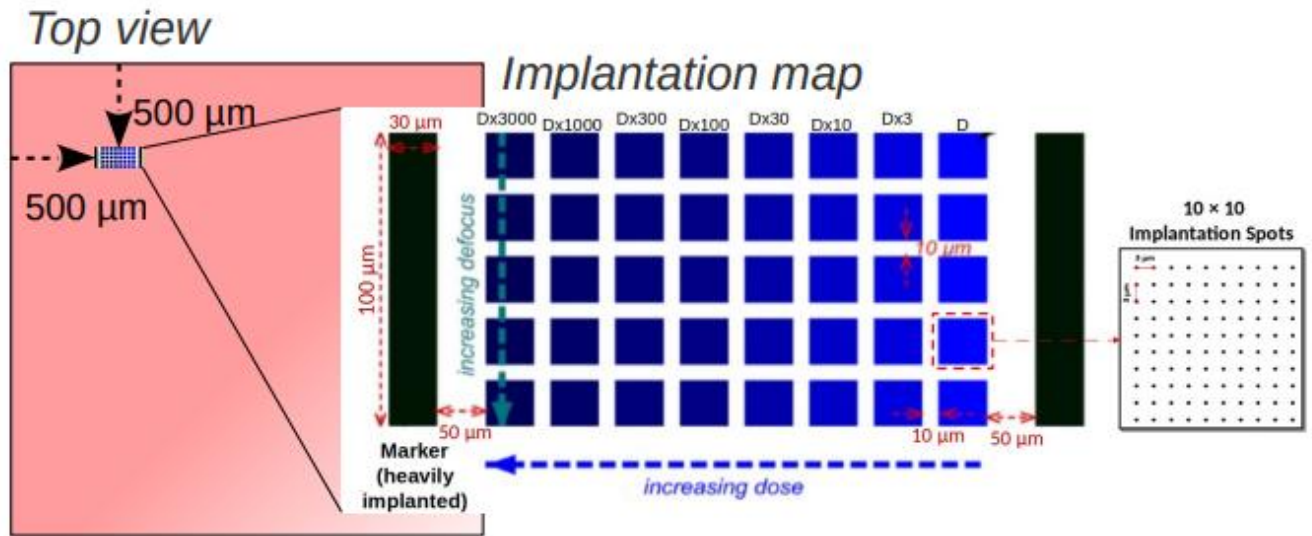


Figure 3.9. Diagram of the sketch of implantation of the $^{28}\text{Si}^+$ in the UT-SOI with the Nanospace FIB filtered column at 30 keV. The variation of the dose in the X-axis is indicated by the blue colour code. De-focusing is varied in the Y-axis.

Once implanted, the samples were annealed in the RTO (Rapid Thermal Oxidation) at 900°C, for both recrystallisation and defects activation. They were the characterised by PL in L2C in Montpellier. Several defects were detected but not the SiV centers. Some examples of PL cartographies are given in Figure 3.10, 3.11, 3.12.

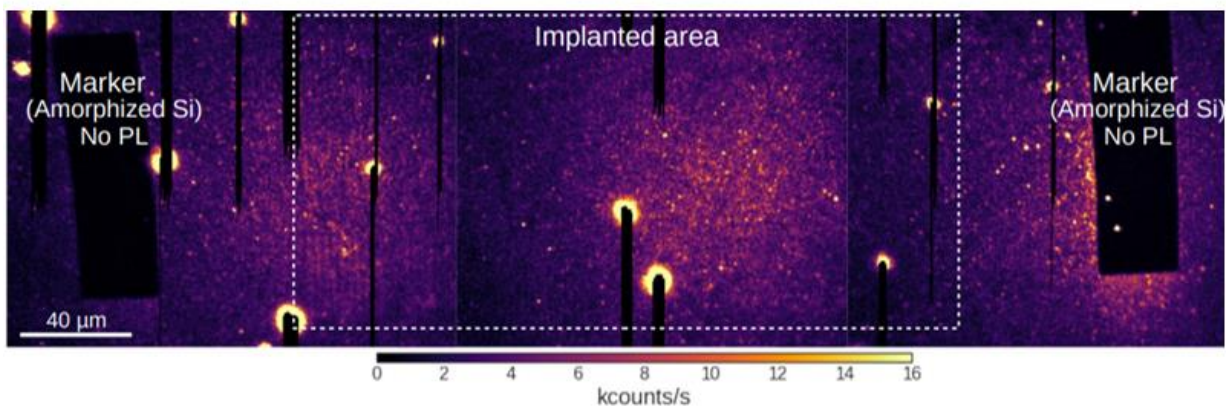


Figure 3.10. PL cartography of the implanted areas using a green (532-nm) laser excitation, with an optical power $P=10 \mu\text{W}$, using only a FELH1050 filter & at a temperature ($T=30 \text{ K}$).

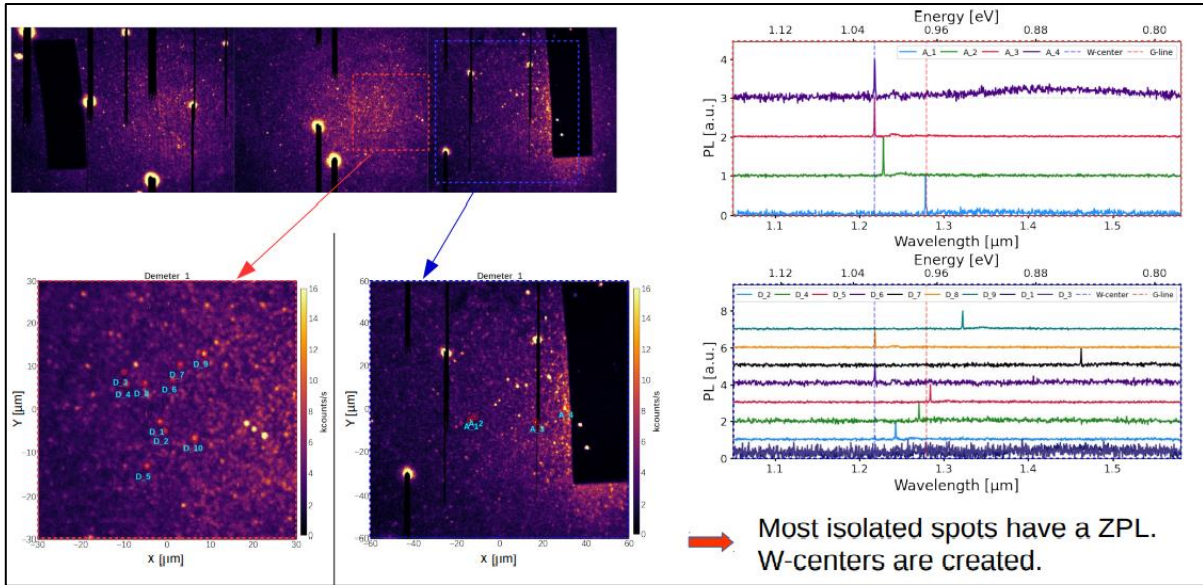


Figure 3.11. PL spectra of the W-centers created from FIB implantation of $^{28}\text{Si}^+$ in ^{28}SOI .

It can be seen that the fluorescent defects are randomly distributed spatially and do not correspond to the patterned areas (Figure 3.10). The bright spots are only dust (Figure 3.10). The dark lines correspond to an artefact, due to a switching of the superconducting detector to normal metal phase due to high contrast. We could detect the creation of intrinsic defects in silicon, which are linked to a tri-interstitial complex called the W-center (Figure 3.11). The defects have a very broad PL band (Figure 3.12).

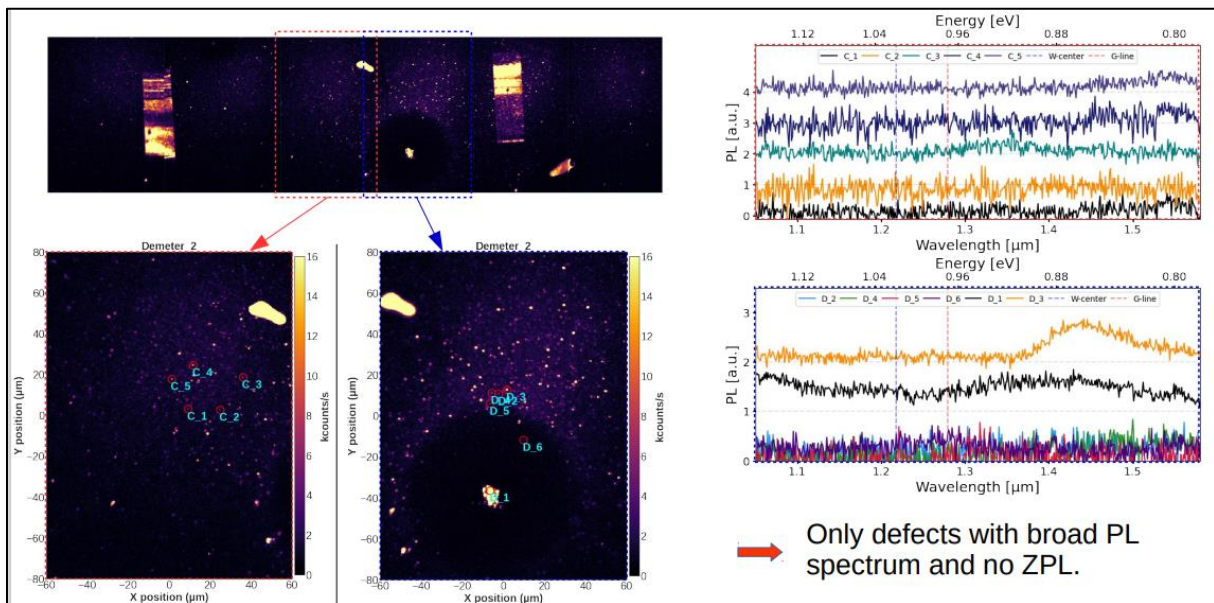


Figure 3.12. PL spectra of the detected defects generated from FIB implantation with $^{28}\text{Si}^+$ in ^{28}SOI .

On both samples, the ion implanted areas could not be observed. Among all the isolated spots randomly distributed spatially on the implanted areas, a large number of W defects were identified in the sample without annealing.

III.2. Nanopatterning with Ge ions

In this section, we present the self-organisation of Si and Ge quantum dots formed by combining FIB lithography and RTO dewetting processes. The aim of this work is to form high density of ultra-small Ge and Si nanocrystals. For this study the interest in the FIB is its high resolution which should allow a very spacing between the nanopatterns. Another critical point, is the depth resolution which should be of the order of a few nanometers, well below the 20nm thickness of the SiGe layer in epitaxy on SOI (Figure 3.13).

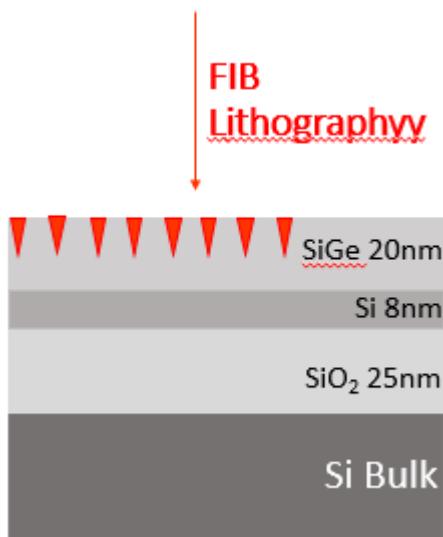


Figure 3.13. Cross section view of SGOI stacking layers that consist of SiGe on top in epitaxy on Silicon On Insulator, on Si(001) substrate .

In a first step, I started the experiments using Ge ions from the AuGe source. To obtain the highest resolution, it is mandatory to prepare the FIB settings: mechanical and optical alignment and isotopic discrimination of the Au and Ge chemical species, then choosing small apertures size (10 μm and 20 μm) for the best filtering of Ge isotopes even single or double charged: ^{76}Ge , ^{74}Ge , ^{73}Ge , ^{72}Ge and ^{70}Ge with the creation of dedicated ionic conditions for nanopatterning experiments with a compromise between the different patterns configurations and the beam parameters (i.e. low current and low dose). The number of scans and the time per pixel (0.8 μs) were also reduced. Not only the current and the beam size come into play in the etching but also the etching rate of the substrate should be determined. It is why I calibrated it using the isotope to be used ($^{74}\text{Ge}^{2+}$) and the SGOI samples. Even if these samples consist of 20 nm thick Si_{0.8}Ge_{0.2} layer epitaxially deposited on 8 nm thick Si layer itself on 25 nm SiO₂

layer on Si(001), I was only interested in the milling of the top surface layer of the SiGe film. To achieve this objective, I carried out a series of calibration tests with Ge with different doses with an ion beam diameter of 50 nm and with low and high currents. The idea is always optimise the current, the number of beam scans per pixel, the dot coverage rate during etching, the etching rate and the exposure step between spots. The aim is to get a rather shallow depth of between about 2 to 5 nm in the SiGe top layer.

The first geometries consist of series of parallel lines of different depths and pitches. The depth is changed from 1 to 10nm and the pitch from 100 nm to 200 nm, 280 nm, 300 nm, 500 nm, 750 nm and 1.2 μm . The table below shows the optimal etch depths characterised by AFM using a spot size of 50 nm and a sample current of 23 pA:

Dwell Time	1 μs	2 μs	3 μs	5 μs	6 μs	7 μs	32 μs
Nombre de scan 1000							
Profondeur de gravure (nm)	600 pm - 0.75 nm	1-2	2-5	3 - 6	3 - 6	8 - 10	

Table 3.2. Summary of etch depths at 30 keV with $^{74}\text{Ge}^{2+}$ ions.

The deepest depths were performed with exposure times of 32 μs at 30 keV. As a result of the cascades of collisions of the ion beam with the substrate, defects and amorphisation are created which potential change of the chemical properties. The shallow depths were obtained at low currents and very short etching times (160 ms). At low current, the interactions between the ions and the substrate take place at the top surface, as shown by AFM scan profiles (Figure 3.14).

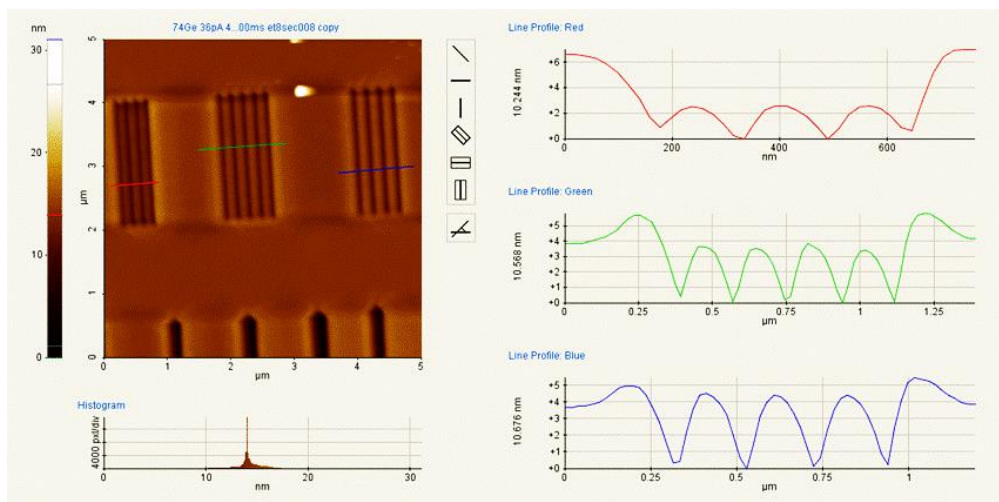


Figure 3.14. AFM characterisation of patterns of paralleled lines with increasing pitches milled by FIB with $^{74}\text{Ge}^{2+}$ ions accelerated under 30 keV.

After the FIB milling calibration, I calibrated the condensation by RTO using SGOI samples (20% of Ge) with ^{74}Ge ions. Before the condensation, the samples are characterised by AFM. Condensation is performed at $750\text{ }^\circ\text{C}$ for 4, 5 and 6 hours. The aim is to determine the evolution of condensation and of dewetting with the duration of the oxidation which is related to the formation of the Ge nanocrystals when Ge is totally dewetted inside the oxide. The study should also determine the sizes of the Ge NCs and their position. Concerning the condensation, it is necessary to know if the Si layers have been consumed by oxidation to get a pure Ge layer embedded in the SiO_2 . Cross-section TEM imaging is used to get this information.

For all the samples, the SiO_2 was etched in an aqueous solution with HF. Subsequently, SEM characterisations were carried out with a TECNAI microscope (CP2M). The first sample, which was oxidised for 4 hours at $750\text{ }^\circ\text{C}$, is shown in Figure 3.15.

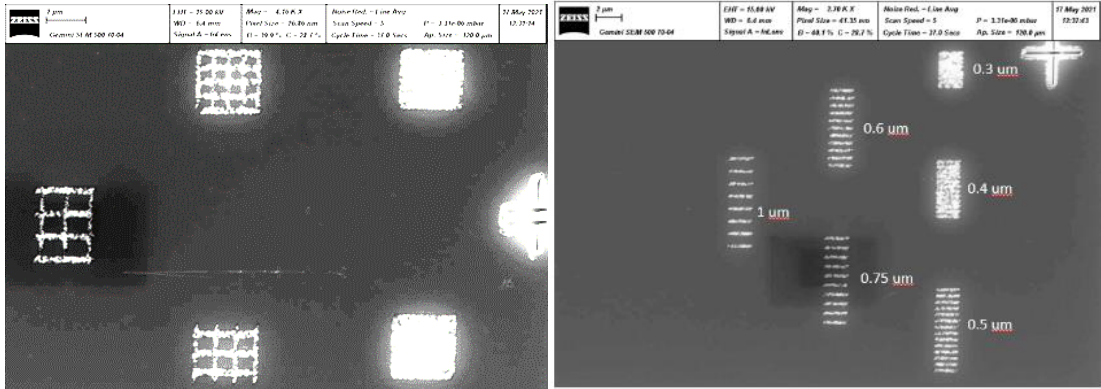


Figure 3.15 SEM observation of parallel lines and squares etched with $^{74}\text{Ge}^{2+}$ under 30 keV in SGOI.

Unfortunately, for this sample, there was a mistake during the FIB preparation of the lamellae and the desired areas were etched. TEM did not allow to visualise the patterns.

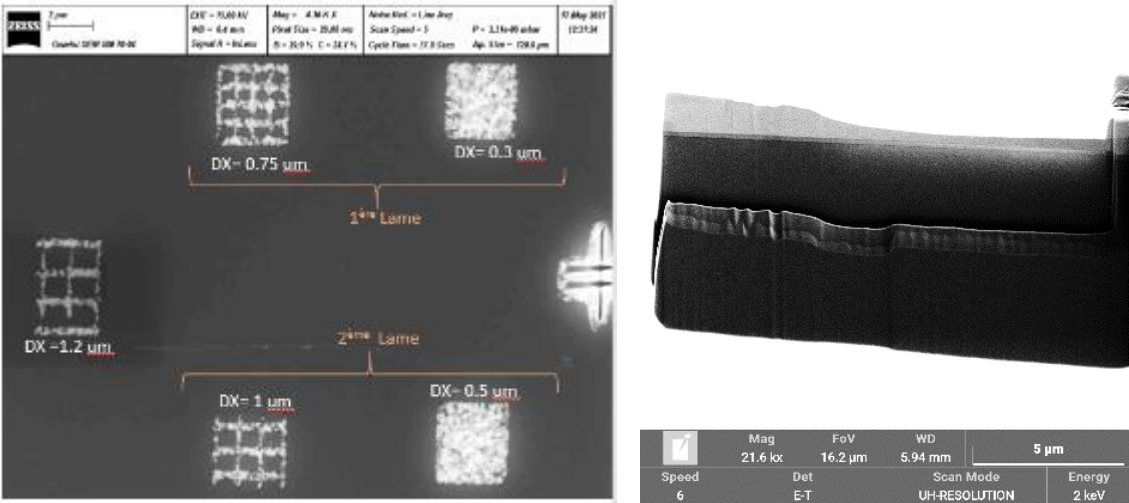


Figure 3.16. Preparation of two slides for TEM observation of $^{74}\text{Ge}^{2+}$ etched patterns.

The two other samples were oxidised during 5h and 6h. The SEM characterization is shown on figure 3.17. The formation of NCs is clearly visible on the image for both oxidation durations with different sizes depending on the depth/pitch of the lines made by FIB. We show here an example of Ge NCs with ~100nm diameter, spaced of ~300nm.

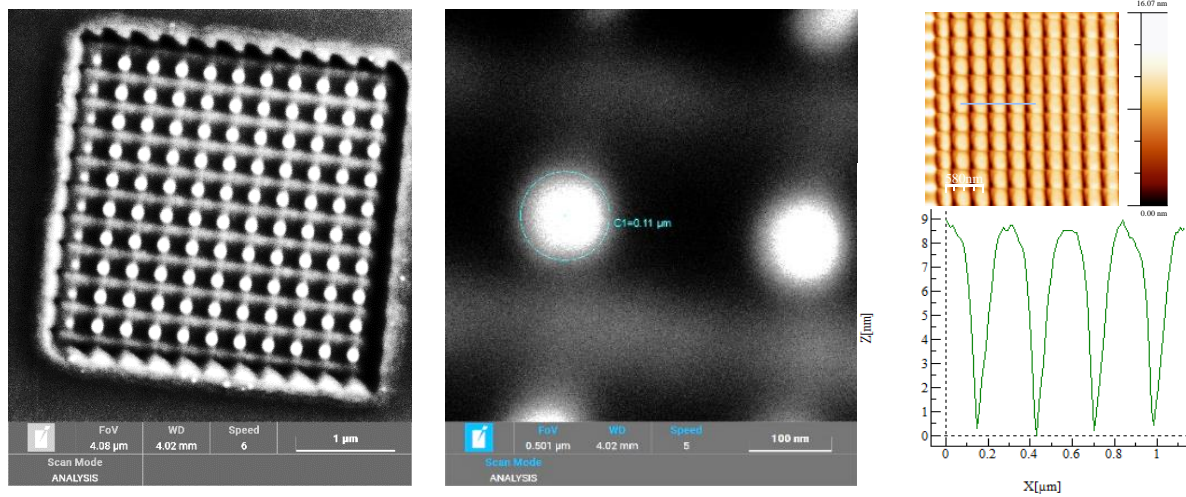


Figure 3.17 SEM image of 100nm large Ge NCs obtained by FIB nanopatterning/ condensation of the SGOI sample using $^{74}\text{Ge}^{2+}$ under 30 keV (Lyra station). AFM images show that the depth of the patterns is ~9 nm and the pitch ~300nm. Condensation was performed at 750 °C for 6 hours in the RTO.

This illustration demonstrates the elaboration of Ge nanocrystals by coupling direct FIB lithography with Ge condensation in RTO. The nano-objects formed have a mean size of 100 nm +/- 20 nm, which is a function of the pitch of the patterns.

Several questions currently arise about the structure and composition of the NCs. Unfortunately, TEM cross-section did not allow to answer the questions, since the FIB cross-section was not exactly positioned on the dots (Figure 3.18).

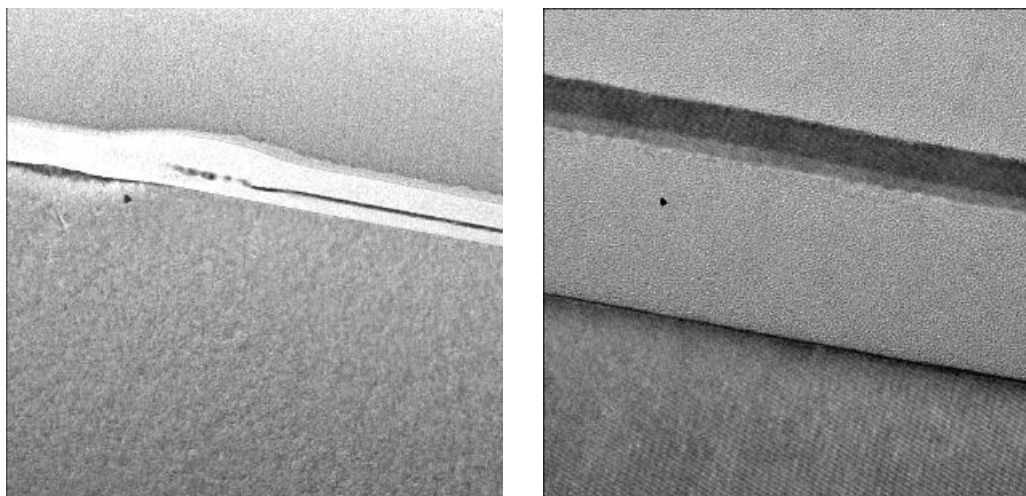


Figure 3.18. Cross-section TEM observation of the sample after condensation/oxidation in the RTO. Ge NCs cannot be observed.

The TEM observations made on these patterns do not show the Ge nanocrystals because of the polishing steps, we lost the quantum dots during this step and we were observing the areas between the NCs. Besides, it can be seen on the unpatterned areas, that the condensation is not complete and that there is still a sub-Si layer (that remains from the SOI) and a Ge-rich SiGe layer. However, since the condensation kinetics is much more rapid on the patterned areas, may be on these areas there was the formation of pure Ge (not confirmed by TEM).

In order to have a Ge-rich layer, further condensation is required to consume the remaining Si from the SOI as well as the Ge-rich SiGe layer. Furthermore, TEM observations show that for high doses patterning, the defects created by Ge implantation during the FIB pre-patterning step have pushed the Ge into the Si substrate. For this reason, it is necessary to reduce the FIB doses to minimize the defects created and avoid damaging the complete SiGe/SOI layer.

Another alternative that has been investigated is to etch parallel lines with Ge and Au ions in the SGOI. The pitch between the lines was varied from 100 nm to 320 nm. This was expected to facilitate the preparation of TEM lamellae and to favour the NCs self-organisation without damaging neither the substrate, nor the residual Ge.

A wide range of patterns were performed with different settings in order to get low depth. The problem of this study is the characterization of the samples which is extremely time consuming since it should be done by TEM cross-section. From TEM observations, only very low dwell time, down to 5 μ s was sufficiently small to achieve the total condensation, and get the Ge NCs.

III.3. Ge Condensation process

Before presenting the condensation of SGOI samples patterned with FIB, a brief presentation of thermal oxidation of Si and the soft SGOI samples condensation process, these samples consist of SiGe in epitaxy on SOI itself on Si(001). SiGe contains a 20% of Ge, and a thickness about 20nm. Low thickness/concentration allow to avoid relaxation and the nucleation of dislocations during the epitaxy process.

III.3.1. Thermal oxidation of Si

In order to understand the oxidation process, it is necessary to know the physical and chemical mechanisms that govern this reaction. In the case of silicon oxidation, an insulating film of SiO₂ is formed on the surface of the silicon. We can already distinguish two main types of thermal oxidation: dry oxidation where the oxidising agent is molecular oxygen and wet oxidation

where the oxidising agent is water vapour. We are interested in dry oxidation. Since the newly formed SiO_2 separates the two reagents (Si and O_2), there must be first diffusion of O_2 through the oxide layer so that in a second stage the chemical reaction could produce SiO_2 . Figure 3.19 illustrates the process of silicon oxidation showing the different parts of reaction and diffusion. It is well established that it is the oxidising agent that is the diffusing species and that the reaction forming SiO_2 takes place at the Si/SiO_2 interface. However, the details of the diffusion processes, the phenomena involved in the interface reaction and the nature of the oxide formed cannot be detailed here.

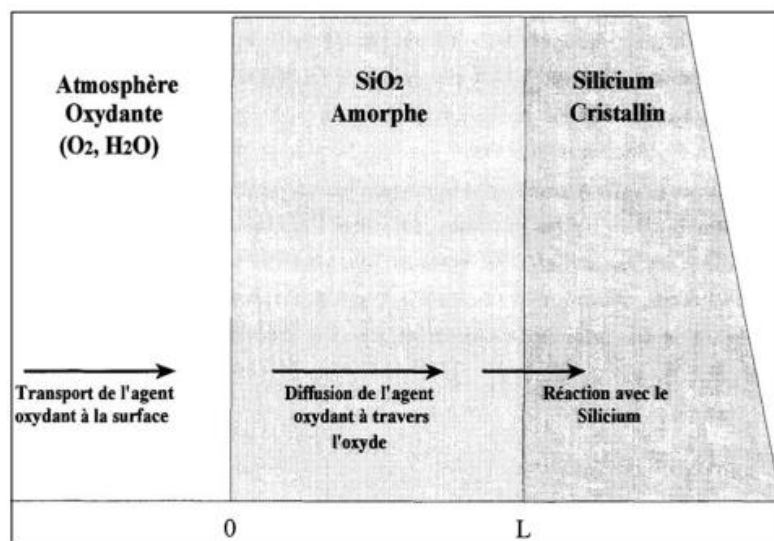


Figure 3.19. Schematic representation of the chronological oxidation steps of a silicon crystal: Transport, diffusion and reaction

Characterising the diffusion process involves not only identifying which reactant is diffusing but also determining how the diffusing species interacts with the SiO_2 lattice and what charges the oxidising species have. Results using oxygen isotope 18 as a tracer of the oxidation process, showed that this process was strongly dominated by the migration of molecular oxygen through the SiO_2 lattice without exchange of atomic oxygen with the SiO_2 molecules already formed. The overall understanding of the silicon oxidation process requires the characterisation of the interface reaction. This interface reaction actually groups together several sub-reactions. Firstly, the molecule of oxidising agent (O_2) comes near the Si/SiO_2 interface in order to obtain an oxygen atom that can react with the silicon of the substrate. However, as the substrate is in crystal form, the four valence electrons of a silicon atom form covalent bonds with other silicon atoms. These Si-Si bonds must be broken to form new bonds with the oxygen. Once these two conditions are met, the oxidation reaction can take place. Under given conditions the interface

reaction is determined by the slowest reaction. Of these three reactions, only the formation of a Si - O bond is exothermic. The interface reaction will therefore be limited either by the breaking of the Si - Si bonds or by the breaking of the oxidising agent molecules. Thus, the thermal oxidation process of silicon involves diffusion of the oxidising agent through the oxide layer already formed oxidation at the SiO₂ oxide/substrate interface between the oxidising agent and the silicon crystal. Depending on the experimental conditions of the oxidation (temperature, pressure, oxidation time and thickness of oxide, etc.), it is one of these two phenomena that will limit the oxidation kinetics. In 1965, Deal and Grove [29] proposed an equation for the oxidation of silicon taking into account all the phenomena known at that time. This model considers that any oxidation reaction is governed by three basic physico-chemical mechanisms: (i) the migration of oxidising agents from the carrier gas to the SiO₂ surface; (ii) the diffusion of these oxidising agents into the silica towards the Si/SiO₂ interface; (iii) the reaction with the silicon surface and the formation of SiO₂.

To sum up, oxidation initially occurs very rapidly (as long as the oxide formed is very thin) and is then slowed down by the increasing thickness of oxide that the oxygen must pass through before reacting with the silicon. It is therefore generally considered that in the first stages the oxide thickness varies linearly with time, and in a second regime the oxide varies linearly with the square root of time (Deal and Grove model). Because D_{Si} through SiO₂ is infinitely smaller than D_{O_2} through SiO₂, the mechanism limiting is the diffusion of oxygen through the SiO₂.

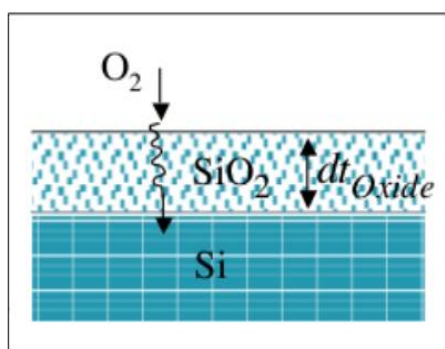


Figure 3.20 Representation of the O₂ diffusion mechanism through SiO₂

III.3.2. Thermal Oxidation of Si_{1-x}G_x in RTP

For SiGe alloys the mechanism is the same: formation of thermal SiO₂ oxide on the SiGe surface, which is energetically more favourable compared to germanium dioxide germanium dioxide (-8.2 eV and -4.7 eV respectively). The Si concentration in the remaining SiGe layer decreases progressively during oxidation; conversely, the concentration of germanium

increases (Figure 3.20). This selective oxidation process is called condensation. It allows the formation of Ge-rich layers from SiGe layers with low initial proportion (10 - 20%). With this method, and at low temperatures (in the range of 700-850°C), a Ge-rich layer with an abrupt interface with the underlying SiGe nominal film is obtained. Conversely, at high temperatures, a strong inter diffusion of Ge and Si in the crystal (SiGe and Si) induces the intermixing of the species and the formation of a SiGe layer with homogeneous concentration.

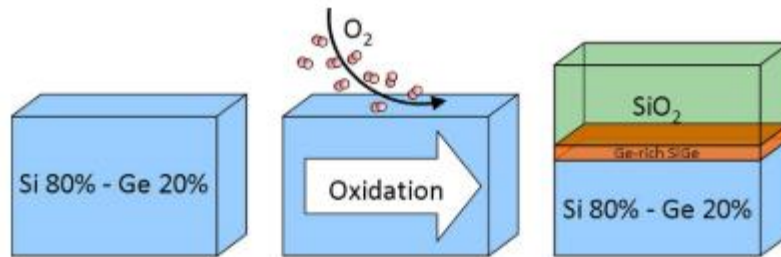


Figure 3.21. Ge condensation obtained by selective oxidation of Si and repulsion of Ge towards the SiGe/SOI interface [27].

✚ Measurement of SiO₂ thickness layer

After the oxidation which enriches the SiGe underlying layer with Ge and to keep the oxidation time reasonably short, we must therefore have a minimum of Si to oxidise, so we place an ultra-thin SOI (8nm thick). If we consider that Ge is not oxidised at all during the oxidation [28], we expect to end up with a 4nm of Pure Ge (8nm of SiGe-50%):

$$t_{Ge_pur_equiv} = t_{SiGe_initial} * C_{Ge_initial} = 20 * 0.2 = 4 \text{ nm}$$

Indeed, as Ge is conserved during the process, one can note " $t_{Ge_pur_equiv}$ " the equivalent thickness of a pure germanium layer containing all the germanium in our structure, $t_{SiGe_initial}$ is the thickness of the initial SiGe layer and $C_{Ge_initial}$ is the Ge concentration in this initial SiGe layer. The equivalent thickness of the silicon layer to be oxidised is: $20 * 0.8 + 8 = 24 \text{ nm}$. The final oxide thickness of $24 * 2.27 = 37.5 \text{ nm}$. This gives an estimation of condensation conditions to use to obtain a full oxidation of the SiGe/SOI stacked layers. It is necessary to mention that Si_{1-x}G_x alloys samples that are patterned by FIB have a condensation rate higher than the flat (unpatterned ones), this is due to the amorphization induced by FIB. At the end of the condensation step, a Ge pure layer remains directly in contact with SiO₂. If oxidation is gently pursued or even during annealing, dewetting of the Ge layer occurs: the layer breaks into small droplets that are self-organised by the pre-patterning of the SiGe layer before oxidation. It is this very last step of dewetting, which produces the formation of Ge dots. Oxidation has then

to be perfectly calibrated to get the dewetting and not the dissociation of Ge or even the diffusion of Ge through the oxide towards the underlying Si substrate.

In order to calibrate the oxidation rate, a series of dry oxidations were carried out at temperatures ranging from 700 °C to 850 °C for durations of 30 min to 90 min. We found that the optimal condensations were performed at 750°C in RTO during 3 hours among a set of Ge condensation calibrations after FIB patterning with very low doses: 1 μ s dwell time, 500 scans and 3 pA using $^{74}\text{Ge}^{2+}$ ions accelerated under 30 keV. The thickness of the SiO_2 layer was measured by ellipsometry. Calibrations are performed with reference samples of Si. The samples are then observed by SEM. An example of such images is given in figure 3.22.

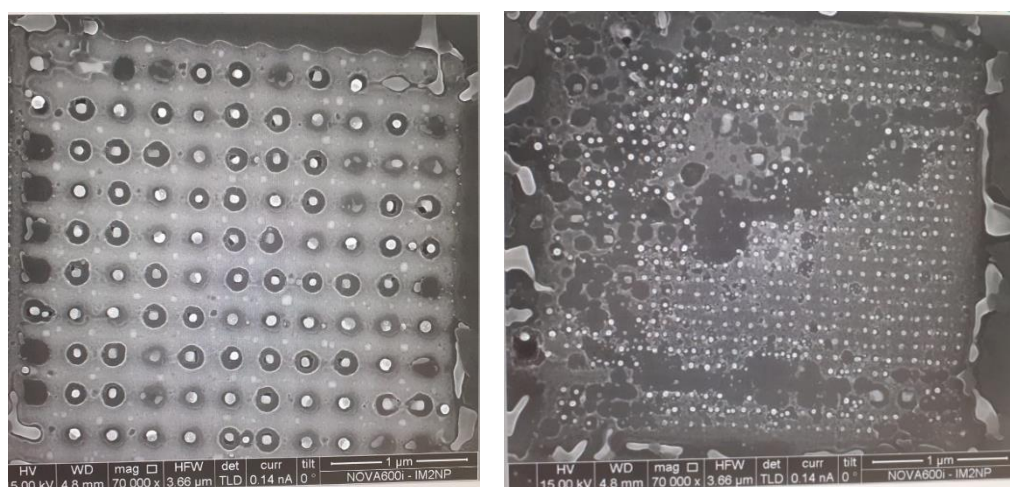


Figure 3.22 SEM observation of Ge QD obtained by dewetting of pure Ge layer after condensation of Ge in RTO at 750°C during three hours, the SiO_2 formed is removed with HF. The sample was first patterned with crossed lines with FIB.

From these characterizations, we demonstrated the formation of Ge QDs auto-assembly by coupling FIB lithography and Ge dewetting in RTO. The lateral size of the QDs depend on the distance between the patterns: when the distances between patterns (lines) is low and using low dwell-time of draw beam, the QD formed are well organised with lateral sizes as small as 30nm.

An important observation is that the FIB patterning is not reproducible and in several places, patterning produces defects, irregular pattern shapes and depths. For this reason, with FIB it was not possible to get clean samples with homogeneous Ge QDs. It was not possible to clearly understand what occurs exactly during the FIB process which induces such strong inhomogeneities and deficiencies. We think that may be the FIB filtered columns used during the PhD work are not really stable.

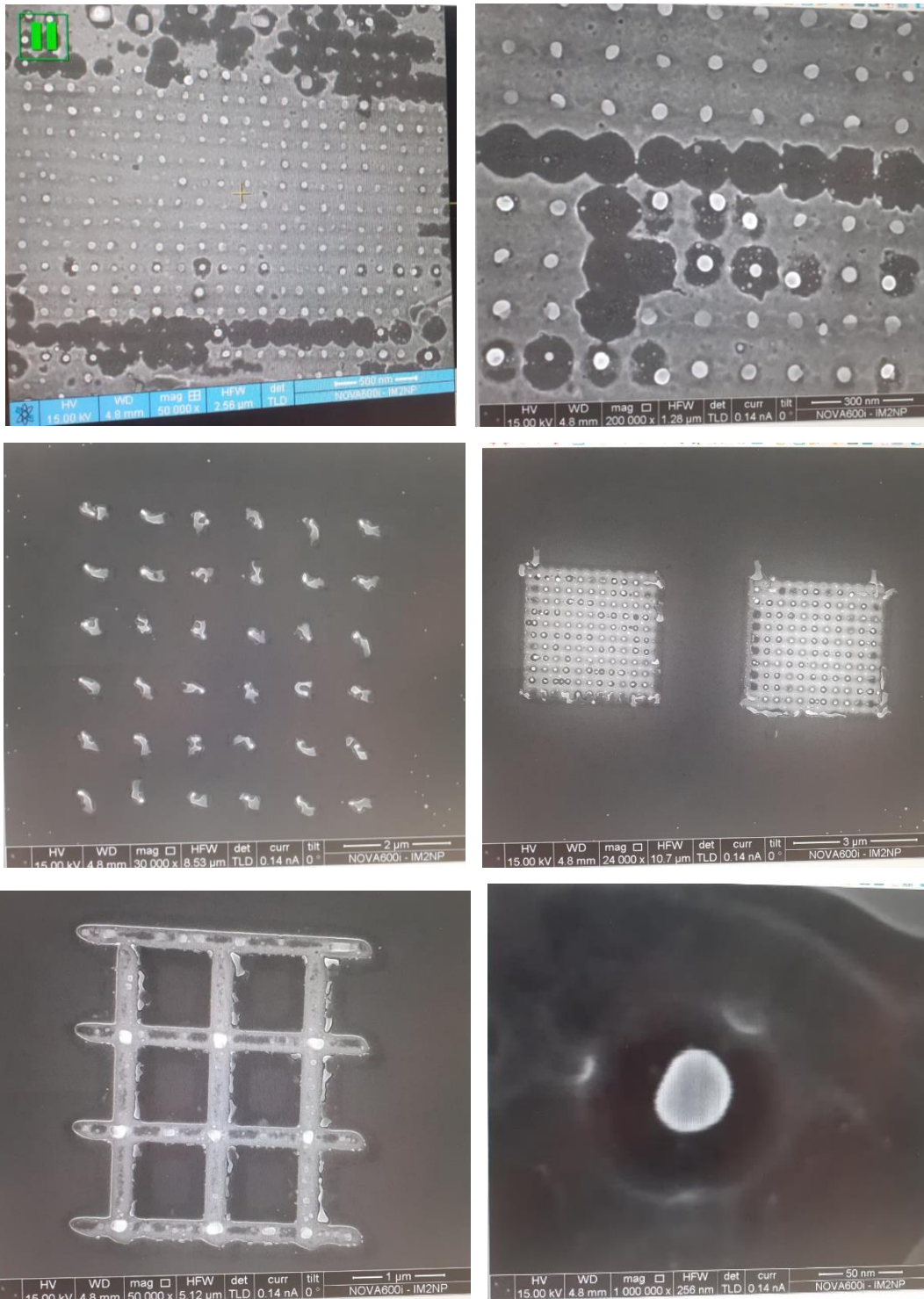


Figure 3.23. Examples of SEM observations showing different QD dimensions and different FIB patterns configurations: spot, lines and square arrays separated by different pitches.

III.4. Nanopatterning with He and Ne ions

These experiments were performed with GFIS-FIB in collaboration with ICFO in Spain, employing He and Ne as elements to pattern the SGOI surfaces at energies of 15 keV, 20 keV and 30 keV for Ne and 20 keV, 25 keV and 30 keV with He. All the patterns were made by paralleled lines with pitch of 3 μm and each line is 20 μm long and 150 nm wide. The doses were ranged from 0.01 nC/ μm^2 to 1 nC/ μm^2 . TEM observations were only performed on the patterns obtained at low energy with both He and Ne.

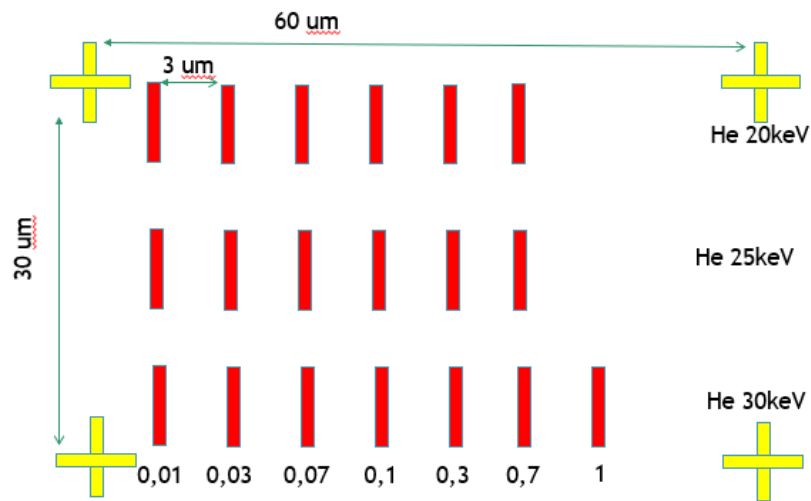


Figure 3.24. scheme of lines patterned with He -FIB in SiGe top layer of SGOI sample.

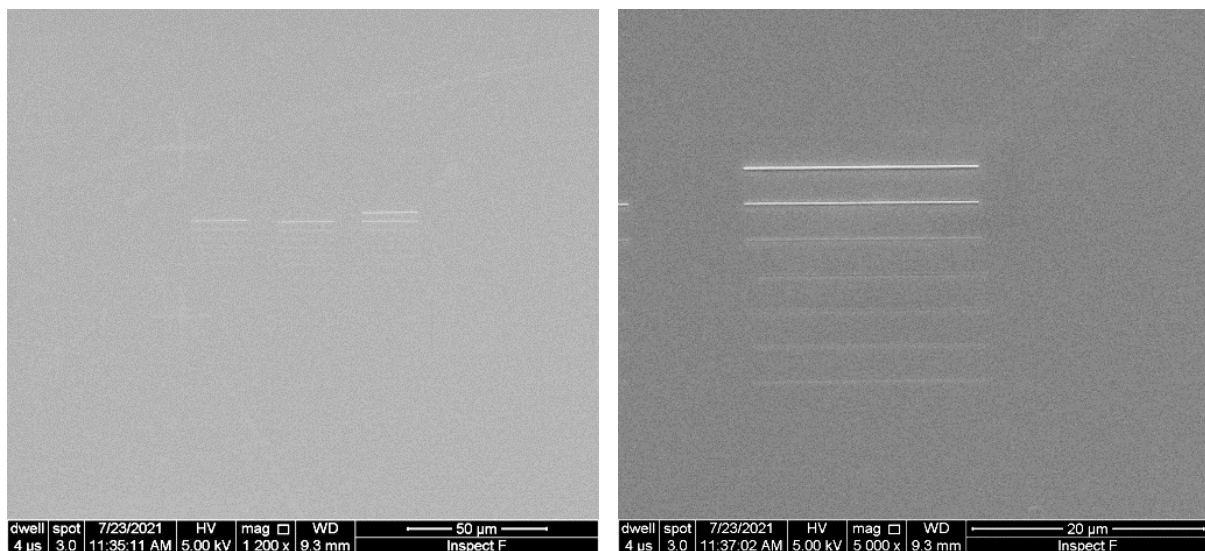


Figure 3.25. SEM observations of He patterns in SGOI.

The AFM images of the lines performed with He show that the depth of the lines obtained at high energy are too important and should cross the SiGe/SOI structure and even penetrate inside the substrate. This is absolutely no what we expected. Indeed as explained above, the aim is to pattern the extreme top surface of the SiGe layer which is used as a “sacrificial” layer. In consequence, among the lines performed at different energies and doses with He, we have chosen to observe the ones obtained at low doses and low energy (20 keV).

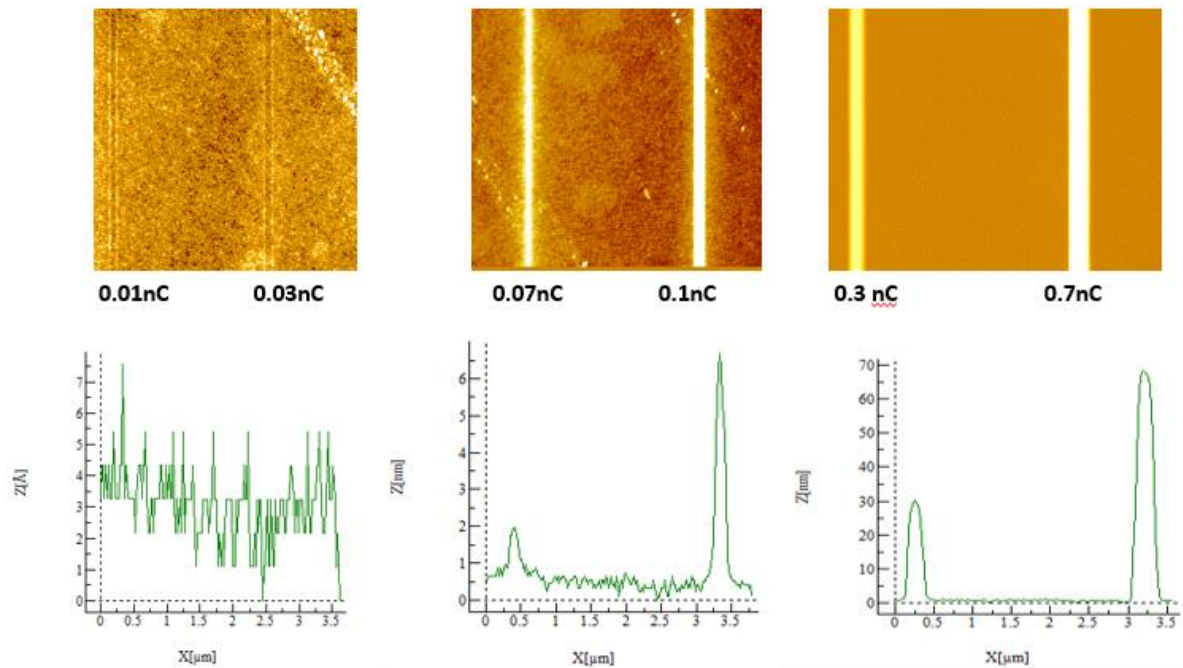


Figure 3.26. AFM images of He lines patterned at 20 keV.

AFM images showed that the lines have depths in the Å range and lateral size in the nm range for $0.01 \text{ nC}/\mu\text{m}^2$ and $0.03 \text{ nC}/\mu\text{m}^2$. TEM lamellae were performed on these patterns. Observations showed that even if the patterns are not so deep, there is a very deep penetration of the He ions: they cross SiGe and SOI layers and penetrate even the Si bulk. Similar situation was also observed at 20 keV.

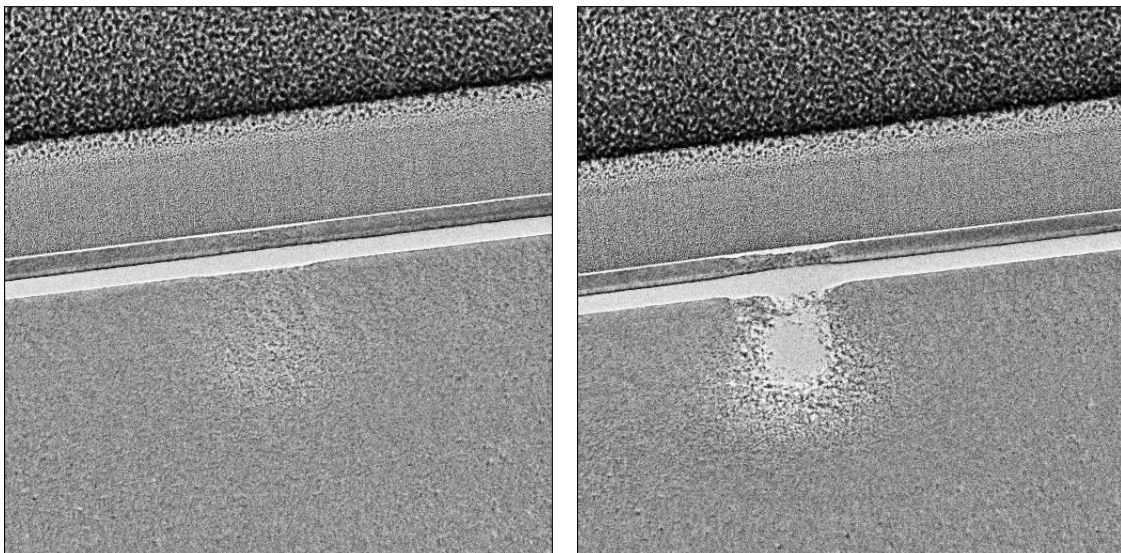
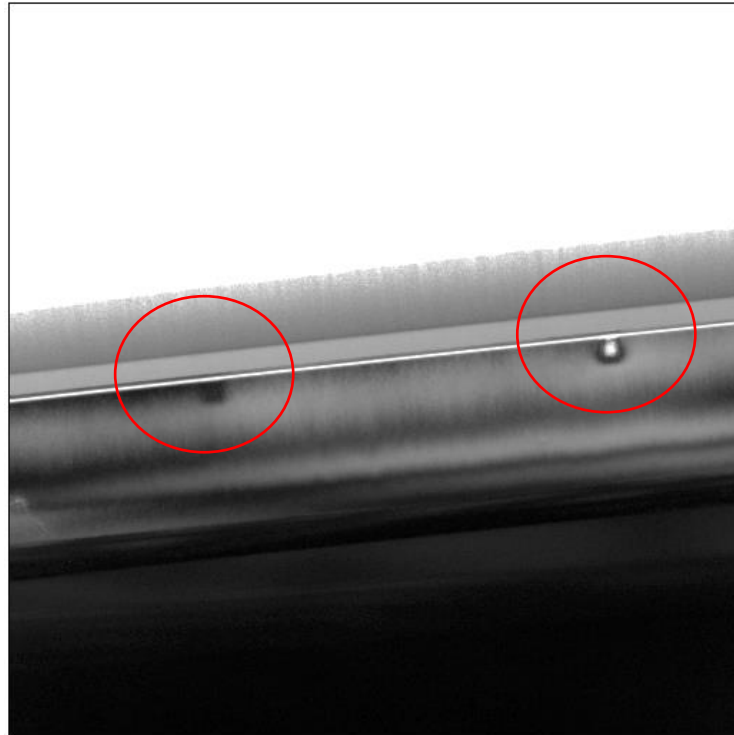


Figure 3.27. TEM observation for the lowest doses with He ions accelerated at 20keV surrounded with red circles with 0,01 nC/μm² on the left and 0,03 nC/μm² on the right.

Unfortunately, with 0,01 nC/μm², we only observe an amorphization with He ions of the SiGe/SOI layers, which appears as a swelling of the surface at these areas on AFM images. At 0,03 nC/μm² the He ions already penetrate too deeply in the Si bulk.

We performed similar Ne patterns at 15keV, 20 keV and 25keV as shown in figure 3.28. SEM observation of the patterns is given in Figure 3.29.

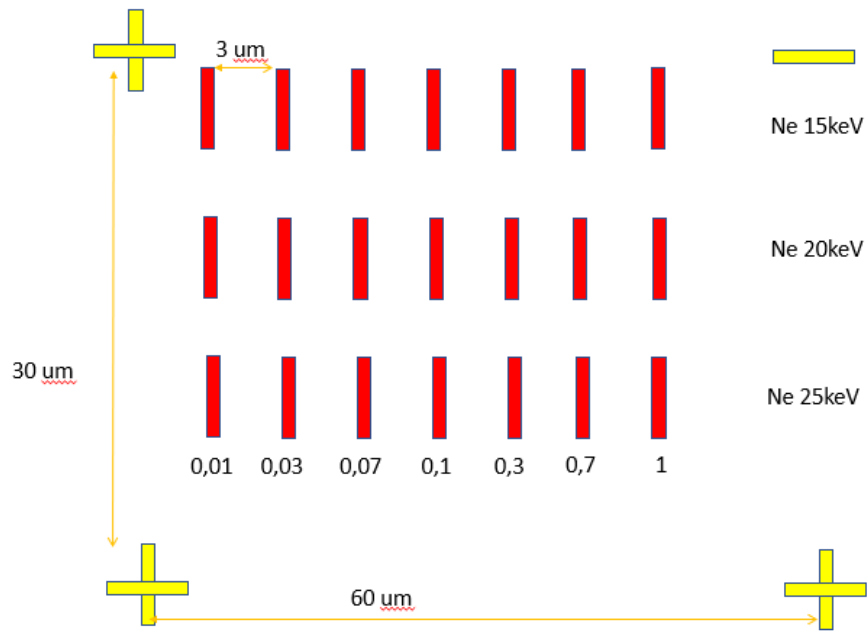


Figure 3.28 Schema of lines patterned with Ne by FIB in SGOI sample.

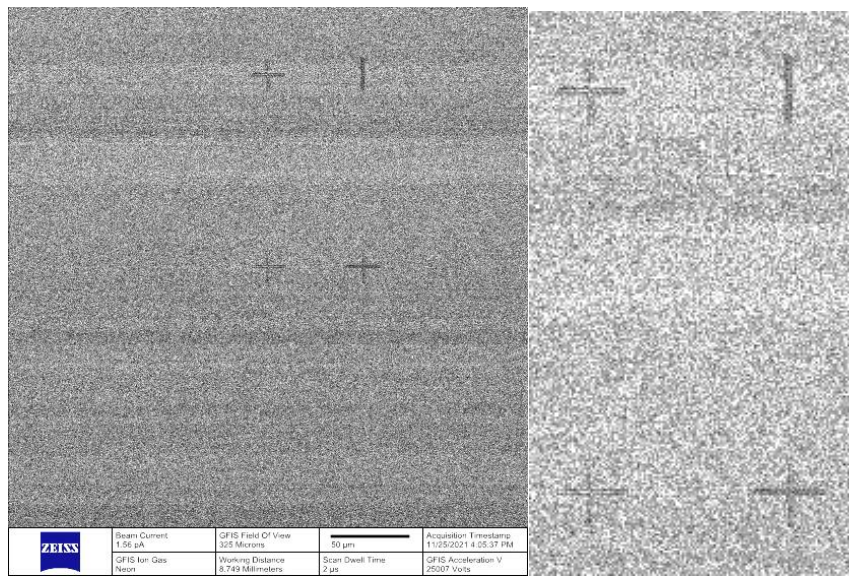


Figure 3.29 SEM observations of FIB patterns performed with Ne in SGOI.

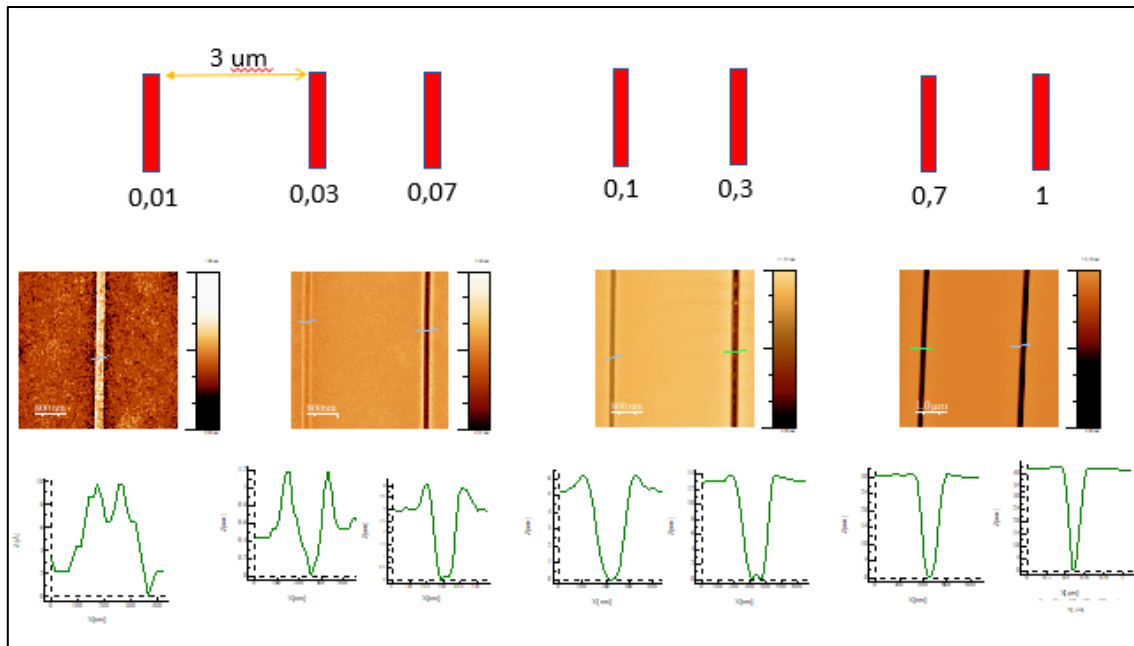


Figure 3.30. AFM images of Ne lines patterned at 15 keV.

The depth of the patterns was measured by AFM (Figure 3.30). All the dimensions measured are reported in the table below.

Energy [keV]	15	20	25
Dose [nC/μm ²]			
0.01	1nm swelling	1,1 nm swelling	1,7 nm swelling
0.03	0,5 nm swelling	1 nm swelling	1,6 nm swelling
0.07	3 nm	2,5 nm	0,95 nm
0.1	5 nm	5 nm	2,25 nm
0.3	13 nm	7,5 nm	2,5 nm
0.7	30 nm	21,5 nm	12 nm
1	42,5 nm	32 nm	22,5 nm

Table 3.3. Depth of lines measured from AFM images.

For all the samples, the penetration of ions is really too deep. Even at 15 keV and using Ne which is heavier than He, the ions penetrate in the Si bulk (Figure 3.31) and the samples could not be used for the condensation / dewetting application.

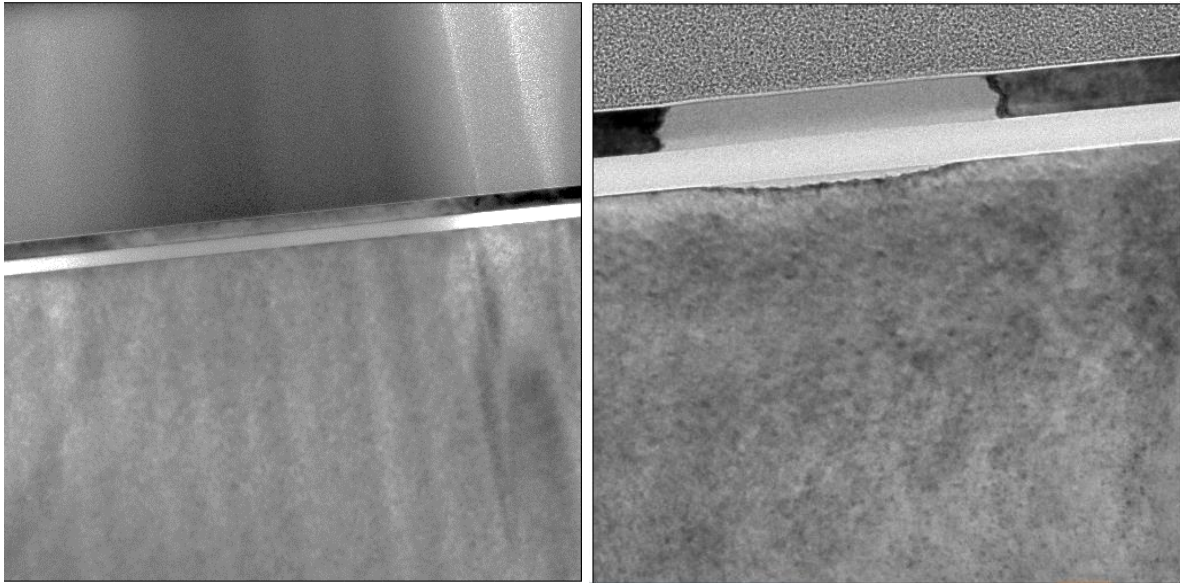


Figure 3.31. TEM observation of the lines performed with the lowest doses ($0,01 \text{ nC}/\mu\text{m}^2$ and $0,03 \text{ nC}/\mu\text{m}^2$) using Ne ions accelerated at 15 keV.

The lowest dose ($0,01 \text{ nC}/\mu\text{m}^2$) seems to be the optimal one for both Ne and He FIB nanopatterning. However, since the penetration is too important, the unique parameter which should be modified is the duration of the milling in order to decrease the amorphization only produce an erosion of few nm deep in the top layer of SiGe. But the main problem is the penetration depth even at 15keV. The next step would then be to decrease further the energy.

Conclusion and perspectives

In this work, we have performed a broad range of applications using the two dual beams FIB/SEM systems present either in OP (unfinished prototype Nanospace) or in IM2NP (Lyra from OP). We have performed various series of ion implantation, of nano-patterning and of TEM cross-section samples.

As known, the quantum science and technology have an important problem which is the development of material-processing techniques for the formation of quantum dots, optical diamond nanostructures containing a single-color centre ...etc, for wide range of applications quantum dots, nanowires, 2D materials, single colour centers...etc. The fabrication steps should have a short duration and a minimum price as well as the know-how easy to transmit are the major pillars that make the value and the importance of a process among others.

In this chapter, we showed two complementary procedures that are based on FIB lithography and thermal treatment which are mainly applicable to quantum photonic devices. Beginning with the single-photon emitters, we demonstrated the ability to create implantation of Si and Ge in diamond with FIB employing AuSi and AuGe LMAIS sources at very low doses and different energies. A subsequent thermal treatment which takes a few seconds per sample for lower doses is then performed to activate the SiV and GeV defects. Large series of patterned samples were performed, but no relevant PL results were obtained. The same procedure was applied to SGOI samples. Again, no PL characterization results were obtained.

Nanopatterning was then performed. The approach aim is to elaborate Ge QDs (with sizes <10nm). A combination of FIB nanopatterning and Ge condensation in RTO was developed. Some examples of dewetting were observed by SEM and AFM. However, I could not get TEM cross-section observations of the samples since the lamellae made in OP (using the FIB cross-section process) were not positioned on the patterned areas.

In these conditions, we can conclude that even if FIB should have excellent capabilities, the two OP apparatus used in this work were not stable (Au, Si and Ge sources are not stable in the conditions used here) and the soft were not adapted; this produces non-uniform patterns, with unreproducible sizes and depths. In addition the equipments were not user-friendly and presented several disfunctions. In these conditions such equipments cannot give relevant results for applications in optoelectronics, which was the main objective of the study.

At last, the patterns made with He and Ne were much too deep; for future experiments, we suggest to try to lower the energy. The doses should also be lowered to reduce the amorphization of the samples. Other experiments with a SiO₂ sacrificial layer on the top of SiGe/SOI, could also be performed.

References

- [1] Kurtsiefer C, Mayer S, Zarda P and Weinfurter H 2000 Stable solid-state source of single photons *Phys. Rev. Lett.* 85 290–3.
- [2] Beveratos A, Brouri R, Gacoin T, Poizat J-P and Grangier P 2001 Nonclassical radiation from diamond nanocrystals *Phys. Rev. A* 64 061802(R).
- [3] Babinec T M, Hausmann B J M, Khan M, Zhang Y, Maze J R, Hemmer P R and Loncar M 2010 A diamond nanowire single-photon source *Nat. Nano* 5 195–9
- [4] Wang C, Kurtsiefer C, Weinfurter H and Burchard B 2006 Single photon emission from SiV centres in diamond produced by ion implantation *J. Phys. B: At. Mol. Opt. Phys.* 39 37–41
- [5] Naydenov B, Kolesov R, Batalov A, Meijer J, Pezzagna S, Rogalla D, Jelezko F and Wrachtrup J 2009 Engineering single photon emitters by ion implantation in diamond *Appl. Phys. Lett.* 95 181109
- [6] Gaebel T, Popa I, Gruber A, Domhan M, Jelezko F and Wrachtrup J 2004 Stable single-photon source in the near infrared *New J. Phys.* 6 98
- [7] Aharonovich I, Castelletto S, Simpson D A, Stacey A, McCallum J, Greentree A D and Praver S 2009 Twolevel ultrabright single photon emission from diamond nanocrystals *Nano Lett.* 9 3191–5
- [8] Childress L, Taylor J M, Sorensen A S and Lukin M D 2006 Fault-tolerant quantum communication based on solid-state photon emitters *Phys. Rev. Lett.* 96 070504
- [9] Childress L, Taylor J M, Sorensen A S and Lukin M D 2005 Fault-tolerant quantum repeaters with minimal physical resources and implementations based on single-photon emitters *Phys. Rev. A* 72 052330
- [10] Jelezko F, Gaebel T, Popa I, Gruber A and Wrachtrup J 2004 Observation of coherent oscillations in a single electron spin *Phys. Rev. Lett.* 92 076401
- [11] Jelezko F, Gaebel T, Popa I, Domhan M, Gruber A and Wrachtrup J 2004 Observation of coherent oscillation of a single nuclear spin and realization of a two-qubit conditional quantum gate *Phys. Rev. Lett.* 93 130501
- [12] Gurudev Dutt, Childress L, Jiang L, Togan E, Maze J, Jelezko F, Zibrov A S, Hemmer P R and Lukin M D 2007 Quantum register based on individual electronic and nuclear spin qubits in diamond *Science* 316 1312–6
- [13] Neumann P et al 2010 Quantum register based on coupled electron spins in a room-temperature solid *Nat. Phys.* 6 249–53
- [14] Togan E et al 2010 Quantum entanglement between an optical photon and a solid-state qubit *Nature* 466 730–5
- [15] Maze J R et al 2008 Nanoscale magnetic sensing with an individual electronic spin in diamond *Nature* 455 644–8
- [16] Balasubramanian G et al 2008 Nanoscale imaging magnetometry with diamond spins under ambient conditions *Nature* 455 648–52

[17] Taylor J M, Cappellaro P, Childress L, Jiang L, Budker D, Hemmer P R, Yacoby A, Walsworth R and Lukin M D 2008 High-sensitivity diamond magnetometer with nanoscale resolution *Nat. Phys.* 4 810–6

[18] Weber J R, Koehl W F, Varley J B, Janotti A, Buckley B B, Walle C G V D and Awschalom D D 2010 Quantum computing with defects *Proc. Natl Acad. Sci.* 107 8513–8

General conclusion

Direct FIB writing using a column with a Wien filter that allows the production of different types of ion beams (Au, Si and Ge in our case), has a large number of applications in microelectronics. In particular, employing FIB for direct-writing lithography is a promising technique for quantum dots and nanocrystals self-organisation, and for specific single photon emitters when combining FIB lithography and condensation and dewetting. In this research work, I used several ion sources: He, Ne, AuSi, AuGe and Ga for different applications. Single He and Ne focused ion beams were employed for nanopatterning SGOI samples, while Si and Ge ions were used for both local implantation and milling process of SGOI and diamond samples and single Ga ion beam was employed for thin TEM lamellae preparation.

The FIB technique is more and more appealing for applications in different fields of science ranging from chemistry to biology, but these applications are still too marginal due to a number of drawbacks. Unfortunately, most of these drawbacks have not been addressed during the PhD thesis, in particular, the etching speed, the flexibility of the etchings and of different successive etching levels, the column alignment and the resolution of the ion beams have not been improved. The next problems to be addressed are the transition to UHV, the alignment procedures and process automation, the beam resolution especially when working at low voltage and the range of possible etched areas to adapt the technique to very large scale etchings.

The column developed is a mass filtered FIB column, producing a beam of Gold, Silicon and/or Germanium ions with unmatched resolutions in imaging and etching modes for different experimental conditions (accelerating current and voltage). The developed FIB column should be optimized at two levels: column optics and automation. At the optical level, even if different components have been modified (condenser and objective lenses, Wien filter, working distance...) the resolution has not been improved as compared to the Lyra column. At the level of automation, the work focused on the reproducibility of displacements and positions, the improvement of the comfort of use with an automatic alignment of the column, and the access to the alignment of a larger number of parameters). The column has been tested for the first time at the end of 2014, but because of several problems, it cannot be released to the market since this date. During the timescale of my PhD thesis the same problems have persisted.

The aim of the applicative task was to develop a universal nanostructuring technique using an ad hoc ion beam that responds to a given application and that allows either local implantation of source ions or etching using these ions. The aim was first to determine the optimal

experimental conditions for nanostructuring by studying the possibilities to improve the ultimate resolution of the nano-patterns, to decrease the generated defects and to reduce the redistribution area of the implanted impurities. On the other hand, the different possibilities to create large scale two-dimensional arrays: of topographic patterns, of seeds (metallic, organic and semiconductor), of defects (crystalline or impurities) and of stress gradients (by implanting Ge ions in a Si substrate) should also be investigated. Concerning the LMAIS-FIB using a Ge beam, its major interest, in addition to the localized character of the implantation, is to be able to vary in a continuous way the experimental conditions on a substrate in order to modulate the topographic and/or structural properties. Thus we have shown that it is possible to fabricate arrays of objects with a continuous variation of interactions, number and size of objects with strictly identical experimental conditions on a single test sample. As an example, arrays structures of variable sizes made by heterogeneous dewetting on FIB patterns have been realised. The experimental parameters of FIB milling were tested to produce ad hoc patterns. The effective use of FIB nanostructuring has been demonstrated for two main applications in silicon-based semiconductors and in diamond. In particular, the work focused first on the realization of self-organized SiGe QDs and second on the fabrication of light emitting defects. In this context, arrays of gold, Si, Ge were realized. They were then used to fabricate Ge QDs structures based on SiGe thin films and obtained by molecular beam epitaxial growth. These structures could contribute to the development of new photonic devices. The latter could not be realized during the timescale of the PhD thesis, because of the difficulties encountered with the use of the FIB equipment and the permanent deficiencies in the use of the FIB instrument.

The experimental studies using diamond, silicon bulk, thin SGOI and ultra-thin SOI for FIB processing have been reported in the third chapter. Most of the samples have been exposed to an annealing treatment in RTO, and then characterized with PL spectroscopy, and TEM. For the quantum dots obtained by combining FIB lithography (using Ge ions at 30 keV) and oxidation/condensation at 750 °C, this result demonstrates the potential of this approach to improve the FIB-patterning resolution.

Direct milling, nanopatterning or local implantation showed the powerful and the advantages of FIB, which is still a key technique for nano-structuration in semiconductor field. In this work, benefits, limitations and applications of FIB IBL were outlined. The results have been compared to those obtained with other ion sources such as He and Ne. FIB stations with more attractive parts trial-beams for both nano-structuration, local implantation and chemical and/or surface characterization would be favoured since they could allow quantum engineering to

control the size and the structure of the nanomaterial fabricated with nano-meter resolution and with precise placement of the patterns which are required for well-designed quantum devices to assure their reproducible fabrication. Settings as doses and energies and beam options are the key parameters of this kind of sources, which provide few depths for nanostructures, that must be done very well with high precision to avoid undesirable effects and to enhance FIB processing. Dual beam FIB/SEM platform is established as a standard and powerful technique for nanofabrication for new breakthroughs in next-generation research.